frontiers | Research Topics

Integrated quantum photonics

Edited by
Shinichi Saito, Yong Zhang and Qin Wang

Published in
Frontiers in Physics

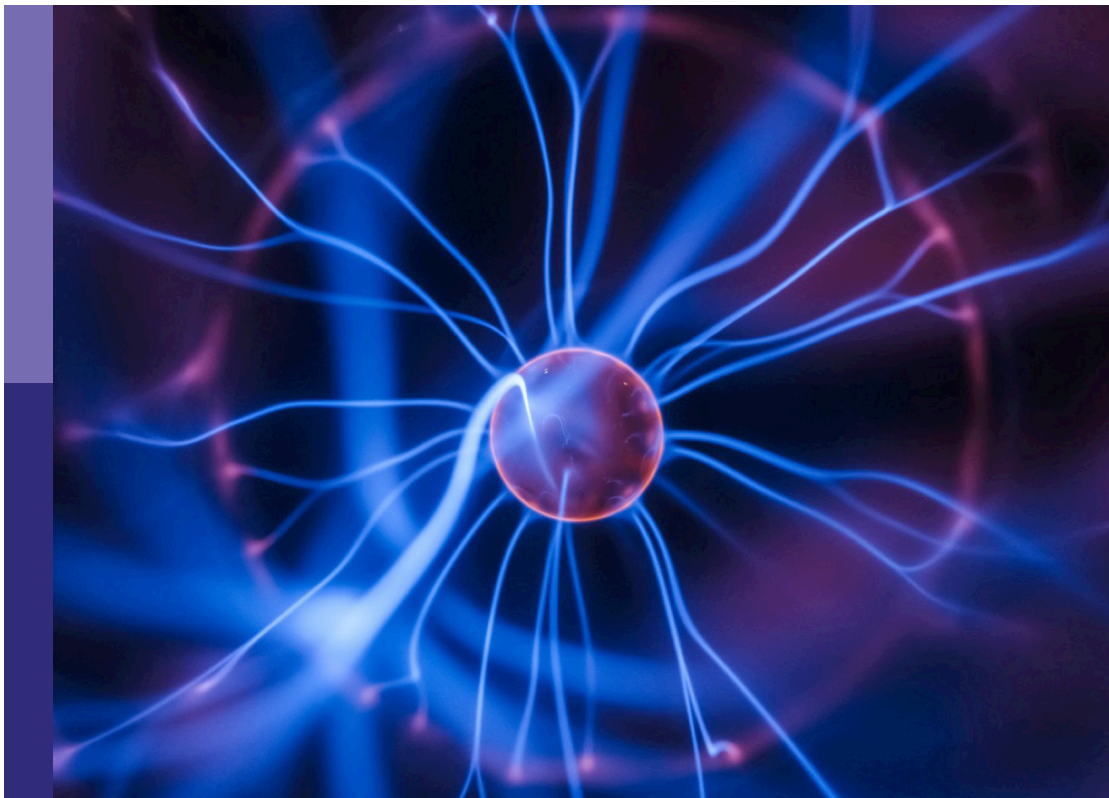

ISSN 1664-8714
ISBN 978-2-8897-4074-1
DOI 10.3389/978-2-8897-4074-1

About Frontiers

Frontiers is more than just an open access publisher of scholarly articles: it is a pioneering approach to the world of academia, radically improving the way scholarly research is managed. The grand vision of Frontiers is a world where all people have an equal opportunity to seek, share and generate knowledge. Frontiers provides immediate and permanent online open access to all its publications, but this alone is not enough to realize our grand goals.

Frontiers journal series

The Frontiers journal series is a multi-tier and interdisciplinary set of open-access, online journals, promising a paradigm shift from the current review, selection and dissemination processes in academic publishing. All Frontiers journals are driven by researchers for researchers; therefore, they constitute a service to the scholarly community. At the same time, the *Frontiers journal series* operates on a revolutionary invention, the tiered publishing system, initially addressing specific communities of scholars, and gradually climbing up to broader public understanding, thus serving the interests of the lay society, too.

Dedication to quality

Each Frontiers article is a landmark of the highest quality, thanks to genuinely collaborative interactions between authors and review editors, who include some of the world's best academicians. Research must be certified by peers before entering a stream of knowledge that may eventually reach the public - and shape society; therefore, Frontiers only applies the most rigorous and unbiased reviews. Frontiers revolutionizes research publishing by freely delivering the most outstanding research, evaluated with no bias from both the academic and social point of view. By applying the most advanced information technologies, Frontiers is catapulting scholarly publishing into a new generation.

What are Frontiers Research Topics?

Frontiers Research Topics are very popular trademarks of the *Frontiers journals series*: they are collections of at least ten articles, all centered on a particular subject. With their unique mix of varied contributions from Original Research to Review Articles, Frontiers Research Topics unify the most influential researchers, the latest key findings and historical advances in a hot research area.

Find out more on how to host your own Frontiers Research Topic or contribute to one as an author by contacting the Frontiers editorial office: frontiersin.org/about/contact

Integrated quantum photonics

Topic editors

Shinichi Saito — Hitachi, Japan

Yong Zhang — University of North Carolina at Charlotte, United States

Qin Wang — Nanjing University of Posts and Telecommunications, China

Citation

Saito, S., Zhang, Y., Wang, Q., eds. (2023). *Integrated quantum photonics*. Lausanne: Frontiers Media SA. doi: 10.3389/978-2-8897-4074-1

Table of contents

frontiers in Physics

EDITORIAL
published: 26 November 2021
doi: 10.3389/fphy.2021.800648

Editorial: Integrated Quantum Photonics

Shinichi Saito *

Center for Exploratory Research Laboratory, Research and Development Group, Hitachi, Ltd., Tokyo, Japan

Keywords: quantum random number generators, Si photonics integrated circuits, optical vortex, photonic crystal, poincare sphere, quantum photonic circuits

Editorial on the Research Topic

Integrated Quantum Photonics

Integration of electronic transistors in a silicon (Si) chip has now exceeded more than 10 B in micro-processing units (MPUs) and graphics processing units (GPUs), which is even larger than the number of neurons in a human brain. The extensive usages of these processing units for various machine-learning and artificial intelligence (AI) applications also demand integration of photonic devices for Internet-Of-Things (IOT) networks and big data analysis. Si photonics will be a key technology for photonics integration, and for the future, photonic-based quantum technologies will be introduced. One of the obvious advantages to use photons instead of electrons for quantum technologies is the potential to introduced these devices at room temperatures without complicated expensive cryogenic systems. We thought it is a good time to call for papers in integrated quantum photonics in Frontiers. In this research topic, five papers were submitted, one paper was rejected, four papers were accepted, but one paper was retracted by the authors. The number of papers which we have attracted was smaller than we expected, but we think the research area will grow over the years.

In the paper of Bisadi et al. a compact quantum random number generator was demonstrated, using a novel light-emitting diode using Si nanocrystals. The group, led by Pavesi, is a leading group for light emissions from Si nanocrystals, and a random number generator will be a suitable application, relying on quantum mechanical probabilistic characteristics of spontaneous emissions. They have developed an integrated system together with an Si photomultiplier and a field-programmable gate array (FPGA) processing unit and showed that their data pass all statistical standards as random numbers. The recorded bit rate of 0.5 Mbps is already comparable to commercial products without using Si nanocrystals. The technology with Si nanocrystals will be used for applications which require even more severe security controls, such as secure communications, among governments, mobile banking, and statistical research.

For various quantum applications, we need a two-level system for describing a quantum bit (qubit). In the paper of Sotto et al. they found a new way to control a polarization state as a two-level system by introducing a phase mismatch between adjacent photonic crystals. In a standard design of a waveguide in a photonic crystal, a line defect is introduced simply by removing holes for a waveguide, and the parity symmetry against mirror reflection is maintained. They intentionally introduced a mismatch by introducing a phase shift among adjacent photonic crystals across the waveguide, which allowed coupling of two propagation modes. By applying a simple model for a two-level system, they found the energy gap is opening up by controlling the amount of the phase shift.

In the last paper, another two-level system is proposed by using photons with left and right vortices. Photons with vortices have optical orbital angular momentum (OAM), and we expect a quantum mechanical superposition state among left and right circulations in a hyper-

OPEN ACCESS

Edited and reviewed by:
Lorenzo Pavesi,
University of Trento, Italy

Correspondence:
Shinichi Saito
shinichi.saito.qt@hitachi.com

Specialty section:
This article was submitted to Optics and Photonics, a section of the journal Frontiers in Physics

Received: *23 October 2021*
Accepted: *28 October 2021*
Published: *26 November 2021*

Citation:
Saito S (2021) Editorial: Integrated Quantum Photonics. Front. Phys. 9:800648. doi: 10.3389/fphy.2021.800648

Poincaré sphere. By using a simple Si photonic two-bus waveguide together with a complex micro-gear, the amplitudes and phases are controlled for the left and right vortices. The device was named a Poincaré rotator, since it allows to rotate the vectorial OAM state in a hyper-Poincaré sphere. The conservation law of spin and OAM was discussed.

We believe the research area of integrated quantum photonics will be even more important for the future, and proposed devices will be developed beyond original foreseeable applications.

AUTHOR CONTRIBUTIONS

The author confirms being the sole contributor of this work and has approved it for publication.

FUNDING

The author SS is supported by JSPS KAKENHI Grant Number JP 18K19958.

Conflict of Interest: SS is employed by Hitachi.

frontiers in Physics

ORIGINAL RESEARCH
published: 14 February 2018
doi: 10.3389/fphy.2018.00009

Compact Quantum Random Number Generator with Silicon Nanocrystals Light Emitting Device Coupled to a Silicon Photomultiplier

Zahra Bisadi[1], Fabio Acerbi[2], Giorgio Fontana[1], Nicola Zorzi[2], Claudio Piemonte[2], Georg Pucker[2] and Lorenzo Pavesi[1]*

[1] Nanoscience Laboratory, Department of Physics, University of Trento, Trento, Italy, [2] Center for Materials and Microsystems, Bruno Kessler Foundation (FBK), Trento, Italy

A small-sized photonic quantum random number generator, easy to be implemented in small electronic devices for secure data encryption and other applications, is highly demanding nowadays. Here, we propose a compact configuration with Silicon nanocrystals large area light emitting device (LED) coupled to a Silicon photomultiplier to generate random numbers. The random number generation methodology is based on the photon arrival time and is robust against the non-idealities of the detector and the source of quantum entropy. The raw data show high quality of randomness and pass all the statistical tests in national institute of standards and technology tests (NIST) suite without a post-processing algorithm. The highest bit rate is 0.5 Mbps with the efficiency of 4 bits per detected photon.

Keywords: compact photonic quantum random number generation, silicon nanocrystals LED, silicon photomultiplier, robust methodology, NIST tests

OPEN ACCESS

Edited by:
Derek Abbott,
University of Adelaide, Australia

Reviewed by:
Junichi Fujikata,
Photonics Electronics Technology Research Association, Japan
Bernard Gelloz,
Nagoya University, Japan

****Correspondence:***
Zahra Bisadi
zahra.bisadi@unitn.it;
zahra.bisadi.86@gmail.com

Specialty section:
This article was submitted to Optics and Photonics, a section of the journal Frontiers in Physics

Received: *28 September 2017*
Accepted: *30 January 2018*
Published: *14 February 2018*

Citation:
Bisadi Z, Acerbi F, Fontana G, Zorzi N, Piemonte C, Pucker G and Pavesi L (2018) Compact Quantum Random Number Generator with Silicon Nanocrystals Light Emitting Device Coupled to a Silicon Photomultiplier. Front. Phys. 6:9. doi: 10.3389/fphy.2018.00009

1. INTRODUCTION

Thanks to the quantum properties of light, "truly" random numbers can be produced by photonic quantum random number generators (PQRNG). Cryptographic tasks of encryption and decryption of private data can be executed using secret keys based on high quality random numbers. Even though mathematical algorithms are extensively used to generate random numbers, they suffer from high guessability provided the seed of the algorithm is known. If they have a short periodicity, their repeatability would be a serious flaw, as well.

PQRNGs benefit from the intrinsically random and unpredictable properties of physical processes involving photons as the quanta of light. The randomness in path taken by photons arriving on a beam splitter[1] [1], the comparison of the waiting time for photon arrivals in adjacent time intervals [2] and the combination of both methods [3] have been used to generate random numbers. In some other works, encoding the number of arriving photons in observation windows [4–6] and the randomness in the photon arrival times [7–9] have been used to produce random numbers. Recently, a robust approach based on arrival times of photons has been proposed by our group [9]. It considers all the non-idealities of the source as well as the detector, producing high quality random numbers which pass all the statistical tests in national institute of standards and technology (NIST) tests suite and TestU01 without a post-processing algorithm[1].

[1]Dataset. http://www.idquantique.com/wordpress/wp-content/uploads/white-paper-understanding-qkd.pdf. (2016).

However, in all the above-mentioned approaches a bulky setup is used to generate random numbers. A small-sized and compact PQRNG, easy to be implemented in small electronic devices such as mobile phones and cameras for secure data encryption and decryption as well as other applications, is highly essential for facile accessibility to everyone. Here, we present a first step toward this goal: a PQRNG with a novel, compact configuration comprising a silicon nanocrystals large area LED (Si-NCs LLED) coupled with a silicon photomultiplier (SiPM) in free space. Based on some statistical analyses described in section 5, it is proved that the generated hexadecimal random symbols have a very high quality and the corresponding random bits pass all the statistical tests in NIST tests suite with no post-processing operations. The highest bit rate of 0.5 Mbps is achieved with the efficiency of 4-bits per detected photon.

In a previous work [9], we have demonstrated a procedure to extract high quality random numbers from the arrival time of photons emitted by a Si-NCs LED, collected by a fiber bundle and detected by a commercial single photon avalanche diode (SPAD). In this work we use the same robust methodology of random number extraction of Bisadi et al. [9] but we demonstrate a PQRNG where the LLED is directly faced to a SiPM. Moreover, both devices are fabricated by the same silicon pilot line of Bruno Kessler Foundation (FBK) with a dimension allowing optimum coupling which is specifically challenging for the Si-NCs LLED.

This work is organized as follows. In section 2, the Si-NCs LLEDs and their electrical and optical characteristics are described. In section 3, the SiPM is introduced and explained. Section 4 describes the experimental procedure and random numbers extraction. Randomness analyses are discussed in section 5 and at the end the conclusions are presented.

2. SI-NCS LARGE AREA LED

Si-NCs are silicon quantum dots which emit light at room temperature in the visible range due to quantum confinement. The emitted photons are emitted independently by a quantum process named spontaneous emission and their statistics obey Poisson statistics (see more in section 4).

Si-NCs LEDs are fabricated by complementary metal-oxide-semiconductor (CMOS) processing, they can be easily incorporated in integrated configurations, they emit photons with wavelengths in the spectral range detectable by silicon detectors allowing the fabrication of an all-silicon-based device and since the spontaneous emission of photons in a Si-NCs LED is a non-deterministic, quantum mechanical and random process, they can be used as a quantum source of randomness to generate random numbers. The Si-NCs LEDs were fabricated with a large emitting surface in order to illuminate large area detectors like the SiPM we use here. The matching of the emitter and detector surfaces allows their direct coupling, i.e., without any coupling optics. The Si-NCs LLED (large area LED) has the active layer structure formed by a multilayer structure with 5 periods of silicon rich oxide (SRO)/SiO_2 layers of 3.5–4 nm and 2 nm thicknesses, respectively (**Figure 1A**). The Si-NCs are grown in a silica matrix through the plasma enhanced chemical vapor deposition (PECVD) technique and annealed at 1150°C for 30 min to form the Si-NCs.

The Si-NCs LLEDs have been prepared in three different sizes: big (b), medium (m) and small (s) with emitting surface area of 1.3 mm × 0.99 mm, 0.99 mm × 0.82 mm and 1.02 mm × 0.11 mm, respectively (see **Figure 1B**).

The electroluminescence (EL) spectra of the Si-NCs LLEDs can be seen in **Figure 2A** with a high peak at ∼ 900 nm attributed to the emission from Si-NCs. Note that all the LLEDs show the same EL lineshape which points to the great uniformity of the fabrication. **Table 1** reports the optoelectronic characteristics of these LLEDs. The figure of merit is the efficiency of the EL which is measured as the ratio between the EL intensity and the driving electrical power. The electrical power density is calculated to be 5.87, 0.93 and 0.08 mW/cm^2 for the (b), (m) and (s) LLEDs, respectively. It should be noted that the applied currents to the (b), (m) and (s) LLEDs are 30, 3 and 3 μA, respectively.

At currents lower than 30μA to the (b) LLED, no appreciable EL is observed. Therefore, by applying the previously-mentioned currents to the LLEDs, we tried to keep the voltages and hence the electric field through the active area of the LLEDs (with actual thickness of ∼22.5 nm) more or less the same. The low current density and high EL intensity of the (m)LLED yield the higher efficiency of this LLED compared with the (b) and (s) LLEDs. In addition to the efficiency, the active area of (m)LLED allows a suitable coupling with the large area SiPM since the SiPM dimensions are of 1 mm × 1 mm. It should be noted that all three LLEDs result in the generation of high quality random numbers since they are fabricated in a very similar way and the detected photons from all of them follow a Poisson distribution.

The current-voltage (I/V) characteristics of Si-NCs LLED are presented in **Figure 2B**. They show a rectifying behavior with more current density at forward regime—i.e., negative voltage applied to the cathode and zero voltage to the anode—than the reverse regime—i.e., positive voltage applied to the cathode and zero voltage to the anode. It is observed that at a fixed forward voltage, the current density through the (b) LLED is larger than (m) and (s) LLEDs (particularly at 0.5–3 V): this is due to the larger free carrier density flowing through the active area in (b) than (m) and (s) LLEDs. In the reverse bias region (1–6 V), however, the (b), (m), and (s) LLEDs show the same order of magnitude current densities that is related to the inefficient carrier injection to the active area by the accumulation of the charges near the boundaries of the cathode and the anode. This effect blocks the carriers from flowing through, recombining and contributing to the net current and consequently makes the current density independent of the gate areas of the LLEDs[2]. The charge blocking seems to be more effective for (s) LLED with a flat I/V curve at the region of −0.5–1 V (**Figure 2B**).

These LLEDs can emit light over long hours of operation. **Figure 3** shows the EL of the (m) LLED over ∼16 h. Note that the EL variation is compensated by the randomness extraction [9] and does not influence the quality of random numbers and therefore no adjustment of the QRNG is needed over a very long working period.

[2]Dataset. "http://www.ieee.li/pdf/essay/pin_diode_handbook.pdf/" (1998).

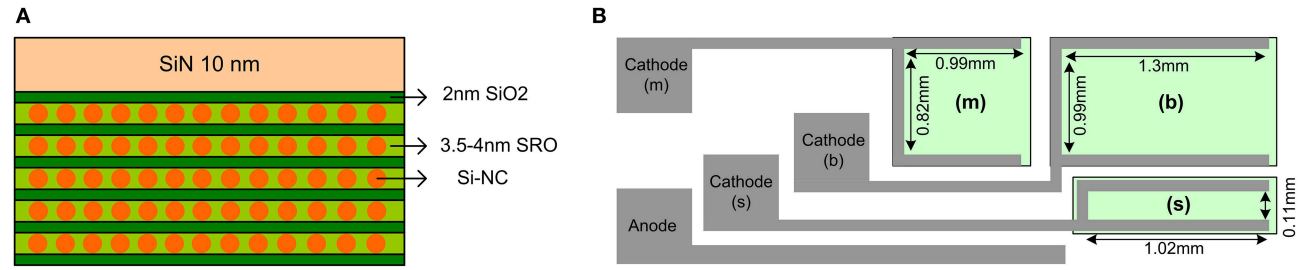

FIGURE 1 | (A) The multilayer structure of Si-NCs LLED with 5 periods of 3.5–4 nm silicon rich oxide (SRO) sandwiched between 2 nm thick SiO_2. **(B)** The geometry of Si-NCs LLED with different sizes b (big), m (medium) and s (small). The cathode and common anode electrodes are shown.

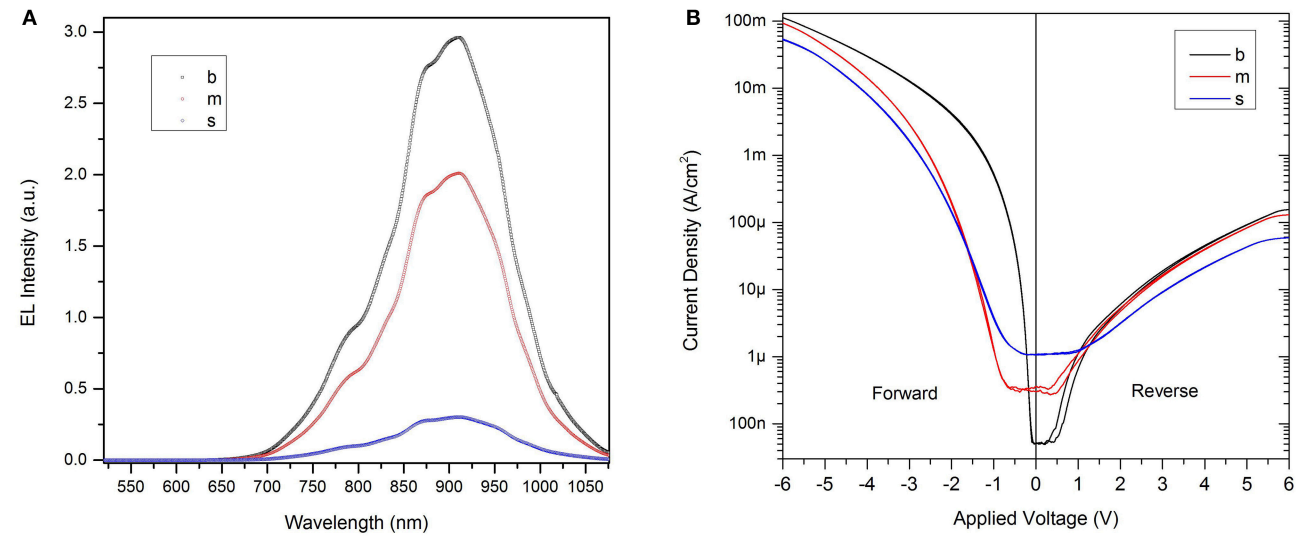

FIGURE 2 | (A) The EL spectra of the three different sizes of Si-NCs LLED illustrated in **Figure 1A**. A high peak at ∼900 nm can be seen which is attributed to the emission from Si-NCs. The EL spectra are acquired by a Spectra-Pro 2300i monochromator coupled with a nitrogen-cooled charge coupled device (CCD) camera. The measurements were performed at room temperature in a dark chamber. EL intensity is normalized for the responsivity of the spectrometer. **(B)** The I/V characteristics of the Si-NCs LLEDs. A quite rectifying behavior is observed in the I/V curves with more current density at forward regime—i.e., negative voltage applied to the n-type contact electrode and zero voltage to the p-type contact electrode—than reverse regime—i.e., positive voltage applied to the n-type contact electrode and zero voltage to the p-type contact electrode.

TABLE 1 | The efficiency (EL over injected power) of (b), (m), and (s)LLED.

LLED	Area (mm^2)	Voltage (V)	Current Density (mA/cm^2)	EL (Kcps)	Efficiency (Kcps/W)
b	1.29	2.52	2.33	∼533	70
m	0.81	2.34	0.37	∼363	517
s	0.11	3	2.67	∼364	413

3. SILICON PHOTOMULTIPLIER

The analog SiPM is an array of many (hundreds) of single photon avalanche diodes (SPADs). They are all connected in parallel to a common anode and cathode, each one with its own quenching resistor. Each cell (i.e., SPAD+resistor) is sensitive to a single photon and provides a current pulse at the output. Therefore, the counts at the SiPM output are proportional to the number of triggered cells, thus to the number of detected photons. Different technologies for SiPM have been developed in FBK during last few years, with peak sensitivity in the green part (RGB-SiPM) or in the blue part (NUV-SiPM) of the visible spectrum, and with different cell sizes. The NUV technology, in particular, benefits from an upgraded silicon material [10], employing an epi/substrate structure with a lower-lifetime substrate. This gives particular benefits in terms of correlated noise reduction, i.e., afterpulsing probability (AP) and delayed crosstalk probability (DeCT), which are particularly detrimental for QRNG applications [9].

In this work we employ a 1 mm ×1 mm NUV SiPM (inset in **Figure 4B**), containing 625 cells (SPADs) with the cell size of 40 μm and the fill factor (FF) of 60 %. This particular technology has a photon detection efficiency (PDE) (and in particular spectral sensitivity) not matched to the LLED emission. PDE is about 5% at 800 nm, at 4 V of excess bias (i.e., the

difference between the applied bias and the breakdown voltage (V_{bd})), as shown in **Figure 4A**. However, NUV SiPM has the advantage of a low primary dark count rate (DCR), less than 100 kcps/mm^2 at 5 V of excess bias (see **Figure 4B**), meaning less than 200 cps per single SPAD. In addition, it has a reduced correlated noise probability (overall AP+DeCT probability lower than 5%), which is very important in this kind of application.

We designed a custom front-end board to amplify and digitalize the analog output signal from the detector (see **Figure 5B**). This is based on a AD8000 amplifier in a trans-impedance configuration, followed by a comparator with an adjustable voltage threshold and a monostable, creating pulses of 3.3 V and 100 ns width. This fixes the maximum count rate of the detection system, which is anyhow limited by the afterpulsing time constant of the detector, giving an overall time to let all traps to empty, thus an overall time to avoid any possible afterpulsing, of few hundreds of nanoseconds, as seen in the autocorrelation function. As will be explained in section 4, this signal is transferred to a field-programmable gate array (FPGA) processing unit for the generation of random symbols.

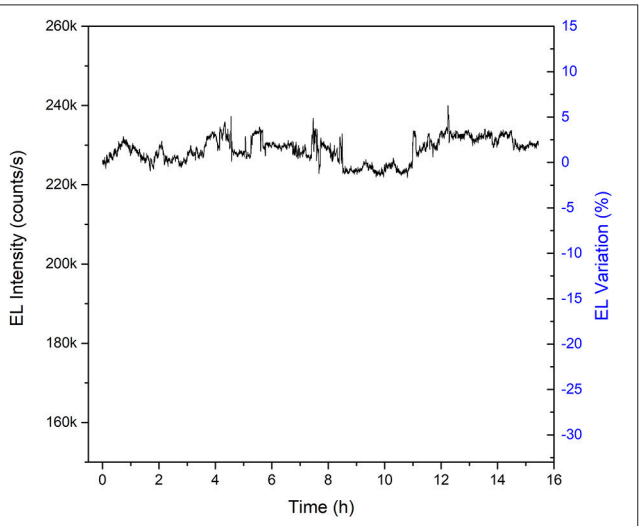

FIGURE 3 | EL of the (m) LLED vs. time at the applied current density of 0.62 mA/cm^2 (corresponding to an applied voltage of 2.61 V). The right hand side of the figure (blue axis) shows the EL variation percentage.

4. EXPERIMENTAL

The experimental setup is schematically shown in **Figure 5A**. The (m)LLED is directly facing a SiPM at a distance of ∼ 1 mm without any interposed optics or diffuser. The Si-NCs LLED is driven by an Agilent B1500A Semiconductor Device Parameter Analyzer. The TTL output of the SiPM is directly connected to the high speed digital input of an FPGA. A voltage of ∼30–36 V is applied to the SiPM by an Agilent E3631A DC Power Supply. The measurement of the arrival times is performed by a fully synchronous logic. The FPGA continuously samples the detector at the frequency of 100 MHz, which is crystal controlled. A valid detection is produced by a high analog logic level heralded by one clock cycle (10 ns) of low analog logic level. A Digilent ATLYS FPGA board has been used with the programming language VHDL.

In order to verify that the Si-NCs emit independent photons, cross correlation measurements can be performed. The measurement is based on the random transmission of the emitted photons from the source (i.e., a Si-NCs LLED) into two arms of a fiber beam splitter (see **Figure 6A**) each connected to a detector (i.e., a SPAD). The longer arms of the fiber splitter are long enough (15 m) to prevent any possible peaks in the correlogram due to the correlation of either backflashs or back reflections and the real signals on the silicon SPADs within 60 ns time lags. Therefore, any visible peaks in the correlogram

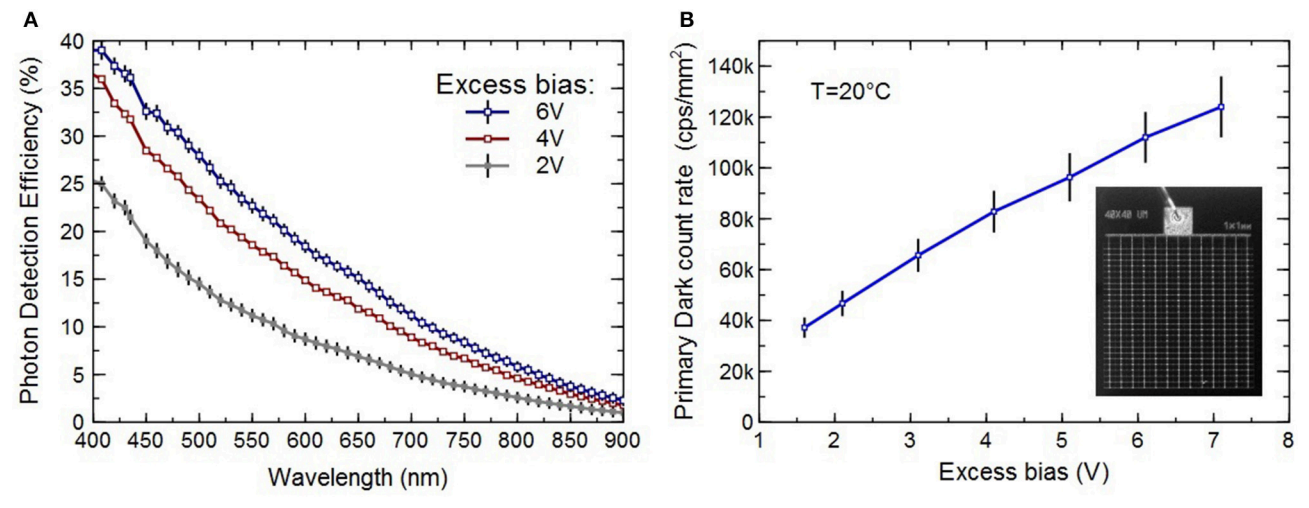

FIGURE 4 | (A) Measured photon detection efficiency (PDE), including the FF, as a function of wavelength for NUV SiPM at excess bias of 2, 4, and 6 V. **(B)** Dark count rate (DCR) of NUV SiPM vs. excess bias at temperature of 20°C. The inset shows 1 mm×1 mm SiPM containing 625 SPADs with cell size of 40 μm.

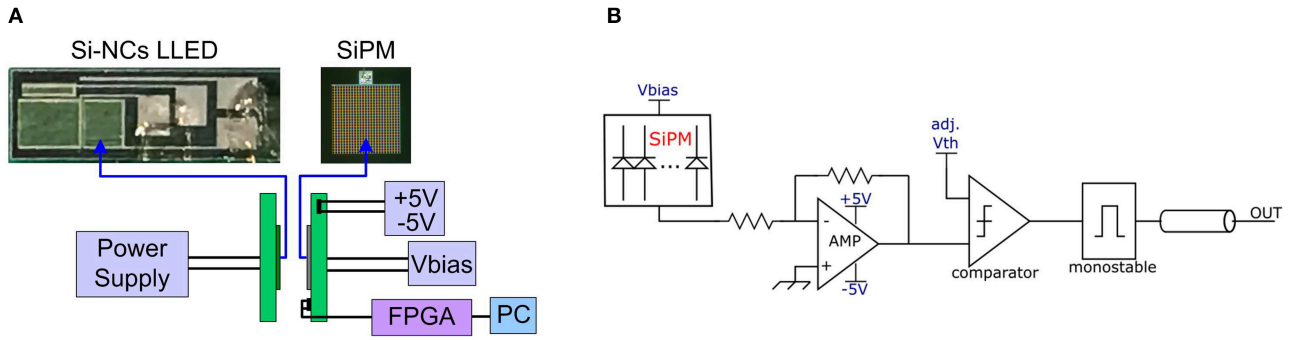

FIGURE 5 | (A) Schematic of the experimental setup with a Si-NCs LLED coupled with a SiPM at a distance of ∼ 1 mm. The SiPM board is connected to ±5 V and a bias voltage (Vbias) is applied to the SiPM. The Si-NCs LLED is driven by an applied current (voltage) provided by the power supply. The output signal of the SiPM is transmitted to an FPGA connected to a PC for the generation of random numbers. **(B)** The front-end board to amplify and digitalize the analog output signal from the detector. This is based on an AD8000 amplifier in a trans-impedance configuration, followed by a comparator with an adjustable voltage threshold (adj.Vth) and a monostable, creating pulses of 3.3 V and 100 ns width.

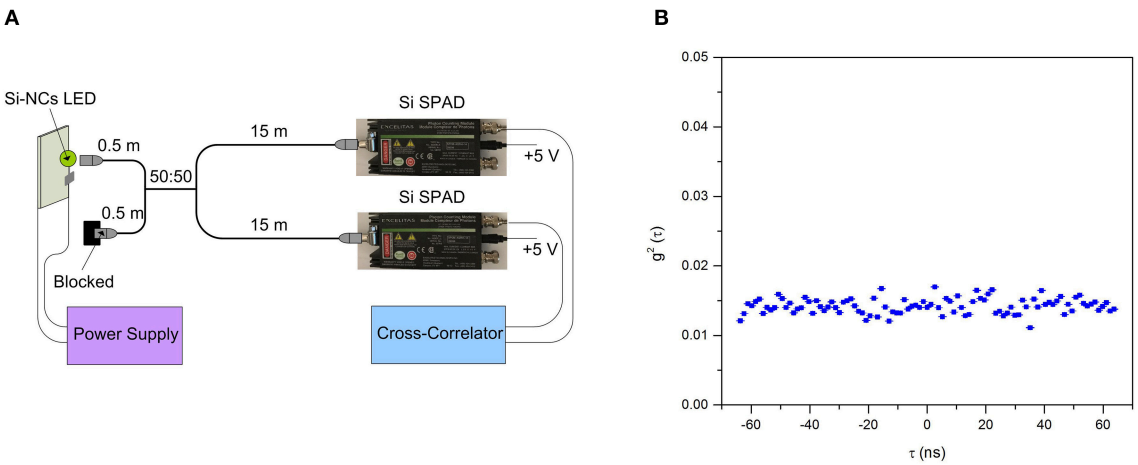

FIGURE 6 | (A) The cross-correlation setup consisting of a 50:50 optical multimode fiber splitter coupled with Si-NCs LED from one of the shorter arms (0.5 m) end and with commerical silicon SPADs from the longer arms (15 m) ends and a linear cross-correlator to perform cross-correlation measurement of the output signals from the silicon SPADs. The other 0.5 m arm is being blocked to light exposure. **(B)** The cross-correlogram of the output pulses. The flat graph indicates that the detected photons follow a Poisson distribution within the resolution of the instrument. The plot is not normalized and the error bars can be seen for some data points.

would be the result of photon bunching. The output signal of the two detectors are then sent to the two channels of a linear-tau cross-correlator having the time resolution of 1.3 ns, where the cross-correlation function, $g^2(\tau)$, is computed. A peak in the cross-correlogram indicates photon bunching while a dip shows anti-bunching. Photon bunching occurs in the case of chaotic or thermal light which has a super-Poissonian distribution with the mean greater than the variance and photon number fluctuations larger than in a coherent light beam. Photon antibunching refers to a sub-Poissonian distribution with the mean lower than the variance and photon number fluctuations smaller than in a coherent light beam [11]. A flat cross-correlogram demonstrates that the photons are emitted independently with a Poisson distribution [12]. Measurement results are presented in **Figure 6B**. As can be seen, a flat cross-correlation graph (with no peak or dip) is observed, which demonstrates that the detected photons follow a Poisson distribution. This is another proof, in addition to the χ^2 statistic [6], that the Poisson distribution is a good match for the distribution of the detected photons which are emitted from the Si-NCs LLED.

In order to characterize afterpulsing and crosstalk in the SiPM, autocorrelation, $g^2(\tau)$, measurements of its signal were performed via a multitau digital correlator with 4 ns resolution [13]. $g^2(\tau)$ exhibits a main peak within ∼140 ns from the main autocorrelation peak at $\tau = 0$ (**Figure 7**). The plateau in $g^2(\tau)$ approaches the normalization value of 1 at about 950 ns.

The measurements for random number generation were performed on the (m)LLED with an active area of ∼ 0.99 mm× 0.82 mm (see **Figure 1A**) which matches the SiPM dimension of 1 mm×1 mm. The applied forward current to LLED was kept below ∼ 45 μA corresponding to the forward voltage of 3 V (see **Figure 2B**) in order to avoid degradation of

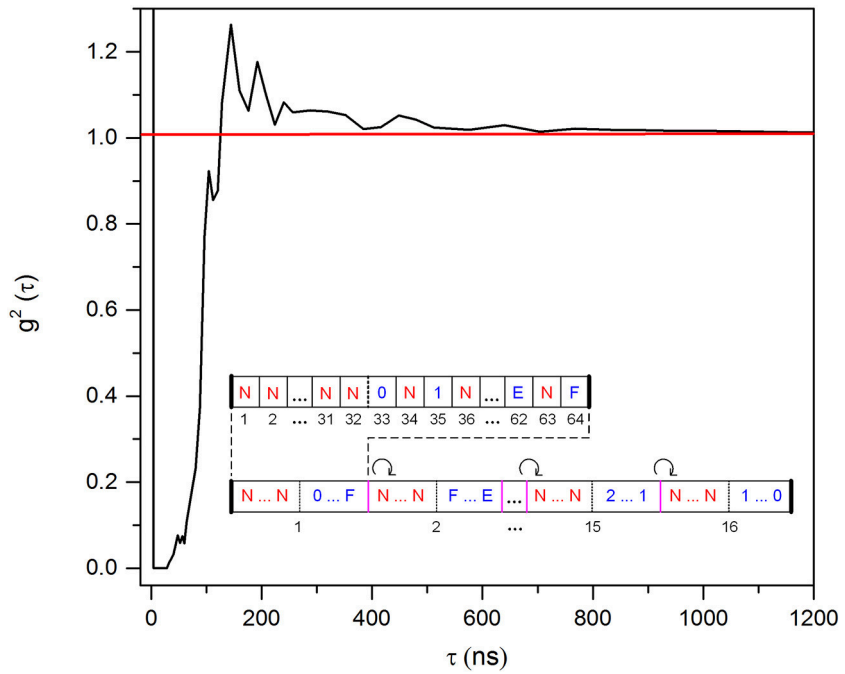

FIGURE 7 | Autocorrelation function ($g^2(\tau)$) of the SiPM signal (peak at zero is out of scale). Dead time and afterpulsing distribution of the SiPM can be seen here. The dead time of ∼110 ns is not due to limitation of the SiPM, but it is set by the monostable in the electronics (front-end shown in **Figure 5B**). The inset shows "super interval" which consists of 16 "double length" intervals with first half of no numbers (N) and second half of alternate hexadecimal symbols and Ns (zoomed in above the "super interval"). Consecutive one-rotation of hexadecimal symbols in the second half of the "double length" intervals is indicated by a circular arrow. The inset is taken from Bisadi et al. [9].

the oxide layer in the active area of the Si-NCs LLED [14]. The V_{bias} to SiPM was 32 V corresponding to an excess bias of ∼6 V ($V_{bd} = 26\ V$) with the DCR of ∼80 kcps/mm^2.

The methodology to generate random numbers is similar to our recent work [9]. It is based on the property of the Poisson statistics that, if an event is observed in a time interval T, the probability that the observation is performed in any subinterval of fixed length of T is uniform. Based on this property and to account for the system limitations, we can describe the methodology by defining "double length" periodic time intervals with an associated fully deterministic "target function". In the case of 16 random number generating subintervals, the alphabet of the symbols is N, 0, 1, ... F, that reads N (no-number), and the hexadecimal numbers 0 to F. Each interval has 32 N subintervals in the first half and an alternation of N subintervals and the full set of numeric symbols in the second half, with a total of 64 subintervals (inset of **Figure 7**). Only if one single detection (event) hits the target function associated with an interval, a random symbol is generated. A mitigation technique is developed in order to improve the non-uniformity in the probability distribution of the generated random symbols. It is called "super interval structure" and is made before the possible arrival of a photon in an interval. As can be seen in the inset of **Figure 7**, it is composed of 16 "double length" intervals in which the random number generating symbols are ordered as 0, 1,... F in the first interval, F, 0, ... E in the second one and so on [9]. This approach results in the nearly uniform probability distribution of the generated symbols (**Figure 9**).

The duration of the "double length" interval is determined by the afterpulsing and crosstalk distribution of the SiPM (**Figure 7**). In order to mask the afterpulsing and crosstalk distribution of SiPM, we needed to set the first half of "double length" interval to ∼950 ns (see **Figure 7**). We considered target functions with "super interval" of lengths 640, 1280, and 1920 ns and studied the autocorrelation coefficient of the generated hexadecimal symbols at time lag 1. It is observed to decrease as the length of "super interval" increases with the values of 1.29×10^{-4}, 1.05×10^{-4} and 1.45×10^{-5} corresponding to the "double length" interval of 640, 1280, and 1920 ns, respectively. Therefore, we fixed the "double length" interval to 1920 ns and acquired sequences of random symbols.

5. EVALUATION OF RANDOMNESS

A very straightforward way to detect an observable pattern among the random symbols or codes is to create a 2-dimensional map of them. A 512 × 512 map of the 16 hexadecimal symbols generated by our methodology from a recording of our system is presented in **Figure 8**. As can be seen clearly, no particular, periodic pattern is observed among the symbols.

Figure 9 shows the probability of generated hexadecimal symbols in a sequence of 1 G symbols. It is seen to follow an uniform distribution (the theoretical value for the probability

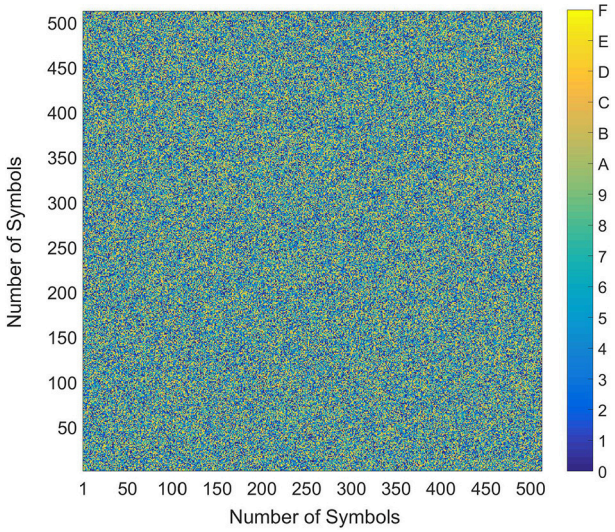

FIGURE 8 | A 512 × 512 map of the hexadecimal symbols. No particular, periodic pattern is observable among the symbols.

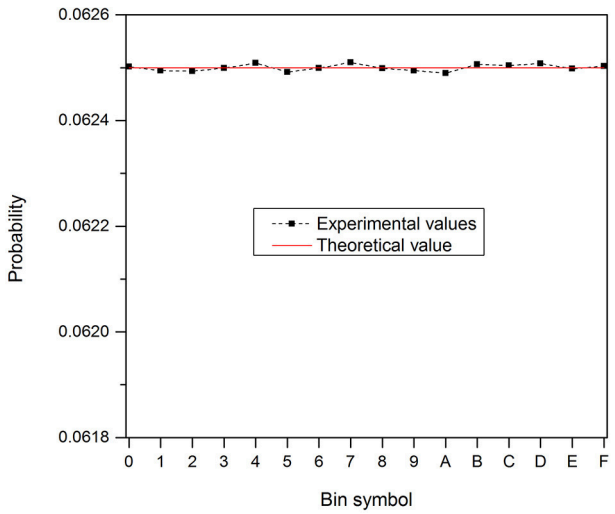

FIGURE 9 | Probability distribution of 16 hexadecimal symbols in a sequence of 1 G symbols raw data. The solid red line shows the theoretical value of 1/16.

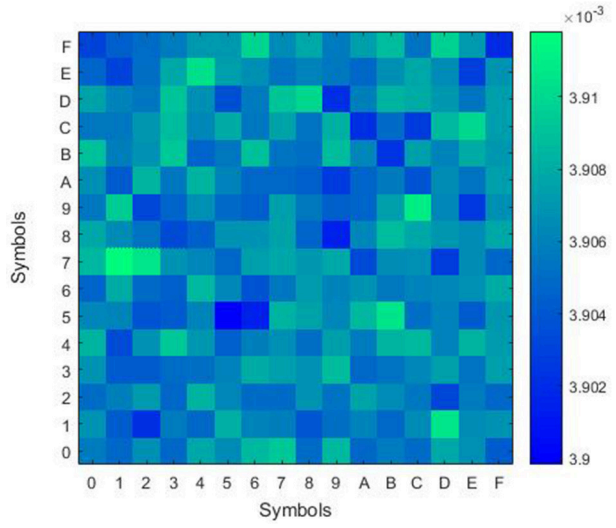

FIGURE 10 | Joint probability mass function for 1 G symbols showing the probability of having each symbol after the other one.

TABLE 2 | NIST tests results for 2 G random bits (2×10^9 bits). The significance level is $\alpha = 0.01$. In order to pass, the p-value should be larger than 0.01 and the proportion should be more than 0.983.

Statistical test	*P*-value	Proportion	Result
Frequency	0.2861	0.9930	Passed
Block frequency	0.2868	0.9935	Passed
Cumulative sum	0.1657	0.9920	Passed
Runs	0.3298	0.9935	Passed
Longest run	0.4817	0.9910	Passed
Rank	0.3611	0.9860	Passed
FFT	0.0401	0.9910	Passed
Non-overlapping template	0.5666	0.9905	Passed
Overlapping template	0.4064	0.9900	Passed
Universal	0.1404	0.9850	Passed
Approximate entropy	0.2854	0.9930	Passed
Random excursions	0.5310	0.9938	Passed
Random excursions variant	0.3127	0.9883	Passed
Serial	0.3376	0.9870	Passed
Linear complexity	0.2550	0.9905	Passed

distribution of 16 bin symbols (1/16) is indicated by a solid red line in **Figure 9**).

The high quality of random symbols is proved through the evaluation of the joint probability mass function (JPMF) [15], which shows a very low deviation of $\sim 5 \times 10^{-6}$ from the expected theoretical value of $(1/16) \times (1/16) = 0.00390625$ (**Figure 10**), and the evaluation of the mutual information (MI) [16], which is calculated to be $\sim 1.5 \times 10^{-7}$ bits considering 1 G random symbols.

To further analyze the quality of generated random numbers, each symbol is replaced with its corresponding 4-bit binary values. In this way, we obtain a binary sequence of random bits. We then apply the 15 statistical tests in the NIST tests suite to the generated raw data. Various datasets with 1 and 2 Gbits length at different applied currents to the (m)LLED were obtained. They all passed the NIST tests without the application of a post-processing algorithm irrespective of the EL variations of the (m)LLED during data acquisition. The results for a dataset of 2 Gbits are tabulated in **Table 2**. The highest experimental bit-rate is calculated to be 0.5 Mbps at the EL intensity of ∼ 550 Kcps.

6. CONCLUSIONS

We realized a compact quantum random number generator with a novel configuration comprising a Si-NCs LLED directly

interfaced with a SiPM without any coupling optics. This paves the way to the further integration of the photon source and the single photon detectors in a single integrated circuits. Indeed, both the devices were fabricated by using the FBK technology. Our research is currently focusing to define a single fabrication process allowing the fabrication of both devices in a single silicon chip.

Remarkably the Si-NCs LLED have similar emission properties and statistics as the standard small Si-NCs which we have previously developed for PQRNG application [6, 9]. Therefore we could use the same robust methodology to extract high quality random numbers which is implemented on a FPGA. The methodology considers the non-idealities of the detector and the source of photons, including parameters (like EL) drifts. The generated high quality random numbers pass all the statistical tests in NIST tests suite without any post-processing. The highest bit rate is 0.5 Mbps with the efficiency of 4-bits per detected photon.

This compact QRNG, with the capability of producing high quality random numbers, can be implemented in small electronic devices providing utmost security accessible to everyone. The proposed device configuration has several advantage with respect to what we already reported in Bisadi et al. [9], particularly with respect to the simplicity of the system (no optics, no thermoelectrical cooler, simple power supply). Still the proposed device can be further optimized by improving the spectral overlap between the LLED and the SiPM and by increasing the parallelization of the Si-NCs LLED/SiPM which can further improve the bit rate to higher values if required by some applications.

AUTHOR CONTRIBUTIONS

ZB prepared the setup, conducted the experiments and analyzed the acquired data. She also made some suggestions to adapt the robust methodology to generate high quality random numbers with the structure. FA partially designed the silicon photomultiplier (SiPM) and characterized it. GF created the robust methodology to generate high quality random numbers and implemented the target function on the FPGA. NZ designed most part of the SiPM. CP supervised the development of the technology used in the SiPM. GP designed and fabricated the large area silicon nanocrystals LED (Si-NCs LLED). LP supervised the whole research work.

ACKNOWLEDGMENTS

This work has been supported by the Provincia Autonoma di Trento via the project "SiQuro."

REFERENCES

1. Hai-Qiang M, Su-Mei W, Da Z, Jun-Tao C, Ling-Ling J, Yan-Xue H, et al. A random number generator based on quantum entangled photon pairs. *Chinese Phys Lett.* (2004) **21**:1961–4. doi: 10.1088/0256-307X/21/10/027
2. Stipčević M, Rogina BM. Quantum random number generator based on photonic emission in semiconductors. *Rev Sci Instrum.* (2007) **78**:045104. doi: 10.1063/1.2720728
3. Stipčević M, Bowers J. Spatio-temporal optical random number generator. *Opt Express.* (2015) **23**:11619–31. doi: 10.1364/OE.23.011619
4. Sanguinetti B, Martin A, Zbinden H, Gisin N. Quantum random number generation on a mobile phone. *Phys Rev X.* (2014) **4**:031056. doi: 10.1103/PhysRevX.4.031056
5. Applegate M, Thomas O, Dynes J, Yuan Z, Ritchie D, Shields A. Efficient and robust quantum random number generation by photon number detection. *Appl Phys Lett.* (2015) **107**:071106. doi: 10.1063/1.4928732
6. Bisadi Z, Meneghetti A, Tomasi A, Tengattini A, Fontana G, Pucker G, et al. Generation of high quality random numbers via an all-silicon-based approach. *Phys Status Solidi* (2016) **213**:3186–93. doi: 10.1002/pssa.201600298
7. Wahl M, Leifgen M, Berlin M, Røhlicke T, Rahn HJ, Benson O. An ultrafast quantum random number generator with provably bounded output bias based on photon arrival time measurements. *Appl Phys Lett.* (2011) **98**:171105. doi: 10.1063/1.3578456
8. Tisa S, Villa F, Giudice A, Simmerle G, Zappa F. High-speed quantum random number generation using CMOS photon counting detectors. *IEEE J Sel Top Quantum Electron.* (2015) **21**:23–9. doi: 10.1109/JSTQE.2014.2375132
9. Bisadi Z, Fontana G, Moser E, Pucker G, Pavesi L. Robust quantum random number generation with silicon nanocrystals light source. *J Lightwave Technol.* (2017) **35**:1588–94. doi: 10.1109/JLT.2017.2656866
10. Acerbi F, Ferri A, Zappala G, Paternoster G, Picciotto A, Gola A, et al. NUV silicon photomultipliers with high detection efficiency and reduced delayed correlated-noise. *IEEE Trans Nucl Sci.* (2015) **62**:1318–25. doi: 10.1109/TNS.2015.2424676
11. Paul H. Photon antibunching. *Rev Mod Phys.* (1982) **54**:1061–102. doi: 10.1103/RevModPhys.54.1061
12. Qu D, Dainty J. A Multichannel Detector for Photon Correlation. *Adv Electron El Phys.* (1988) **74**:107–18. doi: 10.1016/S0065-2539(08)60447-3
13. Kalinin S, Kuhnemuth R, Vardanyan H, Seidel CA. Note: A 4 ns hardware photon correlator based on a general-purpose field-programmable gate array development board implemented in a compact setup for fluorescence correlation spectroscopy. *Rev Sci Instrum.* (2012) **83**:096105. doi: 10.1063/1.4753994
14. Marconi A, Anopchenko A, Wang M, Pucker G, Bellutti P, Pavesi L. High power efficiency in Si-nc/SiO2 multilayer light emitting devices by bipolar direct tunneling. *Appl Phys Lett.* (2009) **94**:221110. doi: 10.1063/1.3147164
15. Grimmett G, Stirzaker D. *Probability and Random Processes.* New York, NY: Oxford University Press (2001).
16. Gray RM. *Entropy and Information Theory.* New York, NY: Springer (2011).

Conflict of Interest Statement: The authors declare that the research was conducted in the absence of any commercial or financial relationships that could be construed as a potential conflict of interest.

frontiers in Physics

ORIGINAL RESEARCH
published: 14 August 2018
doi: 10.3389/fphy.2018.00085

Polarization Rotation and Mode Splitting in Photonic Crystal Line-Defect Waveguides

Moïse Sotto[1], *Isao Tomita*[1,2], *Kapil Debnath*[1,3] *and Shinichi Saito*[1]*

[1] *Sustainable Electronic Technologies, Department of Electronics & Computer Science, Faculty of Physical Sciences and Engineering, University of Southampton, Southampton, United Kingdom,* [2] *Department of Electrical & Computer Engineering, National Institute of Technology, Gifu College, Motosu, Japan,* [3] *Electronics & Electrical Communication Engineering, Indian Institute of Technology, Kharagpur, India*

In a line-defect waveguide of a planer photonic crystal (PhC), we found a new rotational state of polarized light, which exhibits "polarization rotation" on the PhC plane, when a phase mismatch m was added to the air-hole alignment of the waveguide, where mode splitting was simultaneously observed in the dispersion curve. To account for the polarization rotation together with the mode splitting, we propose a two-state model that is constructed from Schrödinger equation obtained from the equation for electromagnetic waves. The proposed two-state model gives an explanation on the relation between the polarization-rotational angle θ and the mismatch m and on its rotational direction (i.e., clockwise or anticlockwise direction) that depends on the mode. Using the two-state model, we also discuss the angular momenta of the polarized light in the PhC waveguide, which are directly related to the Stokes parameters that characterize the polarization rotations.

Keywords: silicon photonics, polarization, photonic crystal, phase mismatch, Stokes parameters

OPEN ACCESS

Edited by:
Michael Mazilu,
University of St Andrews,
United Kingdom

Reviewed by:
Sebastian A. Schulz,
University of St Andrews,
United Kingdom
Venu Gopal Achanta,
Tata Institute of Fundamental Research, India

***Correspondence:**
Shinichi Saito
S.Saito@soton.ac.uk

Specialty section:
This article was submitted to Optics and Photonics, a section of the journal Frontiers in Physics

Received: *01 May 2018*
Accepted: *23 July 2018*
Published: *14 August 2018*

Citation:
Sotto M, Tomita I, Debnath K and Saito S (2018) Polarization Rotation and Mode Splitting in Photonic Crystal Line-Defect Waveguides. Front. Phys. 6:85. doi: 10.3389/fphy.2018.00085

1. INTRODUCTION

In a line-defect waveguide of a planer photonic crystal (PhC), the polarization of light can rotate on the two dimensional PhC plane by addition of a phase mismatch to the air-hole alignment of the waveguide, which occurs without non-linear optical interactions (e.g., optical Kerr effects and photorefractive effects). Originally, the presence of light rotation, given as an optical vortex that carries angular momentum, in photonic bandgap media [1–4] via such non-linear interactions has been found in theoretical and experimental investigations [5–10]; This mechanism is attributed to the localized vortex state induced by those non-linear effects in the bandgap media, which is thus sometimes called a gap vortex. This is an analogous concept to a gap soliton in the bandgap media [11, 12].

However, without such non-linear effects, we can show the presence of a rotational state of polarized light just by adding the mismatch m ($0 < m < a$) to the air-hole alignment of a sidewall of the waveguide [13], as illustrated in **Figure 1**, where a is the air-hole period of the PhC waveguide. Mock et al. also studied the same waveguide [14], but did not report such rotation. They just reported that the light path in the waveguide was "zigzag." An interesting feature of the rotation that we found is that if light propagates from a non-mismatched region to the mismatched region with a gradual mismatch change between them, the light polarization gradually rotates. Here we can define its rotational angle θ for a given m, and as will be shown later, θ is proportional to m (for small m compared with a) via numerical simulations.

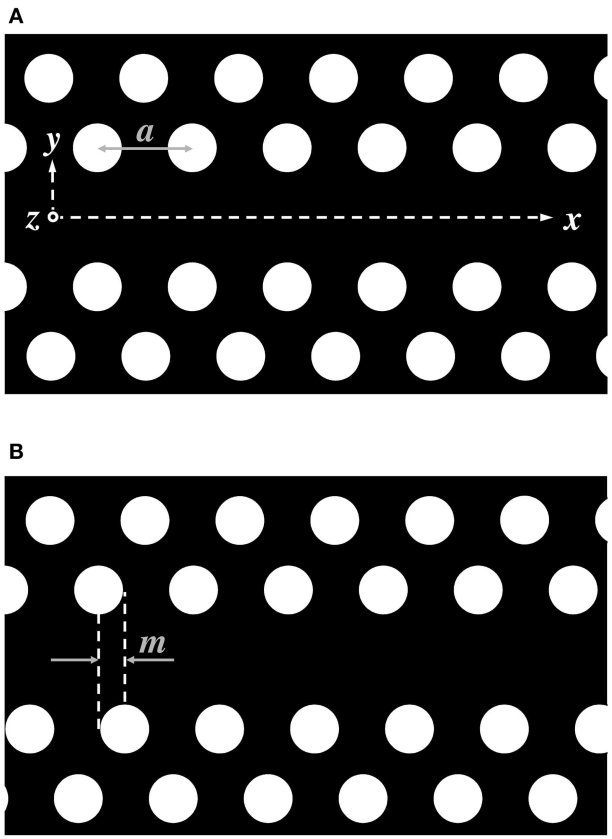

FIGURE 1 | PhC line-defect waveguides, where light propagates through the central part in the *x*-direction. The white circles are air-holes made on a black material (e.g., silicon), where the air-hole spacing (or lattice constant) is *a*, and the air-hole diameter is assumed to be smaller than *a*. **(A)** Air-hole alignments are symmetric with respect to the central line (or the *x*-axis). **(B)** The lower part of the air-hole alignment is shifted with the addition of a mismatch *m*, which causes the polarization rotation of light.

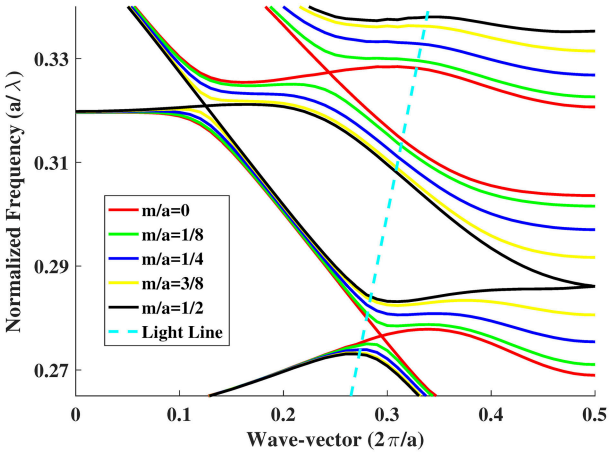

FIGURE 2 | Band structure of the PhC line-defect waveguide. Here, the air-hole period *a* is 450 nm, the air-hole radius is $0.29a$, and the waveguide width is $1.2\sqrt{3}a$. Mode-crossing points exist for $m/a = 0$. As *m* increases (e.g., $m/a = 1/8, 1/4, 3/8, 1/2$), each mode-crossing point splits into two modes (the upper and lower modes) and the split-mode spacing (or gap size) becomes large. The light line for the waveguide with upper and lower air-claddings is indicated by the slanted dashed line.

Moreover, with the addition of m, mode splitting (or level splitting) is observed in the dispersion curve [13, 14], which is created from an originally degenerated mode that contains different polarizations. The main cause of this mode splitting is symmetry breaking; When $m = 0$, structural symmetry in the x and y directions is maintained (despite the presence of a line-defect waveguide at $y = z = 0$), which causes highly degenerated states in the dispersion curve. But, structural symmetry breaking caused by $m \neq 0$ can resolve the degenerated states, creating two split modes, as will be shown in detail in section 2.

We infer from our numerical simulations that the polarization rotation is intimately connected with the mode splitting, because they occur simultaneously, triggered by the addition of m. (Because of the above reasons, the mechanism of the rotational light obtained in our research is completely different from that of a gap vortex with non-linear interactions; the rotation that we found is spatial rotation, not temporal rotation seen for the localized vortex.)

In this paper, we will gain a qualitative understanding of the simultaneous polarization rotation and mode splitting from our two-state model constructed via Schrödinger equation derived from the equation for electromagnetic (EM) waves in the waveguide. In this analysis, we can show that there is a relation between the polarization-rotational angle θ and the mismatch m (via a relation between the mode-splitting spacing ω and the mismatch m), which is an analogous relation to that between an electron-energy-level splitting $\hbar\omega$ and an applied magnetic field B, or $\hbar\omega \propto B$.

In the next section, we will give some numerical simulation results, and then introduce a theory that connects the mode splitting with the polarization rotation within linear optics.

2. NUMERICAL RESULTS FOR MODE SPLITTING AND POLARIZATION ROTATION

Finite-difference time-domain computations [13, 14] show that when $m = 0$, the band structure (or the dispersion curve) of a PhC line-defect waveguide has mode-crossing points, as depicted in **Figure 2**. Each of the mode-crossing points consists of two degenerated modes with different polarizations, which are yielded by band-folding (realized in the reduced zone for the wavenumber k at $-\pi/a \leq k \leq \pi/a$). With the addition of non-zero m, the two-fold degeneracy is resolved (see **Figure 2**), thereby creating two split modes, where the gap size f between the split modes increases with increasing m. (Schematic diagrams of **Figure 3** well describe this behavior, and show that the mode splitting can be regarded as level splitting). The electric fields with different polarizations (with even or odd modes) come to what we call TE_1^- or TE_1^+, respectively, as displayed in **Figure 4** for $k = 0.2925 \times 2\pi/a$ at $m/a = 0, 1/8, 1/4, 3/8, 1/2$. (Much

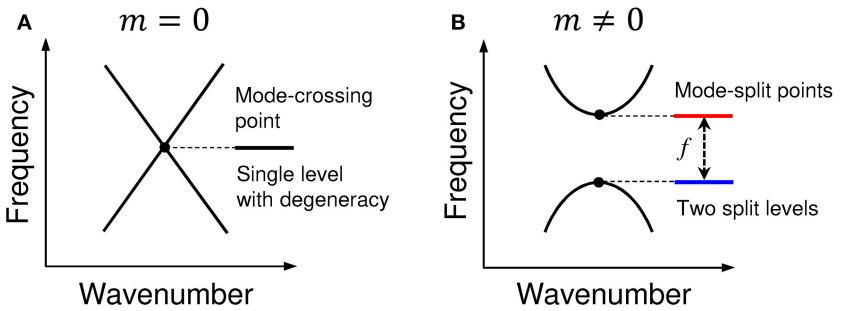

FIGURE 3 | Schematic diagrams for **(A)** a mode-crossing point with $m = 0$, which can be regarded as a single level with degeneracy, and **(B)** mode-split points with $m \neq 0$, which can be looked upon as two split levels.

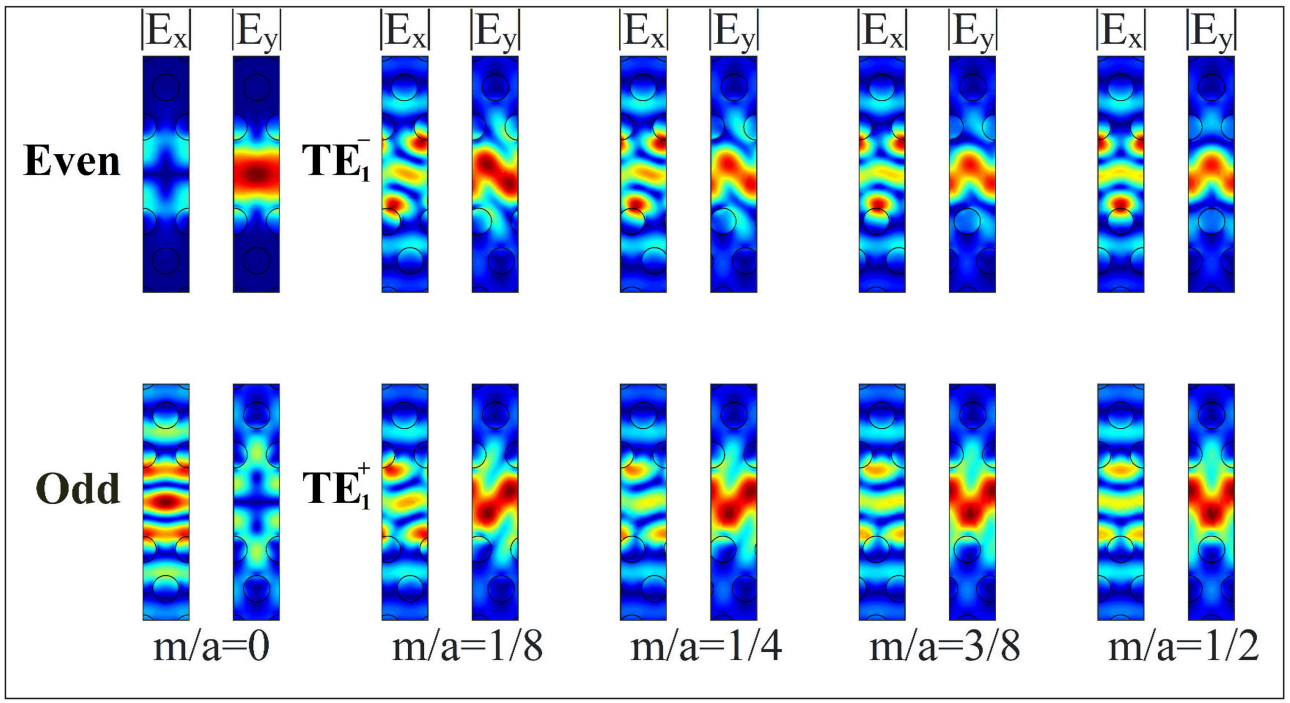

FIGURE 4 | Electric fields with different polarizations that come to the TE_1^-- and TE_1^+-polarizations with even and odd modes, respectively, for $m/a = 0$, 1/8, 1/4, 3/8, 1/2 at $k = 0.2925 \times 2\pi/a$. Here, the absolute value of E_x and E_y is plotted.

clearer polarization rotation can be seen in H_z, and this will also be shown below.)

Figure 5 with the blue (TE_1^+) and red (TE_1^-) curves depicts a calculated m-dependence of the split modes, TE_1^+ and TE_1^-, that correspond to those in **Figure 3B**, which are produced from the lowest degenerated TE_1 mode at 190.13 THz with $k = 0.2925 \times 2\pi/a$. Here, we chiefly focus on the lowest mode (TE_1) because its crossing point at 190.13 THz with $k = 0.2925 \times 2\pi/a$ is placed inside the light cone, that is, the light at that point is a really-propagating mode, not a radiation mode. Also, we observed that a maximum gap size $f_{\max} = 8.68$ THz was obtained at $m/a = 0.5$ and that the splitting behavior was symmetric for (a) $0 < m/a \leq 0.5$ and (b) $0.5 < m/a < 1$. Thus we plotted the figure for Case (a) only, which is sufficient to look at the essence of the behavior. The inset of **Figure 5** shows the m-dependence of the normalized gap size, $f/f_{\max}$. Here, we phenomenologically found that it had good linearity, i.e., $f/f_{\max} = g\,m/a$ ($g = 2.5615$) at $m/a \lesssim 0.3$ (but $f/f_{\max}$ leveled off near $m/a = 0.5$). The $g = 2.5615$ was obtained via the least square fitting with a straight line for the data points at m/a less than or equal to 0.2875. Note that we also observed that the center (say $\bar{\Omega} = (\Omega_0 + \Omega_1)/2$) of the TE_1^+ and TE_1^- modes (say Ω_0 and Ω_1) showed little m-dependence (almost no m-dependence), as indicated by the black dashed curve in **Figure 5** (although $\Omega_1 - \Omega_0 = \omega = 2\pi f$ showed a large m-dependence, as seen in **Figure 5**).

We then give clearer field and intensity profiles of the TE_1^- and TE_1^+ modes for H_z: **Figure 6A** shows the field profile or the real part of H_z in a unit cell at $k = \pi/a$ of the Brillouin-zone

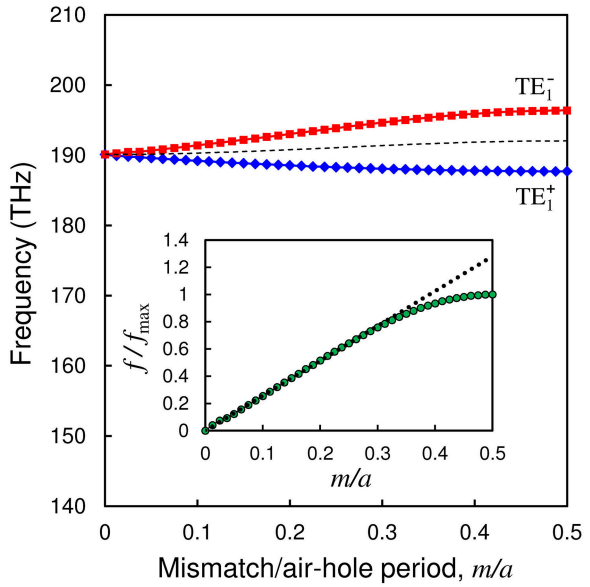

FIGURE 5 | Calculated m-dependence of the two split modes, TE_1^+ (blue curve) and TE_1^- (red curve), produced from a mode-crossing point at 190.13 THz with $k = 0.2925 \times 2\pi/a$ of a degenerated TE_1 mode. The centre of the TE_1^+ and TE_1^- modes has little m-dependence, as indicated by the black dashed curve. The gap size f between the TE_1^+ and TE_1^- modes increases with m, and the maximum gap size f_{max}(= 8.68 THz) is obtained at $m/a = 0.5$. The inset shows the m-dependence of f/f_{max} by the green dots, where the green dots at $m/a \lesssim 0.3$ fit well with the black dashed line with $f/f_{max} = g\,m/a$ ($g = 2.5615$).

(BZ) end, and **Figure 6B** shows the intensity profile $|H_z|^2$ at a mode-crossing point, $k = 0.2925 \times 2\pi/a$. We then observe clearer tilted field and intensity profiles with a tilted angle (or a rotational angle) θ that increases with increasing m. In this case, we found that the rotation of the intensity profiles of TE_1^+ (TE_1^-) in **Figure 6B** was in the anticlockwise (clockwise) direction; A similar tendency remained in the field rotations of **Figure 6A** at the BZ end (since we observed in numerical simulations that the mode-splitting spacing became large even at the BZ end as m increased).

The above results were obtained only from the numerical simulations (i.e., with no theoretical explanations via analytical methods). In the next section, we will explain the observed simultaneous polarization rotation and mode splitting by use of an analytical method with a two-state model derived from the equation for EM waves.

3. ANALYTICAL INTERPRETATION AND DISCUSSION

To derive the two-state model to account for the above phenomena, we start with the following wave equation (obtained from Maxwell's equations) for light propagating in the x direction with polarization E_i:

$$\left(\nabla^2 - \frac{n^2}{c^2}\frac{\partial^2}{\partial t^2}\right) E_i = 0, \tag{1}$$

where $\nabla^2 = \partial^2/\partial x^2 + \partial^2/\partial y^2 + \partial^2/\partial z^2$, n is the refractive index that includes the PhC spatial modulation, and c is the velocity of light.

In the following, we make an approximation that the input-pulse spatial-width $W(> \lambda)$ is larger than the air-hole period a in the waveguide, where the input wavelength λ also needs to suffices $\lambda > a$. This approximation makes it possible to deal with the phenomenon (light rotation) analytically, but cannot well describe it near the PhC band edge because the backward reflection of propagating light is strong due to Bragg reflection with the air-hole arrays. Within the above approximation, *an average nature* of the rotation of light in a size of order $\sim \lambda$ can be obtained.

While keeping the above approximation, we insert $E_i = u_i\, e^{i(\beta x - wt)}$ into Equation (1) and obtain the next Schrödinger equation [15] (see Appendix):

$$i\hbar\,\frac{\partial u_i}{\partial t} = -\frac{\hbar^2}{2n_{\rm eff}}\nabla_2^2\, u_i + V u_i \tag{2}$$

$$\equiv H(t)\, u_i, \tag{3}$$

where we used the notations: $\hbar \equiv \lambda/2\pi$, $t \equiv x$, $V \equiv n_{\rm eff} - n$, $\beta = n_{\rm eff}k = 2\pi\, n_{\rm eff}/\lambda$, $\nabla_2^2 = \partial^2/\partial y^2 + \partial^2/\partial z^2$, and $n_{\rm eff}$ is the effective refractive index in the waveguide. Here we also used the slowly-varying-envelope approximation, $|\partial^2 u_i/\partial x^2| \ll |2\beta\, \partial u_i/\partial x|$. In addition, we omitted a small difference in β for waves with different polarizations (and with the same node numbers). In this situation, we can perfectly utilize ideas and descriptions in quantum mechanics to study the phenomena. Hereafter, we will deal with all quantities in units of $\hbar = c = 1$, as often used in quantum mechanics.

Now we concentrate on the lowest eigenvalue of the right-hand side of Equation (2) when $m = 0$, as described in section 2. In this case, we denote $\bar{\Omega}$ as the lowest eigenvalue, or the lowest frequency at the crossing point (with $m = 0$). When m is added (i.e., $m \neq 0$), since the mode with $\bar{\Omega}$ with degeneracy splits into two modes, we set their eigenvalues to be Ω_0 and Ω_1, where $\Omega_0 = \bar{\Omega} - \omega/2$ and $\Omega_1 = \bar{\Omega} + \omega/2$ with a gap size of $\omega(= 2\pi f)$ between the two split modes, where ω has a large m-dependence but $\bar{\Omega}$ has little m-dependence, as already shown in **Figure 5**.

For those two split modes, the Hamiltonian $H(t)$ in Equation (3) can be written in the matrix representation as

$$\begin{aligned} H(t) &= \begin{pmatrix} \Omega_1 & 0 \\ 0 & \Omega_0 \end{pmatrix} \\ &= \frac{\Omega_1 + \Omega_0}{2}\,\hat{1} + \frac{\Omega_1 - \Omega_0}{2}\,\hat{\sigma_3} \\ &= \bar{\Omega}\,\hat{1} + \omega\,\frac{\hat{\sigma_3}}{2}, \end{aligned} \tag{4}$$

which is known as a two-state model [16]. In Equation (4), $\hat{1}$ is a unit matrix and $\hat{\sigma_3}$ is the z-component of the Pauli matrices ($\hat{\sigma_1}$, $\hat{\sigma_2}$, $\hat{\sigma_3}$):

$$\hat{\sigma_1} = \begin{pmatrix} 0 & 1 \\ 1 & 0 \end{pmatrix}, \quad \hat{\sigma_2} = \begin{pmatrix} 0 & -i \\ i & 0 \end{pmatrix}, \quad \hat{\sigma_3} = \begin{pmatrix} 1 & 0 \\ 0 & -1 \end{pmatrix} \tag{5}$$

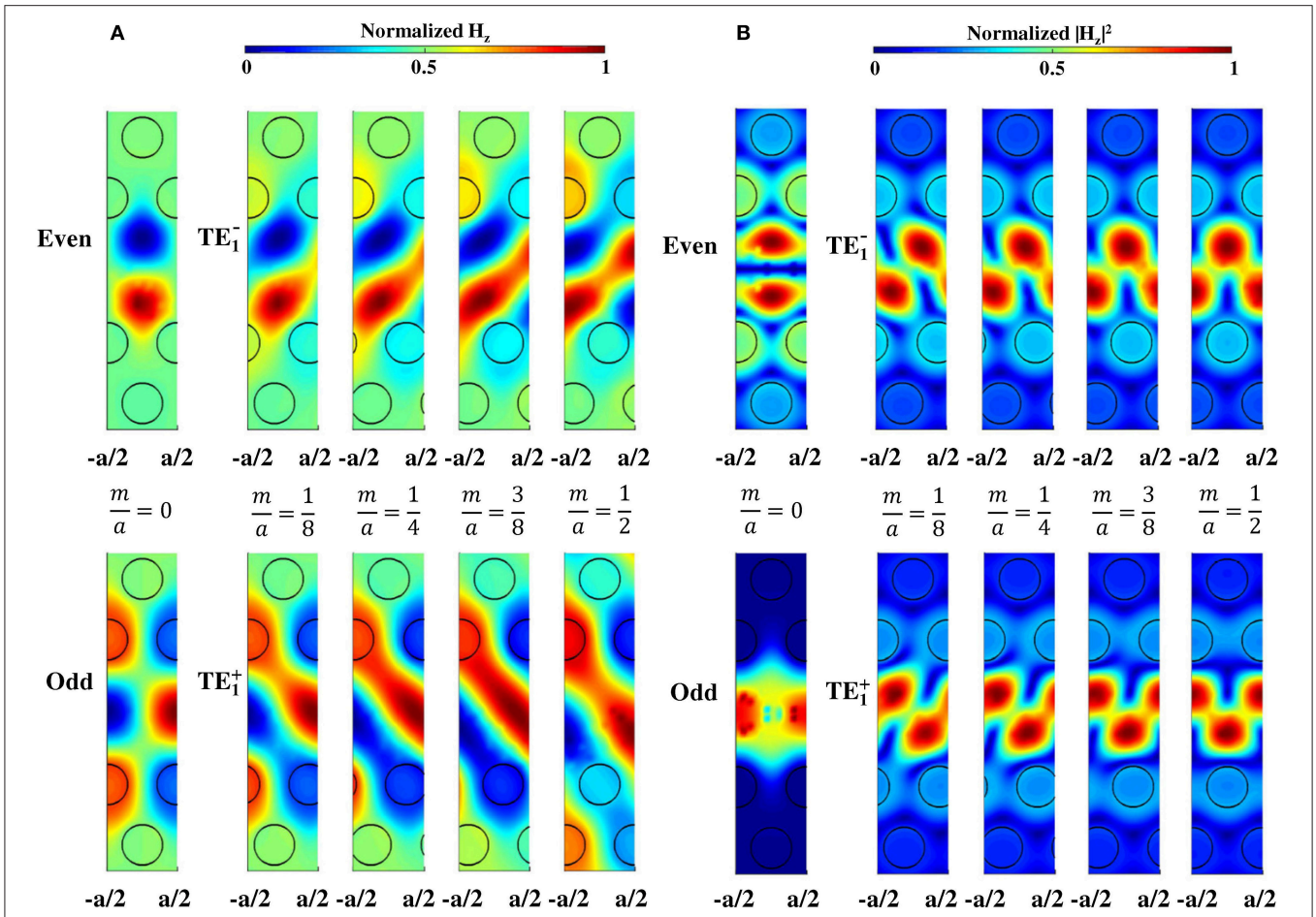

FIGURE 6 | Mode profiles of TE_1^+ and TE_1^- at $m/a = 0, 1/8, 1/4, 3/8, 1/2$ (for odd and even modes). **(A)** Field profile of the real part of H_z at $k = \pi/a$ of the BZ end. **(B)** Intensity $|H_z|^2$ at $k = 0.2925 \times 2\pi/a$ of a crossing point.

that suffice

$$[\hat{\sigma}_i, \hat{\sigma}_j] = 2i\epsilon_{ijk}\hat{\sigma}_k, \tag{6}$$

$$\{\hat{\sigma}_i, \hat{\sigma}_j\} = 2\delta_{ij}\hat{1} \tag{7}$$

and thus

$$\hat{\sigma}_i\hat{\sigma}_j = \delta_{ij}\hat{1} + i\epsilon_{ijk}\hat{\sigma}_k, \tag{8}$$

where $[X, Y] = XY - YX$, $\{X, Y\} = XY + YX$, and i, j, k run from 1 to 3. ϵ_{ijk} is the Levi-Civita symbol, and δ_{ij} is the Kronecker delta. In what follows, we also use the vector notation of Equation (5), i.e., $\hat{\boldsymbol{\sigma}} = (\hat{\sigma_1}, \hat{\sigma_2}, \hat{\sigma_3})$.

For the Hamiltonian (4), the Schrödinger equation is of the form:

$$i\frac{d}{dt}|\phi(t)\rangle = H(t)|\phi(t)\rangle, \tag{9}$$

$$= \left(\bar{\Omega}\,\hat{1} + \omega\frac{\hat{\sigma_3}}{2}\right)|\phi(t)\rangle, \tag{10}$$

where $|\phi(t)\rangle$ is a two-component wave function, or a spinor [17, 18]. (Its detail is described below.) In Equation (10), using the following transformation

$$|\phi(t)\rangle = e^{-i\bar{\Omega}\hat{1}t}|\psi(t)\rangle = e^{-i\bar{\Omega}t}|\psi(t)\rangle, \tag{11}$$

we can simplify the Equation (10) as

$$i\frac{d}{dt}|\psi(t)\rangle = \mathscr{H}(t)|\psi(t)\rangle, \tag{12}$$

where

$$\mathscr{H}(t) = \omega\frac{\hat{\sigma_3}}{2}. \tag{13}$$

In Equation (11), deriving the $e^{-i\bar{\Omega}t}$-term from $|\phi(t)\rangle$ is accepted, because we observed a sizable field/intensity tilt induced by a change in m or ω (because ω has a large m-dependence, but not $\bar{\Omega}$ because $\bar{\Omega}$ has little m-dependence). Thus clearly, we can say that the tilt does not depend on $\bar{\Omega}$. Furthermore, when we calculate the expectation value for an operator $\hat{\mathscr{O}}$, we can rigorously say

that no $\bar{\Omega}$ term contributes to the expectation value: In fact, we obtain via the transformation (11).

$$\langle\hat{\mathscr{O}}\rangle_t = \langle\phi(t)|\hat{\mathscr{O}}|\phi(t)\rangle = \langle\psi(t)|\hat{\mathscr{O}}|\psi(t)\rangle. \tag{14}$$

Further, at the initial state (or at $t = 0$), the next relation holds:

$$|\phi(0)\rangle = |\psi(0)\rangle \equiv |\psi\rangle, \tag{15}$$

where $|\psi\rangle$ is the (time-independent) eigenvector of Equation (13), or a spinor:

$$|\psi\rangle = \begin{pmatrix} u_1 \\ u_2 \end{pmatrix}. \tag{16}$$

Here, u_1 and u_2 are polarized electric fields or wave functions that will come into the TE_1^- mode and TE_1^+ mode, respectively. Equation (16) is almost the same as the Jones vector constructed with polarized electric fields, which is expressed as a spinor with an appropriate basis [19, 20]. There is a slight difference in definition between Equation (16) and the Jones vector defined with plane EM waves, because our EM waves are the waves propagating along the PhC waveguide with different polarization directions; nonetheless, almost the same definition can be used (except for the polarization directions).

The above spinor of a two-state model with Equation (13) can be regarded as that of an electron with spin $\frac{1}{2}$. In this case, as is well-known, the size of ω in Equation (13) is proportional to the strength B of an applied magnetic field, i.e., $\omega \propto B$ (for weak B) [16]. In this situation, we can look upon m as B phenomenologically by help of the "equivalence" between $\omega \propto m$ and $\omega \propto B$ (for small m and B).

Next, to see the time evolution of the system with $\mathscr{H}(t)$, we use the following equation for a unitary operator $U(t)$ [16, 21].

$$i\frac{d}{dt}U(t) = \mathscr{H}(t)U(t). \tag{17}$$

Equation (17) can be derived from the derivative of the identity $U(t)^\dagger U(t) = U(t)U(t)^\dagger = \hat{1}$, that is,

$$i\frac{dU(t)}{dt}U(t)^\dagger = -iU(t)\frac{dU(t)^\dagger}{dt}, \tag{18}$$

which indicates that the left-hand side of Equation (18) is hermitian. If we set this hermitian part as $\mathscr{H}(t)$, Equation (17) can be obtained from Equation (18).

By inserting Equation (13) into Equation (17) and integrating Equation (17) with the initial condition $U(0) = \hat{1}$, we obtain

$$U(t) = \hat{1} - i\int_0^t dt_1\,\mathscr{H}(t_1) + (-i)^2\int_0^t dt_1\int_0^{t_1} dt_2\,\mathscr{H}(t_1)\mathscr{H}(t_2) + \dots \tag{19}$$

$$= \sum_{n=0}^{\infty}(-i)^n\left(\omega\frac{\hat{\sigma_3}}{2}\right)^n\frac{t^n}{n!} \tag{20}$$

$$= e^{-i\omega\frac{\hat{\sigma_3}}{2}t} \tag{21}$$

$$= \hat{1}\cos\frac{\omega t}{2} - i\hat{\sigma_3}\sin\frac{\omega t}{2}, \tag{22}$$

where the time-integration parts have been simply calculated as

$$\int_0^t dt_1\int_0^{t_1} dt_2 \dots \int_0^{t_{n-1}} dt_n = \frac{t^n}{n!} \tag{23}$$

because $\mathscr{H}(t) = \omega\hat{\sigma_3}/2$ has no time-dependence.

In this case, the time-evolution $|\psi(t)\rangle$ of the spinor $|\psi\rangle$ in Equation (16) is of the form:

$$|\psi(t)\rangle = U(t)|\psi\rangle \tag{24}$$

$$= e^{-i\omega\frac{\hat{\sigma_3}}{2}t}|\psi\rangle \tag{25}$$

$$= \left(\hat{1}\cos\frac{\omega t}{2} - i\hat{\sigma_3}\sin\frac{\omega t}{2}\right)|\psi\rangle. \tag{26}$$

where if we interpret that ωt is an angle θ for the polarization rotation, then Equation (26) gives a double-valuedness to u_2 (or u_1) in the θ-rotation. Here, t should be interpreted as *the length* of the interconnection part between the non-mismatched entrance and the mismatched exit (when we use the units of $\hbar = c = 1$); The "t" is a constant when the interconnection length has a fixed value. Even in this situation, θ can vary as m changes because the insertion of $f = gf_{\max}\,m/a$ into $\omega = 2\pi f$ in Equation (26) gives $\theta = \omega t = 2\pi g f_{\max} t\,m/a = \theta_0\,m/a$, where $\theta_0 = 2\pi g f_{\max} t$ is a constant. Inserting $\omega t = \theta$ into Equation (26), we obtain

$$|\psi(\theta)\rangle = \left(\hat{1}\cos\frac{\theta}{2} - i\hat{\sigma_3}\sin\frac{\theta}{2}\right)|\psi\rangle, \tag{27}$$

which provides the relation $|\psi(2\pi)\rangle = -|\psi(0)\rangle$. Furthermore, Equation (27) can explain the aforementioned anticlockwise (clockwise) rotation of the TE_1^+ (TE_1^-) mode, because the explicit expression of Equation (27) with

$$|\psi(\theta)\rangle = \begin{pmatrix} u_1(\theta) \\ u_2(\theta) \end{pmatrix}, \quad |\psi\rangle = \begin{pmatrix} u_1 \\ u_2 \end{pmatrix} \tag{28}$$

is of the form:

$$\begin{pmatrix} u_1(\theta) \\ u_2(\theta) \end{pmatrix} = \begin{pmatrix} e^{-i\theta/2}\,u_1 \\ e^{i\theta/2}\,u_2 \end{pmatrix}. \tag{29}$$

Thus, if $u_2(\theta)$ rotates anticlockwise, then $u_1(\theta)$ rotates clockwise (and vice versa). Note that in terms of $|\phi(t)\rangle$ (not $|\psi(t)\rangle$), we obtain in place of Equation (29):

$$\begin{pmatrix} u_1(\theta) \\ u_2(\theta) \end{pmatrix} = \begin{pmatrix} e^{-i\Theta_0}\,e^{-i\theta/2}\,u_1 \\ e^{-i\Theta_0}\,e^{i\theta/2}\,u_2 \end{pmatrix}, \tag{30}$$

where $\Theta_0 = \bar{\Omega}\,t$ is a constant when the "length" t is a constant, as described above. If $m = 0$, then $\theta = 0$, but Θ_0 remains as a constant (because $\bar{\Omega}$ in Θ_0 has (almost) no m-dependence); in this case (or $m = 0$), Equation (30) becomes

$$\begin{pmatrix} u_1(0) \\ u_2(0) \end{pmatrix} = \begin{pmatrix} e^{-i\Theta_0}\,u_1 \\ e^{-i\Theta_0}\,u_2 \end{pmatrix}. \tag{31}$$

Equation (31) corresponds to the zero-m fields, as given at the leftmost ones in **Figure 6A**. We can see that adjusting the

parameter "t" in Θ_0 of Equation (31) enables setting various initial polarized states at $m = 0$. We should examine the field tilt for $m \neq 0$ as a difference from those initial field profiles, $(u_1(0)\ u_2(0))$, and thus what we should look upon as a field tilt is given by

$$\begin{pmatrix} u_1(\theta) \\ u_2(\theta) \end{pmatrix} = \begin{pmatrix} e^{-i\theta/2}\, u_1(0) \\ e^{i\theta/2}\, u_2(0) \end{pmatrix}, \tag{32}$$

and hence we obtain the same result as that in Equation (29).

As for the evolution of the angular momentum operator $\hat{\boldsymbol{\sigma}}$, we can calculate it as

$$\hat{\boldsymbol{\sigma}}(t) = U^{\dagger}(t)\hat{\boldsymbol{\sigma}}\, U(t). \tag{33}$$

Using Equations (21),(33), we obtain

$$\begin{pmatrix} \hat{\sigma_1}(t) \\ \hat{\sigma_2}(t) \\ \hat{\sigma_3}(t) \end{pmatrix} = \begin{pmatrix} \cos\omega t & -\sin\omega t & 0 \\ \sin\omega t & \cos\omega t & 0 \\ 0 & 0 & 1 \end{pmatrix} \begin{pmatrix} \hat{\sigma_1} \\ \hat{\sigma_2} \\ \hat{\sigma_3} \end{pmatrix}, \tag{34}$$

where Equations (8),(22) have been used in the calculations. For convenience, we rewrite Equation (34) as

$$\hat{\sigma_i}(t) = a_{ij}(t)\hat{\sigma_j}, \tag{35}$$

where j is a dummy index and runs from 1 to 3. Since $\hat{\sigma_i}$ is defined in the $SU(2)$ space [22], it is not yet related to a vector in our *real* space, i.e., in the $SO(3)$ space.

Next, we show how a vector rotating in $SO(3)$ space is related to $\hat{\sigma_i}$ in the $SU(2)$ space. To perform this, we start with the following Schrödinger equation:

$$i\frac{d}{dt}|\psi(t)\rangle = \mathscr{H}(t)|\psi(t)\rangle, \tag{36}$$

$$i\frac{d}{dt}|\psi(t)\rangle - \mathscr{H}(t)|\psi(t)\rangle = 0. \tag{37}$$

By multiplying $\langle\psi(t)|\hat{\sigma_i}$ from the left to Equation (37), we obtain

$$i\langle\psi(t)|\hat{\sigma_i}\frac{d}{dt}|\psi(t)\rangle - \frac{\omega}{2}\langle\psi(t)|\hat{\sigma_i}\hat{\sigma_3}|\psi(t)\rangle = 0, \tag{38}$$

where Equation (13) was also used. We then multiply $\hat{\sigma_i}|\psi(t)\rangle$ from the right to the hermitian conjugate of Equation (37) and obtain

$$-i\left(\frac{d}{dt}\langle\psi(t)|\right)\hat{\sigma_i}|\psi(t)\rangle - \frac{\omega}{2}\langle\psi(t)|\hat{\sigma_3}\hat{\sigma_i}|\psi(t)\rangle = 0. \tag{39}$$

By subtracting Equation (39) from Equation (38), we have

$$i\frac{d}{dt}\langle\psi(t)|\hat{\sigma_i}|\psi(t)\rangle - \frac{\omega}{2}\langle\psi(t)|[\hat{\sigma_i},\hat{\sigma_3}]|\psi(t)\rangle = 0, \tag{40}$$

$$i\frac{d}{dt}\langle\psi(t)|\hat{\sigma_i}|\psi(t)\rangle + i\epsilon_{ij3}\langle\psi(t)|\hat{\sigma_j}|\psi(t)\rangle\omega = 0, \tag{41}$$

where $[\hat{\sigma_i},\hat{\sigma_3}] = 2i\epsilon_{i3k}\hat{\sigma_k} = -2i\epsilon_{ij3}\hat{\sigma_j}$ was used. In Equation (41), $\langle\psi(t)|\hat{\sigma_i}|\psi(t)\rangle$ is an expectation value of $\hat{\sigma_i}$ at "time" t and is observed as a vector in the $SO(3)$ space. Also, we can show that $\langle\psi(t)|\hat{\sigma_i}|\psi(t)\rangle$ is actually proportional to $M_i(t)$ of a general vector $\boldsymbol{M}(t)$ rotating in the $SO(3)$ space, where it suffices the same-form equation as Equation (41):

$$\frac{d}{dt}M_i(t) + \epsilon_{ij3}M_j(t)\,\omega = 0 \tag{42}$$

that is obtained [23] from

$$\frac{d}{dt}\boldsymbol{M}(t) - \boldsymbol{\omega}\times\boldsymbol{M}(t) = 0, \tag{43}$$

where $\boldsymbol{M}(t)$ is fixed in a moving system with an angular frequency vector $\boldsymbol{\omega} = \omega\boldsymbol{e}_3$ and $\boldsymbol{e}_3$ is a unit vector in the $\boldsymbol{e}_3$-direction. Furthermore, in order to check the transformation property of $\langle\psi(t)|\hat{\sigma_i}|\psi(t)\rangle$, by use of $|\psi(t)\rangle = U(t)|\psi\rangle$, we get

$$\langle\psi(t)|\sigma_i|\psi(t)\rangle = \langle\psi|U^{\dagger}(t)\sigma_i U(t)|\psi\rangle \tag{44}$$

$$= a_{ij}(t)\langle\psi|\sigma_j|\psi\rangle. \tag{45}$$

This means that $\langle\psi(t)|\sigma_i|\psi(t)\rangle$ is a vector that transforms via $a_{ij}(t)$, i.e., the rotation in $SO(3)$. In the above, we have assumed $\omega t = \theta$ since its use in Equations (27),(29). Thus, we consistently use it in the rotation of the angular momentum. We then obtain

$$\begin{pmatrix} \langle\hat{\sigma_1}\rangle_\theta \\ \langle\hat{\sigma_2}\rangle_\theta \\ \langle\hat{\sigma_3}\rangle_\theta \end{pmatrix} = \begin{pmatrix} \cos\theta & -\sin\theta & 0 \\ \sin\theta & \cos\theta & 0 \\ 0 & 0 & 1 \end{pmatrix} \begin{pmatrix} \langle\hat{\sigma_1}\rangle \\ \langle\hat{\sigma_2}\rangle \\ \langle\hat{\sigma_3}\rangle \end{pmatrix} \tag{46}$$

as the explicit matrix representation of Equation (45), where $\langle\sigma_i\rangle = \langle\psi|\sigma_i|\psi\rangle$ and $\langle\sigma_i\rangle_\theta = \langle\psi(t)|\sigma_i|\psi(t)\rangle$ with $\omega t = \theta$ (or $\langle\sigma_i\rangle_\theta = \langle\psi(\theta)|\sigma_i|\psi(\theta)\rangle$). The relation of $\langle\sigma_i\rangle_\theta$ with the electric fields is easily obtained from the direct calculations of $\langle\sigma_i\rangle_\theta = \langle\psi(\theta)|\sigma_i|\psi(\theta)\rangle$ with Equations (5),(28):

$$\langle\hat{\sigma_1}\rangle_\theta = u_1^*(\theta)u_2(\theta) + u_1(\theta)u_2^*(\theta)$$

$$= 2\,\mathrm{Re}(u_1^*(\theta)u_2(\theta)) \equiv S_2, \tag{47}$$

$$\langle\hat{\sigma_2}\rangle_\theta = -iu_1^*(\theta)u_2(\theta) + iu_1(\theta)u_2^*(\theta)$$

$$= 2\,\mathrm{Im}(u_1^*(\theta)u_2(\theta)) \equiv S_3, \tag{48}$$

$$\langle\hat{\sigma_3}\rangle_\theta = |u_1(\theta)|^2 - |u_2(\theta)|^2 \equiv S_1, \tag{49}$$

where S_1, S_2, and S_3 are the Stokes parameters that characterize polarization rotations [24, 25]. The electric-field intensity relates to the rest (S_0) of the Stokes parameters:

$$\langle\hat{1}\rangle_\theta = |u_1(\theta)|^2 + |u_2(\theta)|^2 \equiv S_0. \tag{50}$$

Note that the rotation of the angular momentum in Equation (46) shows a single-valuedness with respect to θ, which is completely different from the double-valuedness of the wave function $|\psi(\theta)\rangle$; If we treated an electron of spin $\frac{1}{2}$, $|\psi(\theta)\rangle$ would be the wave function of the electron, and the angular-momentum motion would correspond to spin precession [26].

In this paper, we have pointed out the "equivalence" between the PhC line-defect waveguide with an added phase mismatch m

and the spin-half electron with an applied magnetic field B. In particular, the EM wave equation in the PhC waveguide could be reduced to the Schrödinger equation; Both systems showed the same *two-level* splitting and had the split mode or level spacing in proportion to the size of the perturbation, m or B. At the present stage of the theory with some approximations, we cannot prove the "equivalence" mathematically, but we showed it from some supporting evidence. A further development of the theory with much less approximations will be able to explain the equivalence.

4. SUMMARY

Using the Schrödinger equation derived from the EM wave equation, we have built a two-state model that can explain the observed polarization rotation and mode splitting that occur simultaneously when a phase mismatch m is added to a PhC line-defect waveguide. The theory has given a double-valuedness to the light field (or the wave function) with different polarizations and a single-valuedness to the motion of angular momenta. Using a spinor representation, the former has explained the difference in the rotational direction (i.e., clockwise or anticlockwise direction) of TE_1^- or TE_1^+ mode, and the latter has clarified the relation between the angular momenta and the Stokes parameters that define the polarization rotations. Also, the theory has given a relation between the rotational angle θ and the mismatch m for small m (via the numerical result between f and m). In this analysis, the "equivalence" between both systems has been indicated for the light field with two split modes and the electron wave function with two split levels and for the light angular motion and the electron spin precession.

AUTHOR CONTRIBUTIONS

MS proposed the idea to introduce the mismatch. MS, IT, and SS developed theories. MS and KD conducted photonic crystal simulations. IT drafted the main text. All authors contributed to discussions.

FUNDING

This work is supported by EPSRC Standard Grant (EP/M009416/1), EPSRC Manufacturing Fellowship (EP/M008975/1), and EPSRC Platform Grant (EP/N013247/1).

ACKNOWLEDGMENTS

We are grateful to Prof. H. N. Rutt for his constructive comments. The data from the paper can be obtained from the University of Southampton ePrint research repository: doi: https://doi.org/10.5258/SOTON/D0503.

REFERENCES

1. Yablonovitch E. Inhibited spontaneous emission in solid-state physics and electronics. *Phys Rev Lett*. (1987) **58**:2059–62.
2. John S. Strong localization of photons in certain disordered dielectric superlattices. *Phys Rev Lett*. (1987) **58**:2486–9.
3. Yablonovitch E. Photonic crystals: semiconductors of light. *Sci Am*. (2001) **285**:46–55. doi: 10.1038/scientificamerican1201-46
4. Joannopoulos JD, Johnson SG, Winn JN, Meade RD. *Photonic Crystals - Molding the Flow of Light*. Princeton, NJ: Princeton University Press (2008).
5. Musslimani ZH, Yang J. Self-trapping of light in a two-dimensional photonic lattice. *J Opt Soc Am B* (2004) **21**:973–81. doi: 10.1364/JOSAB.21.000973
6. Bartal G, Manela O, Cohen O, Fleischer JW, Segev M. Observation of second-band vortex solitons in 2D photonic lattices. *Phys Rev Lett*. (2005) **95**:053904. doi: 10.1103/PhysRevLett.95.053904
7. Richter T, Kaiser F. Anisotropic gap vortices in photorefractive media. *Phys Rev A* (2007) **76**:033818 . doi: 10.1103/PhysRevA.76.033818
8. Song D, Lou C, Tang L, Wang K, Li W, Chen X, et al. Self-trapping of optical vortices in waveguide lattices with a self-defocusing nonlinearity. *Opt Express* (2008) **16**:10110–6. doi: 10.1364/OE.16.010110
9. Wang J, Yang J. Families of vortex solitons in periodic media. *Phys Rev A* (2008) **77**:033834. doi: 10.1103/PhysRevA.77.033834
10. Zhang Z, Ma D, Zhang Y, Cao M, Xu Z, Zhang Y. Propagation of optical vortices in a nonlinear atomic medium with a photonic band gap. *Opt Lett*. (2017) **42**:1059–62. doi: 10.1364/OL.42.001059
11. Mills DL, Trullinger SE. Gap solitons in nonlinear periodic structures. *Phys Rev B* (1987) **36**:947–52.
12. Chen W, Mills DL. Gap solitons and the nonlinear optical response of superlattices. *Phys Rev Lett*. (1987) **58**:160–3.
13. Sotto M, Debnath K, Khokhar AZ, Tomita I, Thomson D, Saito S. Photonic bonding modes with circular polarization at zero-group-velocity points. In: *The 15th International Conference on Group IV Photonics*. Cancun:IEEE (2018).
14. Mock A, Lu L, O'Brien J. Space group theory and Fourier space analysis of two-dimensional photonic crystal waveguides. *Phys Rev B* (2010) **81**:155115. doi: 10.1103/PhysRevB.81.155115
15. Longhi S. Quantum-optical analogies using photonic structures. *Laser Photon Rev*. (2009) **3**:243–61. doi: 10.1002/lpor.200810055
16. Sakurai JJ. *Modern Quantum Mechanics*. New York, NY: Addison-Wesley Publishing Co., Inc. (1985).
17. Greiner W. *Quantum Mechanics: An Introduction*. Heidelberg: Springer (2001).
18. Cartan E. *The Theory of Spinors*. Cambridge: The MIT Press (1966).
19. Castillo G, Garcia IR. The Jones vector as a spinor and its representation on the Poincare sphere. *Rev Mex Fis*. (2011) **57**:406–13.
20. Castillo G. Spinor representation of an electromagnetic plane wave. *J Phys A Math Theor*. (2008) **41**:115302. doi: 10.1088/1751-8113/41/11/115302
21. Takahashi Y. *Mathematics for Physics I, II*. Tokyo: Koudansha Co., Inc. (1993).
22. Georgi H. *Lie Algebras In Particle Physics: from Isospin To Unified Theories*. London: Benjamin/Cummings Publishing Co., Inc. (1982).
23. Landau LD, Lifshitz EM. *Mechanics*. New York, NY: Pergamon Press (1976).
24. Jackson JD. *Classical Electrodynamics*. New York, NY: John Wiley and Sons, Inc. (1999).
25. Milione G, Sztul HI, Nolan DA, Alfano RR. Higher-order Poincare sphere, Stokes parameters, and the angular momentum of light. *Phys Rev Lett*. (2011) **107**:053601. doi: 10.1103/PhysRevLett.107.053601
26. Tomonaga S. *The Story of Spin*. Chicago, IL: University of Chicago Press (1998).

Conflict of Interest Statement: The authors declare that the research was conducted in the absence of any commercial or financial relationships that could be construed as a potential conflict of interest.

The reviewer SS and handling editor declared their shared affiliation.

APPENDIX

To derive the Schrödinger equation from the wave equation, we insert $E_i = u_i\, e^{i(\beta x - wt)}$ into

$$\left(\nabla^2 - \frac{n^2}{c^2}\frac{\partial^2}{\partial t^2}\right) E_i = 0, \tag{A1}$$

and obtain

$$\nabla_2^2\, u_i\, e^{i(\beta x - wt)} + \frac{\partial^2 u_i}{\partial x^2} e^{i(\beta x - wt)} + 2i\beta \frac{\partial u_i}{\partial x} e^{i(\beta x - wt)} + \left(\frac{n^2}{c^2} w^2 - \beta^2\right) u_i\, e^{i(\beta x - wt)} = 0, \tag{A2}$$

where $\nabla_2^2 = \partial^2/\partial y^2 + \partial^2/\partial z^2$ and $\beta = n_{\text{eff}} k = 2\pi\, n_{\text{eff}}/\lambda$, k is the wavenumber in vacuum, and w is the angular frequency.

By use of the slowly-varying-envelope approximation, $|\partial^2 u_i/\partial x^2| \ll |2\beta\, \partial u_i/\partial x|$, Equation (A2) is of the form:

$$\nabla_2^2\, u_i + 2i\beta \frac{\partial u_i}{\partial x} + \left(\frac{n^2}{c^2} w^2 - \beta^2\right) u_i = 0. \tag{A3}$$

By substituting $\beta = n_{\text{eff}} k$ for Equation (A3) and using an approximation, $|n - n_{\text{eff}}| \ll n + n_{\text{eff}}$, we obtain

$$i\lambda\!\!\!^{-} \frac{\partial u_i}{\partial x} = -\frac{\lambda\!\!\!^{-2}}{2n_{\text{eff}}} \nabla_2^2\, u_i + (n_{\text{eff}} - n) u_i, \tag{A4}$$

where $\lambda\!\!\!^{-} = \lambda/2\pi$. In Equation (A4), by setting $\hbar = \lambda\!\!\!^{-}$, $V = n_{\text{eff}} - n$, we finally get

$$i\hbar \frac{\partial u_i}{\partial t} = -\frac{\hbar^2}{2n_{\text{eff}}} \nabla_2^2\, u_i + V u_i. \tag{A5}$$

frontiers in Physics

ORIGINAL RESEARCH
published: 24 March 2021
doi: 10.3389/fphy.2021.646228

Poincaré Rotator for Vortexed Photons

*Shinichi Saito**

Center for Exploratory Research Laboratory, Research & Development Group, Hitachi, Ltd., Tokyo, Japan

A Poincaré sphere is a powerful prescription to describe a polarized state of coherent photons, oscillating along certain directions. The polarized state is described by a vector in the sphere, and various passive optical components, such as polarization plates and quartz rotators are able to rotate the vectorial state by changing the phase and the amplitude among two orthogonal basis states. The polarization is originated from spin of photons, and recently, significant attentions have been made for optical Orbital Angular Momentum (OAM) as another fundamental degree of freedom for photons. The beam shape of photons with OAM is a vortex with a topological charge at the core, and the state of vortexed photons can be described by a hyper-Poincaré sphere. Here, we propose a compact Poincaré rotator, which controls a vortexed state of photons in a silicon photonic platform, based on Finite-Difference Time-Domain (FDTD) simulations. A ring-shaped gear is evanescently coupled to two silicon photonic waveguides, which convert optical momentum to OAM with both left and right vortexed states. By controlling the relative phase and the amplitude of two traveling waves in input ports, we can control the vortexed states in the hyper-Poincaré sphere for photons out of the gear. The impact of the geometrical Pancharatnam-Berry-Guoy's phase and the conservation law of spin and OAM for vortexed photons out of the gear are discussed.

Keywords: orbital angular momentum, vortex, Poincaré sphere, stokes parameter, silicon photonics

OPEN ACCESS

Edited by:
Guangcan Guo,
University of Science and Technology of China, China

Reviewed by:
Hailu Luo,
Hunan University, China
Satoshi Iwamoto,
The University of Tokyo, Japan

***Correspondence:**
Shinichi Saito
shinichi.saito.qt@hitachi.com

Specialty section:
This article was submitted to Optics and Photonics, a section of the journal Frontiers in Physics

Received: *25 December 2020*
Accepted: *23 February 2021*
Published: *24 March 2021*

Citation:
Saito S (2021) Poincaré Rotator for Vortexed Photons. Front. Phys. 9:646228. doi: 10.3389/fphy.2021.646228

1. INTRODUCTION

Planck discovered momentum p of a photon is determined by its wavelength λ in a vacuum as

$$p = \frac{h}{\lambda} = \hbar\frac{2\pi}{\lambda} = \hbar k, \tag{1}$$

where h is the Plank constant [1], $\hbar = h/(2\pi)$is the Dirac constant [2], and k is the wavenumber, through investigations on black body radiation [3, 4]. This discovery was a landmark for the development of quantum mechanics, which is based on fundamental principles of all elementary particles [5–7]. The quantization condition of the Plank formula was further refined by the Bohr-Sommerfeld model [3, 4, 8, 9],

$$\oint_C \mathbf{p} \cdot d\mathbf{q} = nh, \tag{2}$$

where $\mathbf{q}$ is a generalized coordinate, which is the conjugate of the momentum $\mathbf{p}$ for a counter integration along a closed loop of C, and n is a quantum number for this orbital. By applying the quantization condition for the orbitals of electrons in an atom, the electronic structures

were systematically classified by radial and azimuthal quantum numbers for energy and angular momentum to explain various material properties based on atomic orbitals for the periodic table [3, 4, 8, 9]. In modern quantum mechanics, momentum and angular momentum are understood based on generators of translational and rotational symmetries of the system [5–7, 10–13]. It is interesting to be aware that both photons and electrons are characterized by integer quantum numbers of orbitals, regardless of the difference in statistics governed by Bose-Einstein and Fermi-Dirac distribution functions, respectively [14–18].

Despite its historical importance on the nature of photons, it is relatively recent to pay attention to optical Orbital Angular Momentum (OAM) [19–46]. Allen et al. showed that the optical beam with Laguerre-Gauss mode carry OAM of $\hbar m$ per photon along the direction of propagation, where m is the integer quantum number to characterize the helical rotation of the phase front [19]. In order to allow the finite OAM ($|m| \neq 0$), the amplitude of the Laguerre-Gauss mode must have nodes at the core, and m is the winding number of the phase along the closed contour perpendicular to the direction of propagation [19, 32, 33, 47–49]. m is also called as a topological charge [19, 21, 22, 26, 32, 33, 35, 38, 39]. From fundamental points of views, it was argued whether it is possible to split spin angular momentum and OAM from the total angular momentum defined from the Poynting vector [24], or not [20, 27, 34]. This issue is posing a critical question whether we can treat OAM as a similar degree of freedom with polarization [50, 51] for internal spin degree of freedom. It is beyond our scope of this paper to explore the splitting issue of spin and OAM in a rigorous way [20, 27, 34].

Practically, however, it is well-established that a state with OAM is described in a hyper-Poincaré sphere [21, 28, 36, 37] similar to a Poincaré sphere [52–54] for visualizing Stokes parameters [47, 48, 52, 54–64] of polarization states. Polarization states are described by two level systems corresponding to an arbitrary orthogonal states, such as left ($|\mathrm{L}\rangle$) and right ($|\mathrm{R}\rangle$) circularly polarized states, horizontally ($|\mathrm{H}\rangle$) and vertically ($|\mathrm{V}\rangle$) linear-polarized states, or diagonally ($|\mathrm{D}\rangle$) and anti-diagonally ($|\mathrm{A}\rangle$) polarized linear-polarized states [47, 48, 52, 54–64]. We can also consider corresponding states with OAM in the hyper-Poincaré sphere [21, 28, 36, 37]. We propose to call a beam with OAM as *vortexed* in a close similarity to polarized photons.

Padgett and Courtial proposed to use a hyper-Poincaré sphere by using a superposition states of left- and right- vortexed states, and demonstrated such a superposition state is controlled by a phase-shift, generated by rotated cylindrical lenses [21, 65]. In the definition of the work of Padgett and Courtial [21], the duality between vortexed states and polarized states was discussed in general, and the polarization state of the vortexed state was not specified. Thus, the superposition of left- and right vortexed states with a certain fixed polarization state was considered [21]. Later, Milione et al. clarified the polarization states for photons with OAM, and showed rich vortexed states could be realized by allowing the superposition states of orthogonally polarized states with a proper OAM [28]. Here, instead of considering left- and right-vortexed states, arbitrary polarized states with a certain vortexed state were clarified, and the further superposition states with different OAM states were also discussed [28]. More recently, several groups successfully generated arbitrary OAM states by transferring polarized states to vortexed states [36, 37, 66].

In order to change the polarized state in Poincaré sphere, we can utilize various passive and active optical components, such as retarder plates, phase-shifters, Mach-Zehnder modulators, quartz rotators and so on [48, 50, 51, 60, 62, 64]. We can also use several optical components, such as vortex retarders [25, 31] and novel micro-gears [29, 67–69] for the generations of beams with OAM.

In particular, the micro-gears [29, 68, 69] in a silicon (Si) photonic platform [70, 71] are promising to encode various vortexed states, such as amplitudes, phases, and vorticities (topological charges) for high-speed optical communications [72] as well as for potential quantum communications [46].

Nevertheless, it is not so straightforward to manipulate vortexed states dynamically for photons in the hyper-Poincaré sphere, compared with the polarized photons without OAM, due to the lack of appropriate phase-shifters and rotators for OAM, compared with those for polarization.

Motivated by these fundamental progresses on OAM and practical advances in Si photonics, here, we propose a Poincaré rotator to generate a beam with an arbitrary vortexed photons in an integrated optical circuit. We use Finite-Difference Time-Domain (FDTD) simulations for an Si micro-gear [29] evanescently coupled to two Si photonic wire waveguides (**Figure 1**). We discuss the impacts of the conservation law of OAM and spin as well as the geometrical Pancharatnam-Berry-Guoy's phase [26, 48, 73–76] for vortexed photons.

2. MODEL

2.1. Device Structure

The device structure is schematically shown in **Figure 1**. We assume the use of Si-On-Insulator (SOI) substrate with the top Si layer thickness t of 220 nm, on the buried-oxide (BOX) thickness of 2μm or beyond on top of the supporting Si substrate [70, 71]. Two standard straight wire waveguides are designed to be single mode with the width W of 440 nm. The polarization of the mode propagating in the Si wire waveguide is the quasi-Transverse-Electric (TE) mode [47, 48, 70], such that the electric field is dominated by the horizontal linearly polarized state with the momentum $p = \hbar k_{n_{\mathrm{eff}}}$, given by the wavenumber $k_{n_{\mathrm{eff}}} = 2\pi n_{\mathrm{eff}}/\lambda$ with the effective refractive index of n_{eff}.

The Si wire waveguides are located near the Si micro-gear (**Figures 1A,B,D,E**) with the distance d of 100nm. We have also considered a ring resonator (**Figure 1C**) for the reference. The width of both gears and a ring is the same width (W) with the waveguide. The radius R of gears and a ring is 1μm.

For the gear, we introduced the grating in the inner surface of the ring. The depth of the dip $dr = W/2$ is designed to be half of the waveguide width. We have calculated modes for gears with the grating number N of 10 (**Figure 1B**), 9 (**Figure 1D**), and 8 (**Figure 1E**), respectively, in order to see the impact of the grating to the conservation law. The wavelength we have considered in this work is fixed at $\lambda = 1,540$ nm, for which the grating of $N = 10$ satisfies the Bragg reflection condition.

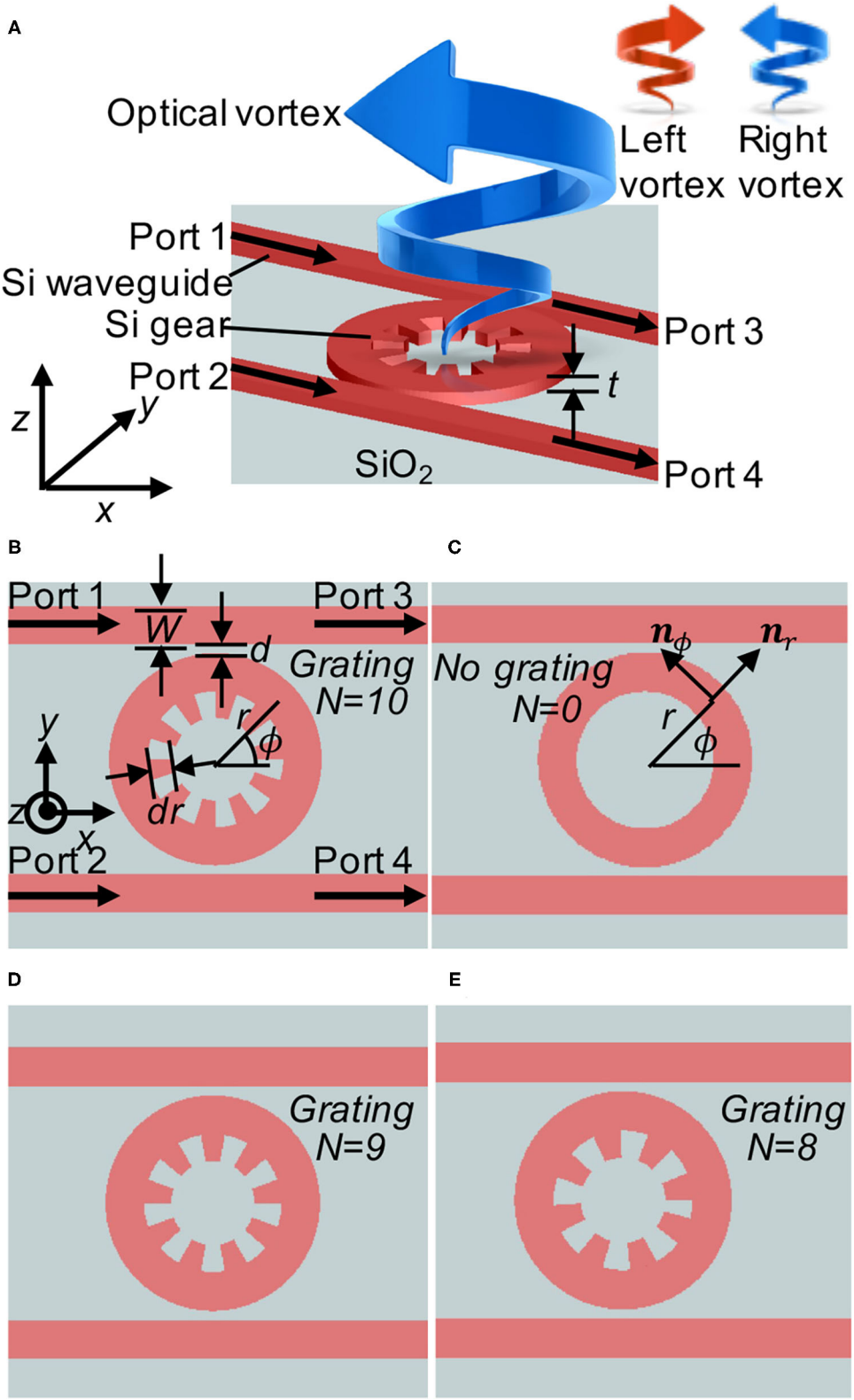

FIGURE 1 | Poincaré rotator. **(A)** Birds' view of the proposed device. The silicon (Si) micro-gear is coupled to two Si wire waveguides located on top of silicon dioxide (SiO_2). Two input ports (1 and 2) are used to inject photons with certain phases and amplitudes to generate a vortex beam with a superposition state of left and right vortexed states. The thickness of the Si layer is $t = 220$ nm. **(B)** Gear of the grating number N of 10. The width of waveguide is $W = 440$ nm. The depth of the grating dip is $dr = 220$ nm. The distance of between the gear and the waveguide is $d = 100$ nm. The radius of the grating is 1μm. **(C)** Ring resonator for the reference. Unit vectors of n_r and n_ϕ are shown. **(D)** Gears of $N = 9$. **(E)** Gears of $N = 8$.

Two input ports of 1 and 2 are used to inject photons from the waveguide into the gear. Photons from port 1 will couple to the gear to rotate along the right hand direction, seen from the top of the chip (from the $+z$ direction), while photons from port 2 will rotate the gear along the left hand direction. The idea is to control the phase and the amplitude of the input ports to generate the vortexed photons under a superposition state between left and right vortexed states.

One might think that one bus arrangement is enough to generate both left- and right- vortexed states, as demonstrated in previous works [29, 68]. In our case, however, we are considering to connect the waveguides to integrated Si photonic optical modulators [70, 71, 77] to allow the phase-shift for left- and right-vortices. Unfortunately, the coupling efficiency to a ring resonator from a waveguide is not high [70, 78, 79], and it is extremely sensitive to temperatures. Therefore, we must avoid interferences from the lights passing into the other ports. So far, on-chip isolators [80] are not integrated as an option for standard foundries of Si photonics chip, yet. A practical option at this moment was to employ two-bus arrangements [69, 81], such that the transmitted lights in the through-ports could be terminated to avoid the back reflections.

Here, we had better to explain our definition of the rotation. We use a standard right handed (x, y, z) coordinate as shown in **Figure 1**. (x, y) define the plane for the surface of the SOI substrate, and z is perpendicular to the substrate. We define the direction of rotation of photons, seen from the detector side. We believe this is a natural direction to describe the rotation, since we consider the rotation of the phase front in the (x, y) plane for a vortex, propagating along the $+z$ direction. Consequently, the phase front of the left vortex is rotating in the counter clock wise (left rotation), seen from the $+z$ direction, while the phase front of the right vortex is rotating in the clock wise (right rotation). We had better to clarify the way to describe the time evolution of the wave. We use $e^{i(kz-\omega t)}$ for the plane wave propagating along $+z$ direction over t with the wavenumber of k and the angular frequency of ω. Physicists prefer this definition, while engineers prefer $e^{-i(kz-\omega t)}$. Due to the duality for the definition of the imaginary number, $i^2 = (-i)^2 = 1$, both definitions work, properly. The use of a complex electric field is a useful technique to calculate an electro-magnetic field, and there is no issue to extract the observable real electric field by calculating the sum of the complex field and its complex conjugate at the end of the calculation [47, 48, 60]. But, the interpretation to consider the direction of the oscillation will be opposite in the complex fields of **E**, such that we needed to clarify to avoid unnecessary confusion. We are also aware that some physicists prefer to define the direction of rotation of photons, seen from the source side. This is in fact quite common, for example, to define the rotation of the screw driver or to consider the use of a handle to drive a car. However, as far as we use the left handed $\mathbf{x} = (x, y, z)$ coordinate, it is easier to show modes and phase angles in the (x, y) plane, such that the natural direction of the observation is from $+z$ direction, which is the detector side. We needed to emphasize this point, since our results would be complicated, if we are not sure about our definition. We apologize from the beginning for those who are not happy about our convention.

We also use the cylindrical coordinate $\mathbf{r} = (r, \phi, z)$, as shown in **Figure 1C**. The unit vectors along the radical and the azimuthal directions are $\mathbf{n}_r$ and $\mathbf{n}_\phi$, respectively. These unit vectors depend on the locations, $\mathbf{n}_r = \mathbf{n}_r(r, \phi) = (\cos\phi, \sin\phi, 0)$ and $\mathbf{n}_\phi = \mathbf{n}_\phi(r, \phi) = (-\sin\phi, \cos\phi, 0)$, such that we must take care of the difference of the fixed unit vectors to define the (x, y, z) coordinate. Even if the components of (r, ϕ) are constant over the area, the real vectors in (x, y) coordinate are changing over the space.

2.2. Ring: Momentum to Orbital Angular Momentum Converter

First, we have simulated a standard ring resonator [70, 82] (**Figure 1C**) to understand how OAM is generated. The single mode in the waveguide has no orbital angular momentum, and it is propagating with the momentum of $\mathbf{p} = (p_x, 0, 0)$ injected from the input port 1 (**Figure 2**). If we do not have the gear, **p** is conserved due to the translational symmetry of the wire waveguide along the x direction. This symmetry is broken due to the presence of the ring, and the modes in the waveguide and the ring are degenerate at the point of contact, where the resonance to the ring waveguide is taking place [70, 82], and the fraction of photons are transferred from the waveguide to the ring resonator.

The single mode of the input is oscillating predominantly along y direction, since it is a TE mode, given by $\mathbf{E} = (E_x, E_y) \approx (0, E_y)$. We use the arbitrary units throughout this paper, and the input mode is normalized as

$$\int dy\, |E_y|^2 = 1. \tag{3}$$

In order to see how the direction of oscillation has been changed, we have projected $\mathbf{E} = (E_x, E_y)$ to the azimuthal and the radical directions to get each component as

$$E_\phi = \mathbf{E} \cdot \mathbf{n}_\phi = -E_x \sin\phi + E_y \cos\phi \tag{4}$$

$$E_r = \mathbf{E} \cdot \mathbf{n}_r = E_x \cos\phi + E_y \sin\phi, \tag{5}$$

respectively. As shown in **Figure 2**, the mode in the ring resonator is predominantly oscillating in the radical direction (**Figures 2E,F**), such that the direction of the oscillation is perpendicular to the direction of the propagation. This is consistent with the single TE mode nature of the ring resonator. Nevertheless, some interesting features are already going on, since the unit vector $\mathbf{n}_r$ is changing the direction along the circulation. Therefore, the polarization is changing azimuthally from horizontal, diagonal, vertical, vertical, back to horizontal upon the rotation. In other words, the average spin angular momentum becomes zero for the resonant mode, circulating in the ring resonator, because of the change in the direction of oscillation upon the time evolution. On the other hand, OAM becomes non-zero, since the mode acquired the phase as

$$E_r \propto e^{im\phi}, \tag{6}$$

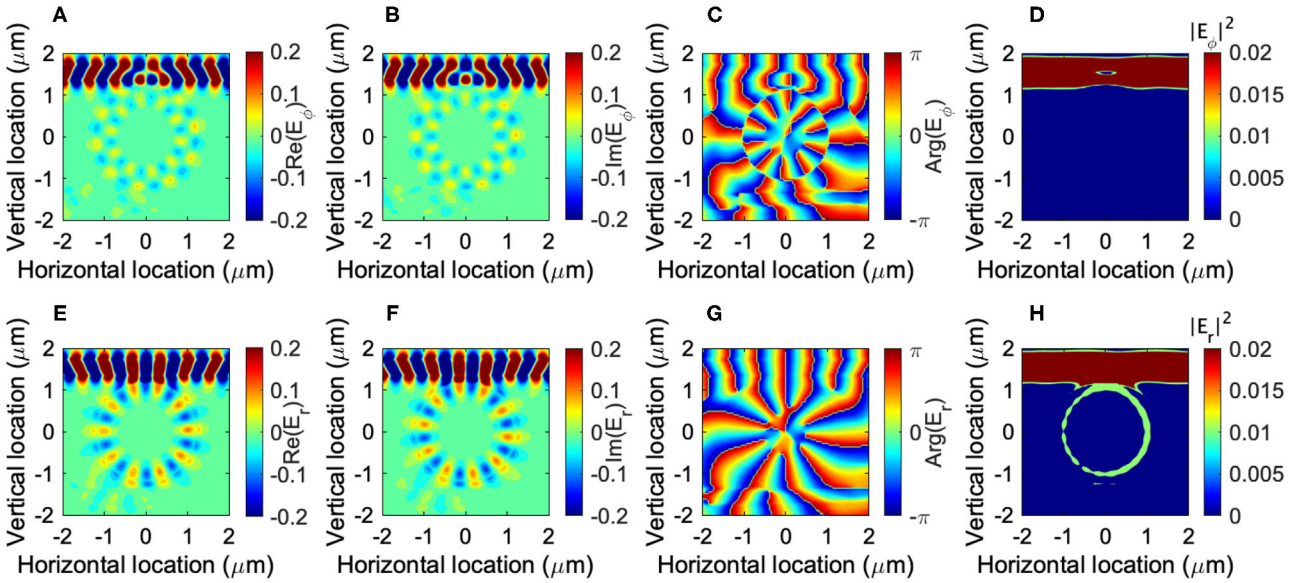

FIGURE 2 | Ring resonator coupled to a wire waveguide. **(A)** Real and **(B)** imaginary part of the azimuthal component of the electric field, its **(C)** phase, and **(D)** intensity. **(E)** Real and **(F)** imaginary part of the radial component of the electric field, its **(G)** phase, and **(H)** intensity. The orbital angular momentum of $m = -10$ is obtained for a ring of the radius of 1μm at the wavelength of 1,540 nm. The mode is rotating along the clock-wise (right) direction.

where the m is the OAM component along the quantization axis of z. We confirm that it is the eignemode of the OAM operator

$$\hat{L}_z E_r = \frac{\hbar}{i}\frac{\partial}{\partial\phi}E_r = \hbar m E_r. \tag{7}$$

In our example of **Figure 2**, the input mode from the port 1 is coupled to the resonator mode of $m = -10$ and it is rotating along the clock-wise right direction, as is evident from the phase evolution from blue (the phase of $-\pi$), green, to red (the phase of π) toward the right circulation (**Figures 2C,D**). This corresponds to the right circulation over the time evolution. Due to the rotational symmetry of the ring, OAM is preserved, if it is isolated. In reality, the ring resonator is coupled to wire waveguides, such that the loss is expected to loose some fractions of photons leaking from the resonator. We also confirmed that E_ϕ also has the same phase and OAM of $m = -10$.

In this classical example, we see that the momentum of photons in the waveguide is transferred to OAM in the ring resonator. Therefore, the ring resonator works as a converter of momentum to OAM. Due to the broken symmetry of the system, the momentum is not conserved, and it adiabatically changes the direction of the propagation. In the ring, it is circulating in the right direction, such that the mode acquired OAM.

It is also interesting to be aware that the Bohr-Sommerfeld quantization condition [3, 4, 8, 9],

$$\oint_C p_\phi \cdot R d\phi = hm, \tag{8}$$

is certainly satisfied to obtain the azimuthal component of the momentum

$$p_\phi = h\frac{m}{2\pi R} = \frac{h}{\lambda_{n_{\text{eff}}}} \tag{9}$$

and the effective wavelength in the waveguide

$$\lambda_{n_{\text{eff}}} = \frac{2\pi R}{m}. \tag{10}$$

It is also important to have a node at the center of the ring. In the ring waveguide, the amplitude of the mode vanishes at the center due to the absence of the material of a high refractive index, and therefore it is obvious. Even if we use a disk instead of the ring, the Whispering-Gallery-Mode (WGM) [67] has a node at the center. Otherwise, OAM would diverge at the center [19]. Thus, the finite m is also called as topological charge, since it characterizes the nature of the electric fields surrounding it. We had better to emphasize, though, that there is no physical observable in the unit of charge. There is no singularity of the fields, either. It is just a node, and m is the winding number of the phase to characterize the vortex, and m is the quantization integer for the OAM component along the direction of the propagation.

2.3. Gear: Generator of Vortices and Conservation Law for Optical Angular Momentum

Next, we discuss about the generation of vortices out of the gear, coupled to the Si wire waveguide [29, 68, 69]. Our design is much smaller than the original proposal of Cai et al. [29], and we found an interplay between spin and OAM upon the conservation law.

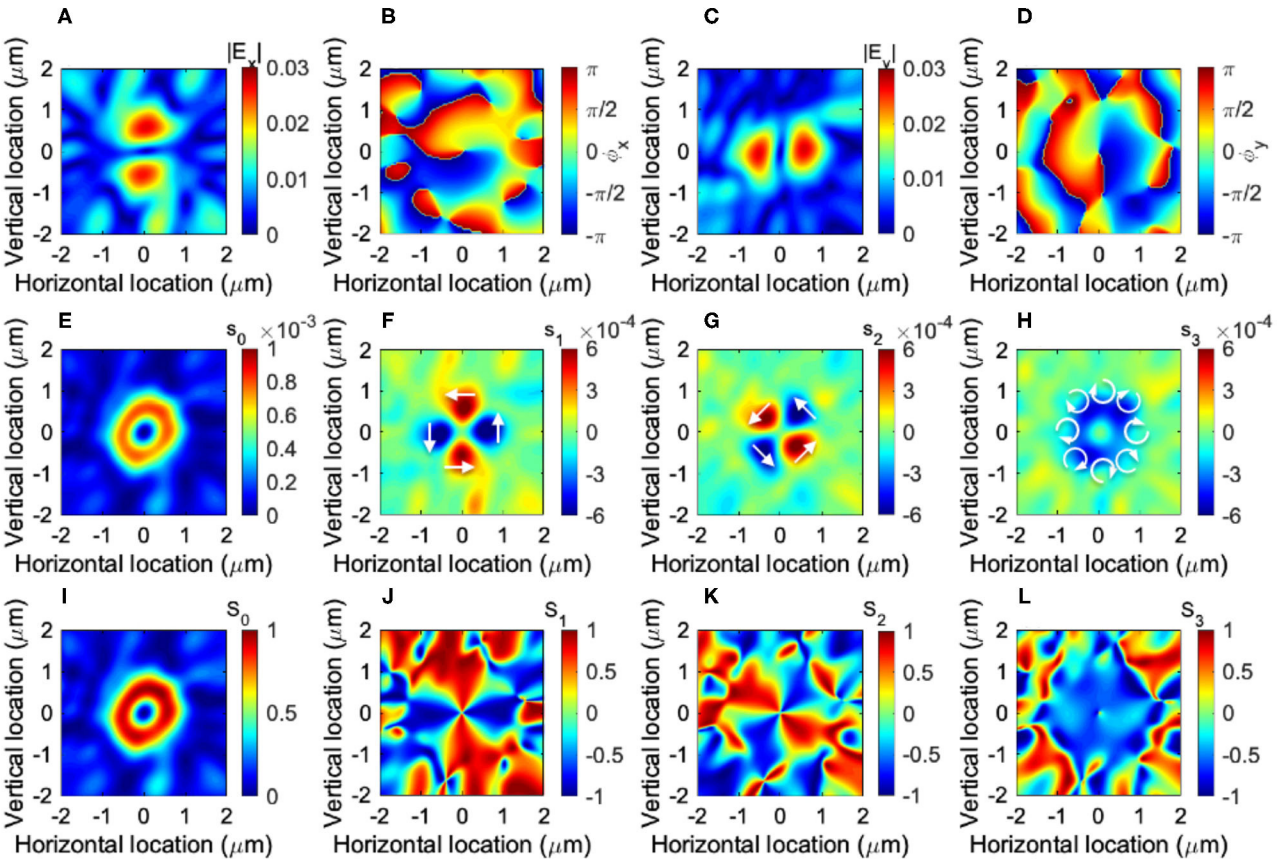

FIGURE 3 | Left vortex generated from the gear of $N = 10$. The input port 1 is used to inject photons to the waveguide, and the mode profile is obtained at $z = 1\mu$m above the gear. **(A)** The amplitude ($|E_x|$) and **(B)** the phase (ϕ_x) of the horizontal electric field E_x. **(C)** The amplitude ($|E_x|$) and **(D)** the phase (ϕ_y)of the horizontal electric field E_y. They show $E_y \sim -iE_x \propto e^{i\phi}$, showing the direct tensor product state of the right-circularly-polarized state and the left-vortexed state, $|\circlearrowleft\rangle_{\text{spin}} \otimes |\circlearrowleft\rangle_{\text{orbit}}$. **(E)** The local intensity, s_0, **(F)** local horizontal/vertical spin component, s_1, **(G)** local diagonal/anti-diagonal spin component, s_2, and **(H)** local left/right spin component, s_1. Normalized Stokes parameters of **(I)** S_0, **(J)** S_1, **(K)** S_2, and **(L)** S_3. White arrows in **(F–H)** schematically show the direction of oscillations.

In the design of Cai et al. [29], the depth of the grating is not significant, such that the small azimuthal component of E_ϕ was scattered by the grating. On the other hand, the width of our grating is the half of the width of the waveguide, $dr = W/2$, (**Figure 1B**) and strong scattering of the entire mode is expected in our design.

First, we have simulated for the gear of $N = 10$ (**Figure 1B**). In this design, the Bragg reflection condition is satisfied, such that the grating will give the momentum of $\hbar 2\pi/\Lambda$, where $\Lambda = 2\pi R/N \sim 628$nm is the period of the grating, and we expect

$$p_\phi - \hbar\frac{2\pi}{\Lambda} \approx 0 \tag{11}$$

due to the momentum conservation law in a periodic system [48, 83–85]. Using the effective refractive index of the grating as the average value of Si and SiO_2 as $n_{\text{eff}} = (3.48 + 1.44)/2 = 2.46$, we obtain $\lambda_{n_{\text{eff}}} \sim 626$ nm, and thus $\lambda_{n_{\text{eff}}} \sim \Lambda$. Therefore, the momentum of photons in the plane vanishes upon acquiring the Bragg momentum, and photons will be projected out of the gear.

The amplitudes and phases of the mode simulated at $z = 1\mu m$ above the gear is shown in **Figure 2**. To our surprise, OAM was not zero, and both E_x and E_y showed the clear anti-clock-wise (left) circulation (**Figures 3A–D**) with the OAM quantum number of $m' = +1$, where we used $'$ to stand for the quantum number after the scattering. This corresponds to the left circulation of a vortex over the time evolution. We have numerically confirmed that OAM of the left-vortexed state (**Figures 3B,D**) is

$$m = \oint_C \frac{d\phi}{2\pi}\nabla\phi_x = \oint_C \frac{d\phi}{2\pi}\nabla\phi_y = 1, \tag{12}$$

which means that the winding number gives the expected z component of OAM.

The amplitudes of $|E_x|$ and $|E_y|$ show the presence of a node at the center of vortex. Moreover, if we compare the phase ϕ_x of E_x with the phase ϕ_y of E_y, it shows $\phi_y = \phi_x - \pi/2$, which means that spin $s' = -1$, showing the right-circularly-polarized state. Consequently, our numerical simulation shows the left vortexed

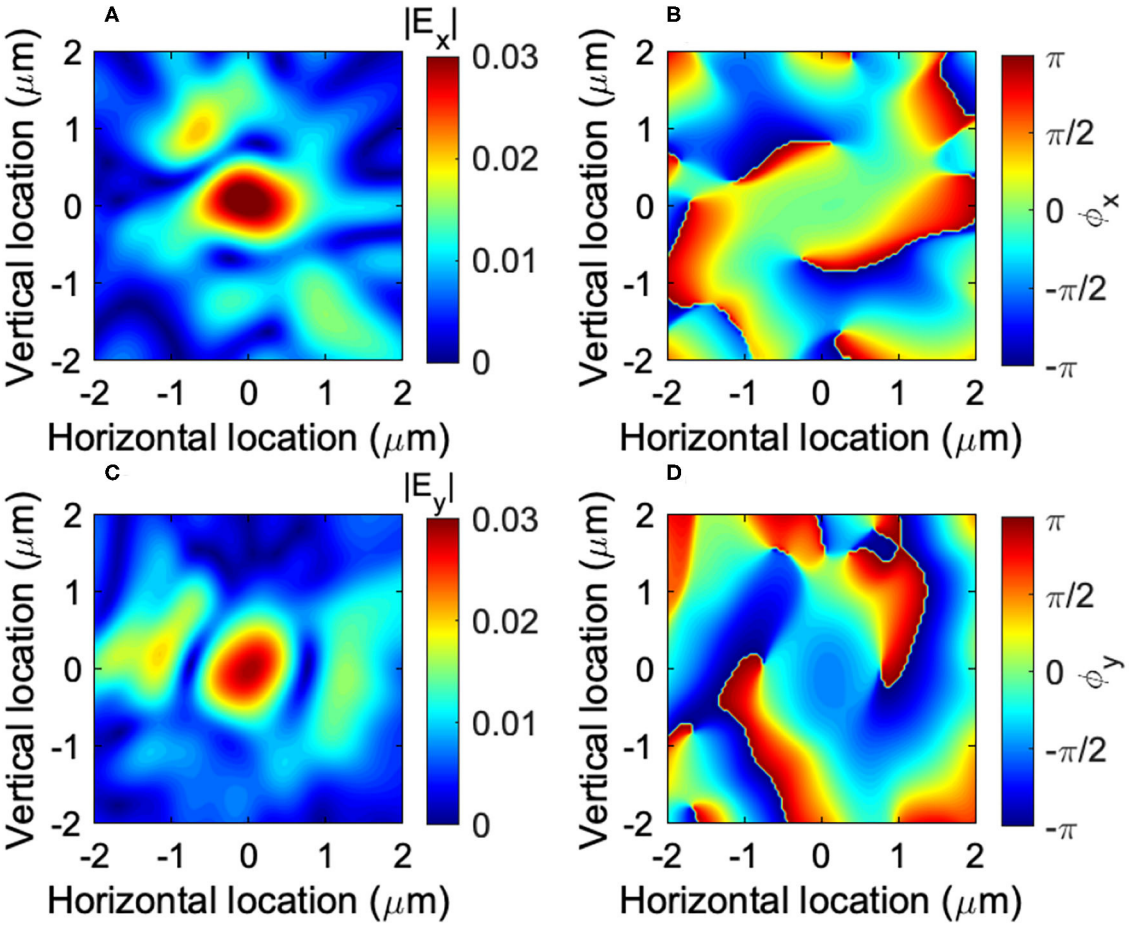

FIGURE 4 | Right-circularly-polarized state, generated from the gear of $N = 9$. The input port 1 is used to inject photons to the waveguide, and the mode profile is obtained at $z = 1\mu$m above the gear. **(A)** The amplitude ($|E_x|$) and **(B)** the phase (ϕ_x) of the horizontal electric field E_x. **(C)** The amplitude ($|E_x|$) and **(D)** the phase (ϕ_y)of the horizontal electric field E_y. There is no node in the modes, such that there is no OAM. They show $E_y \sim -iE_x$, such that the polarization is right-circularly-polarized state, $|\circlearrowleft\rangle_{\text{spin}}$.

state, given by the extended Jones vector [48, 52, 55–57, 60]

$$|\mathrm{L}\rangle = \frac{\mathrm{e}^{-i\frac{\pi}{4}}}{\sqrt{2}}\begin{pmatrix}1\\-i\end{pmatrix}\mathrm{e}^{i\phi}, \tag{13}$$

where the first component is proportional to E_x and the second component is proportional to E_y. The polarization state is described by the $SU(2)$ state [5–7, 10, 11]. Here, we have omitted to include the radial dependence, given by the Laguerre-Gauss function or the Hermite-Gauss function [19, 48]. The global phase factor of $\mathrm{e}^{-i\frac{\pi}{4}}$ is not necessary but useful to understand the azimuthal component. The global phase also depends on the $U(1)$ wave from $\mathrm{e}^{-i(kz-\omega t)}$, standing for the propagation along z and t, and the choice of the phase of $\mathrm{e}^{-i\frac{\pi}{4}}$ is just coming from our random choice of the detector position at $z = 1\mu$m. The important point of our left-vortexed state $|\mathrm{L}\rangle$ is based on the fact that it is a direct tensor product state of spin and OAM with opposite rotation. Therefore, it can also be described as

$$|\mathrm{L}\rangle = |\circlearrowleft\rangle_{\text{spin}} \otimes |\circlearrowleft\rangle_{\text{orbit}}. \tag{14}$$

We described this state as left-vortexed state, since we are primarily interested in a vortex for the present work.

Consequently, the conservation law of angular momentum is described as

$$s + m + N = s' + m', \tag{15}$$

where $s = 0$, $m = -10$, $N = 10$, $s' = -1$, and $m' = 1$. Therefore, both spin and OAM are involved upon the scattering from our grating gear to produce a vortex, while the total angular momentum along the direction of propagation is zero due to the opposite rotation by spin.

The importance of the conservation law of spin and OAM of photons in a micro-gear was first discussed by Shao et al. [68], where the local spin components were experimentally measured

and spin-orbit interaction was demonstrated. They used the gear with $R = 80\mu$m, and the conservation law of angular momentum at the local edge of the grating was discussed [68]. Our design is based on $R = 1\mu$m, and the entire mode profile affects the conservation law of angular momentum. Following the analysis [68], we have also calculated the local spin density of photons, $\mathbf{s} = (s_1, s_2, s_3)$, defined by

$$s_1 = \mathbf{E}^\dagger \hat{\sigma}_3 \mathbf{E} = \begin{pmatrix} E_x^* & E_y^* \end{pmatrix} \begin{pmatrix} 1 & 0 \\ 0 & -1 \end{pmatrix} \begin{pmatrix} E_x \\ E_y \end{pmatrix} = |E_x|^2 - |E_y|^2 \quad (16)$$

$$s_2 = \mathbf{E}^\dagger \hat{\sigma}_1 \mathbf{E} = \begin{pmatrix} E_x^* & E_y^* \end{pmatrix} \begin{pmatrix} 0 & 1 \\ 1 & 0 \end{pmatrix} \begin{pmatrix} E_x \\ E_y \end{pmatrix} = E_x^* E_y - E_y^* E_x \quad (17)$$

$$s_3 = \mathbf{E}^\dagger \hat{\sigma}_2 \mathbf{E} = \begin{pmatrix} E_x^* & E_y^* \end{pmatrix} \begin{pmatrix} 0 & -i \\ i & 0 \end{pmatrix} \begin{pmatrix} E_x \\ E_y \end{pmatrix} = -iE_x^* E_y + iE_y^* E_x, \quad (18)$$

which satisfy $s_0 = \sqrt{s_1^2 + s_2^2 + s_3^2} = |E_x|^2 + |E_y|^2$ (**Figure 3E**). We have also calculated the local Stokes parameters, given by

$$S_1 = S_1(\mathbf{x}) = \frac{s_1}{s_0} \quad (19)$$

$$S_2 = S_3(\mathbf{x}) = \frac{s_2}{s_0} \quad (20)$$

$$S_3 = S_2(\mathbf{x}) = \frac{s_3}{s_0}, \quad (21)$$

which is normalized as $\sqrt{S_1^2 + S_2^2 + S_3^2} = 1$ at each point $\mathbf{x}$, while $S_0 = S_0(\mathbf{x})$ (**Figure 3I**) is a normalized s_0 with its maximum value. As shown in **Figures 3H,L**, the local density of the right-circularly polarized state (s_3 and S_3) is distributed over the ring, which describes the opposite rotation of the polarization to the rotation of the left-vortex state, described by the left rotation of the phases (**Figures 3B,D**). We also found components of locally linearly-polarized states (s_1 and s_2), which are changing signs depending on the positions (**Figures 3F,G,J,K**) and described by

$$|\text{local spin}\rangle = E_{\text{spin}} \begin{pmatrix} -\sin(\phi) \\ \cos(\phi) \end{pmatrix}. \quad (22)$$

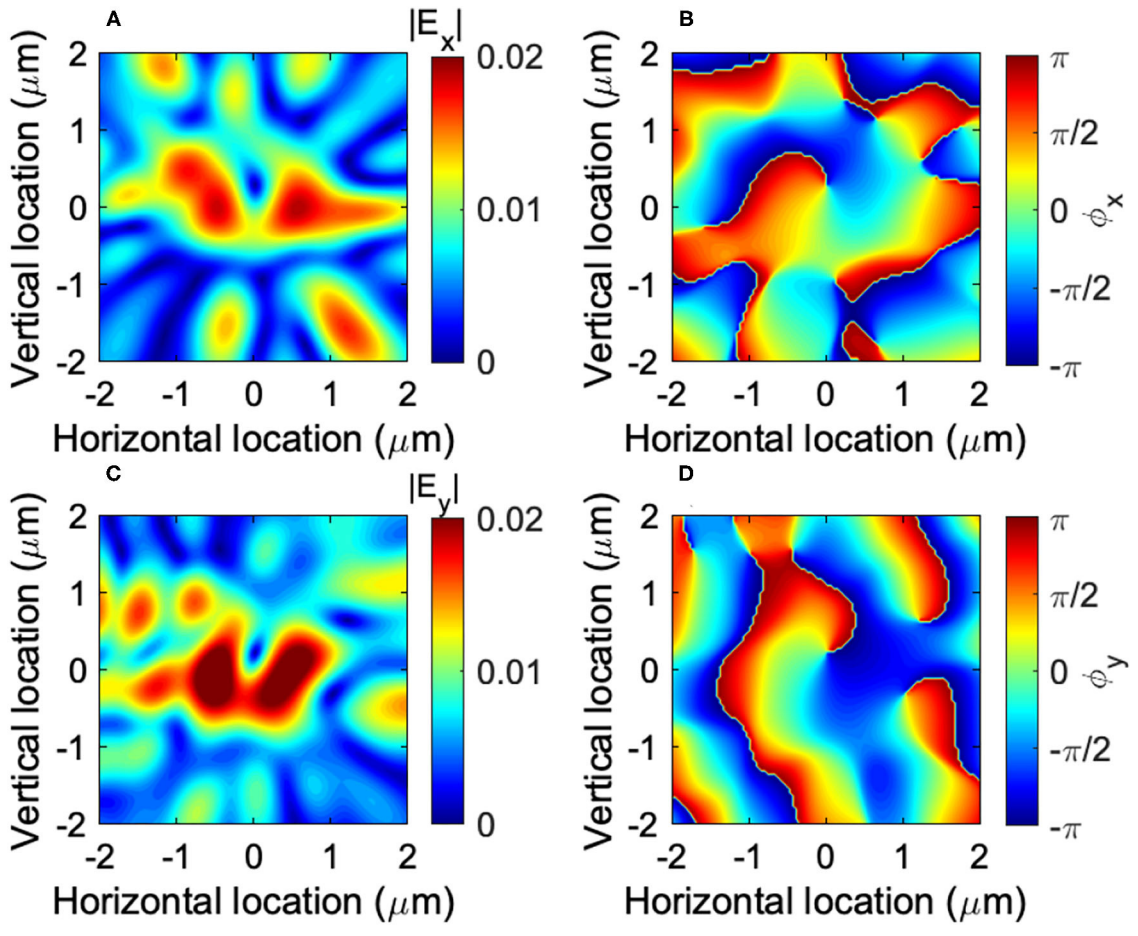

FIGURE 5 | Right vortex generated from the gear of $N = 8$. The input port 1 is used to inject photons to the waveguide, and the mode profile is obtained at $z = 1\mu$m above the gear. **(A)** The amplitude ($|E_x|$) and **(B)** the phase (ϕ_x) of the horizontal electric field E_x. **(C)** The amplitude ($|E_x|$) and **(D)** the phase (ϕ_y)of the horizontal electric field E_y. They show $E_y \sim -iE_x \propto e^{-i\phi}$, showing the direct tensor product state of the right-circularly-polarized state and the right-vortexed state, $|\circlearrowright\rangle_{\text{spin}} \otimes |\circlearrowright\rangle_{\text{orbit}}$.

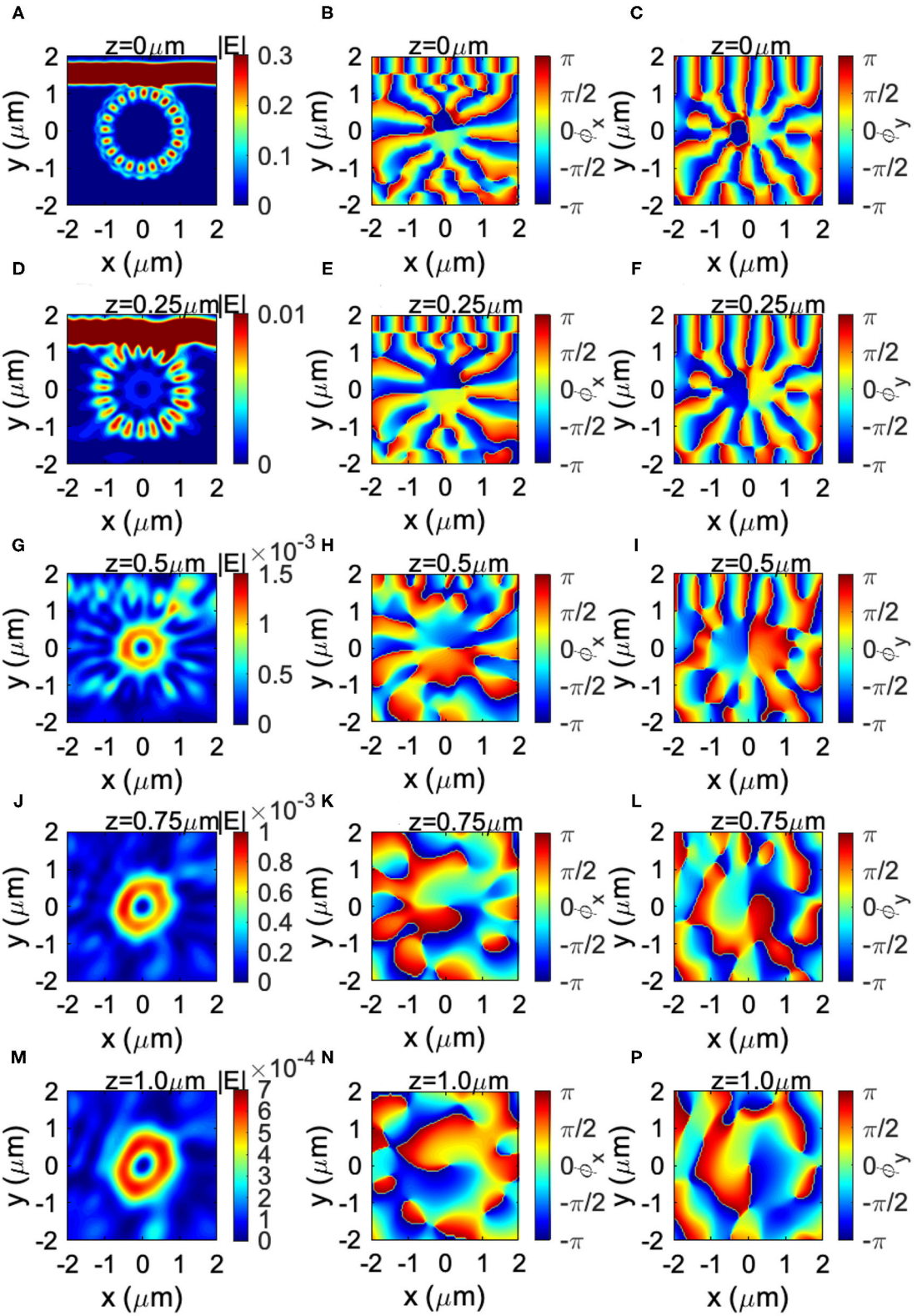

FIGURE 6 | Generation of left vortex from the gear of $N = 10$. The input port 1 is used to inject photons to the waveguide. The mode profiles are obtained at $z = 0, 0.25, 0.5, 0.75$, and 1μm above the gear, which are shown in **(A–C)**, **(D–F)**, **(G–I)**, **(J–L)**, and **(M–P)**, respectively. The amplitude $|E|^2 = |E_x|^2 + |E_y|^2$ and the phases $\phi_x = \arg(E_x)$ and $\phi_y = \arg(E_y)$ are shown in **(A,D,G,J,M)**, **(B,E,H,K,N)**, and **(C,F,I,L,P)**, respectively.

However, the overall contribution of this component to the total spin vanishes after the spatial integration, since both negative and positive values appeared equally (**Figures 3F,G,J,K**). Moreover, the contribution of this component to OAM also vanishes, which is confirmed by calculating

$$\oint_C d\phi \langle \text{local spin}|\hat{L}_z|\text{local spin}\rangle = \oint_C d\phi \left(-\sin(\phi)\ \cos(\phi)\right) \frac{\hbar}{i}\frac{\partial}{\partial\phi}\begin{pmatrix}-\sin(\phi)\\ \cos(\phi)\end{pmatrix} = 0. \quad (23)$$

It is interesting to be aware that the local spin component is also circulating along the azimuthal direction (schematically shown as arrows in **Figures 3F,G**), due to the rotation of the phases (**Figures 3B,D**). Numerically, we have obtained the spatial averages of Stokes parameters, $\bar{\mathbf{S}} = (\bar{S}_1, \bar{S}_2, \bar{S}_3) = (-0.01, +0.01, -0.52)$ for the left-vortexed state. The spatial average of the OAM, $\bar{m}$, was 0.53. The reduction of the expected OAM of 1 from the left vortex is attributed to the contribution of the local spin component with vanishing OAM. This means that about 50% of the mode is made of the purely left-vortexed state under right polarization, while another 50% of the mode is made of the local spin components, which are characterized by spatially rotating linear polarization. Therefore, the efficiency to generate the left vortex out of our gear is about 50%.

In order to confirm our picture on the conservation law of angular momentum, we have also simulated for the gear of $N = 9$ (**Figures 1D**, **4**). In this case, the node completely disappeared from the mode (**Figures 2A,C**), such that OAM cannot be sustained and we obtained $m' = 0$ (**Figure 4**). On the other hand, we confirmed the same phase difference at the center of the mode as before $\phi_y = \phi_x - \pi/2$. Therefore, the state is simply described by a polarization state

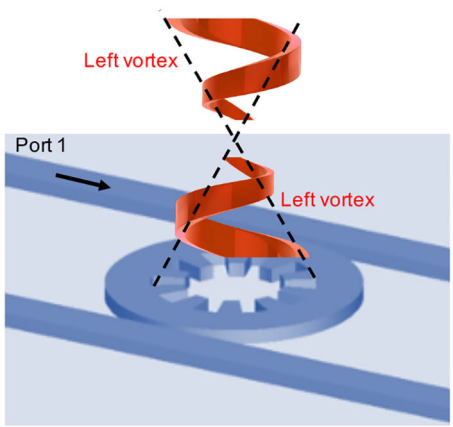

FIGURE 7 | Pancharatnam-Berry-Gouy phase for a vortex generated from the gear. The contribution from the polarization would change the sign of the complex electric field, and the orbital angular momentum will also add to the phase change upon crossing of the focal point. The chirality of a vortex would not be changed upon focusing.

$$|\circlearrowleft\rangle_{\text{spin}} = \frac{e^{-i\frac{\pi}{4}}}{\sqrt{2}}\begin{pmatrix}1\\ -i\end{pmatrix}, \quad (24)$$

which is the right-circulary-polarized state without a vortex. The nodeless mode profile was not reported in the previous work [29], such that our results are coming from the difference of the design of the gear. In our example, the conservation law for angular momentum is given by

$$s + m + N = s' + m', \quad (25)$$

where $s = 0$, $m = -10$, $N = 9$, $s' = -1$, and $m' = 0$. Therefore, the difference between $N = 10$ and $N = 9$ is exactly what we expected.

Furthermore, we have continued to simulate the structure of the gear with $N = 8$ (**Figure 1E**). In this case, the grating is far away from the perfect Bragg grating condition, such that the mode profiles are significantly distorted (**Figures 5A,C**). Nevertheless, they showed the presence of the node at the center (**Figures 5A,C**), and the phase is rotating along the clock-wise (right) direction (**Figures 5B,D**), which is completely opposite to the result for $N = 10$, as we expected from the conservation law. In this case, the vortexed state is described as

$$|\circlearrowleft\rangle_{\text{spin}} \otimes |\circlearrowleft\rangle_{\text{orbit}} = \frac{e^{-i\frac{\pi}{4}}}{\sqrt{2}}\begin{pmatrix}1\\ -i\end{pmatrix} e^{-i\phi} \quad (26)$$

The conservation law for angular momentum is given by

$$s + m + N = s' + m', \quad (27)$$

where $s = 0$, $m = -10$, $N = 8$, $s' = -1$, and $m' = -1$.

In all cases, the angular momentum is conserved upon scattering by gratings. It is important to consider both spin and OAM, simultaneously, to understand the conservation law. On the other hand, we cannot understand why $s' = -1$ was always chosen for $N = 10$, 9, and 8, simply from the conservation law of angular momentum. This could be understood by the evolution of the phase front, as shown in **Figure 6**. The original input is TE polarized along y direction, such that the phase front of ϕ_y is going ahead of ϕ_x, and E_x acquires the same amplitude with that of E_y at the intersection only after the quarterly rotation (phases inside the ring of **Figures 6B,C**). As a result, we obtain $\phi_y = \phi_x - \pi/2$, if we compare the phases at the same position, leading to the generation of the vortex with right polarization (**Figures 6N,P**). Thus, the spin angular momentum is fixed, while OAM is determined by the conservation law of angular momentum.

2.4. Pancharatnam-Berry-Guoy's Phase

We have also considered the Pancharatnam-Berry-Guoy's phase on the generation of a vortex from the gear [26, 48, 73–76]. We considered the design of $N = 10$ (**Figure 1B**) and examined the evolution of mode profiles over the propagation along the $+z$ direction (**Figure 6**). The input beam was injected from port 1, and it coupled evanescently to the gear. At the center of the waveguide at $z = 0$, the mode is circulating in the ring waveguide with OAM of $m = -10$. The phases of $\phi_x = \arg(E_x)$ and

$\phi_y = \arg(E_y)$ show the right circulation over time. If we closely look at ϕ_x and ϕ_y inside the ring, there is no phase difference between them ($\phi_x \sim \phi_y$), consistent with the dominated radical polarization (**Figures 2E,F**) and thus we confirm $s = 0$. The beam is diffracted by the Bragg condition by the grating of the gear, and the mode was emitted vertically from the surface of the device. The direction of propagation is vertical but is slightly pointing inside the gear, since the grating is located only inside of the ring resonator. Consequently, the emitted beam is focused at around $z = 0.5\mu$m (**Figure 6G**), and defocused again (**Figures 6H,M**). It is important to recognize the presence of a node even at the focussed point (**Figure 6G**) to maintain the vortex. We can recognize that the mode gradually changed its shape to accommodate the left circulation with OAM of $m' = +1$, which is opposite rotation with the circulation of $m = -10$ in the ring. We also confirmed that $\phi_y = \phi_x - \pi/2$ for a vortex at $z \geq 0.5\mu$m, such that it is in the right-circularly polarized state.

We could also confirm the spatial rotation of ϕ_x and ϕ_y over z (**Figures 6K,N,L,P**), expected from $e^{i(kz-\omega t)}$. The phase front evolution of z is opposite to t, such that the chiral rotation of the phase of the vortex over the space is opposite to the time evolution. The phase front has moved to the clock-wise (right) direction from **Figures 6K,L** to **Figures 6N,P**, respectively. This is in fact opposite to the left circulation of the vortex, and therefore, our interpretation of OAM and polarization of a vortex is consistent.

The schematic nature of the evolution of a vortex is shown in **Figure 7**. The chirality of the vortex cannot be changed upon the focussing, and the left circulation of the vortex is maintained. On the other hand, we had better to be careful about the geometrical phase facto of Pancharatnam-Berry-Gouy phase [19, 26, 73–76, 86], which is given by

$$\phi_G = (2n + |m| + 1)\tan^{-1}\left(\frac{z}{z_0}\right), \tag{28}$$

where n is the radial quantum number of the Laguerre-Gauss mode, and z_0 is the location of the focussing point [19, 48]. In the example of **Figure 6**, there is no node in the radial direction, except for the central core, and we can assign $n = 0$. In the

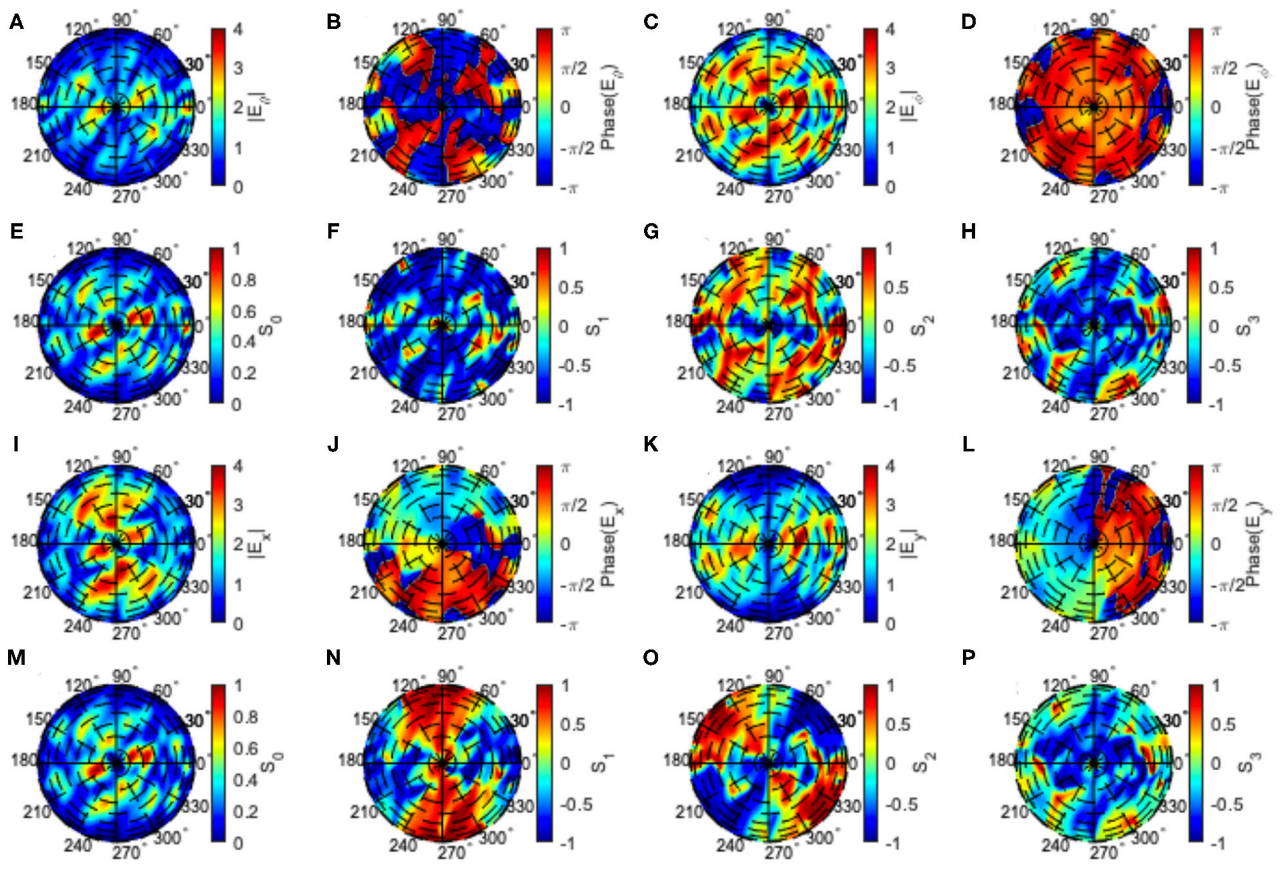

FIGURE 8 | Far-fields and Stokes parameters of left vortex from the gear of $N = 10$. The input port 1 is used to inject photons to the waveguide. Far-fields and Stokes parameters are shown **(A–H)** in a polar coordinate (r, θ, ϕ) and **(I–P)** in a cylindrical coordinate (r, ϕ, z). The ring-shape of the mode in the near-field could not be sustained in far-fields **(A,C,E,I)**, because our mode is not collimated. Consequently, the vortex is not well-defined in far-fields, while the phase is still rotated over the hemisphere **(J,L)**, reflecting the original nature of a left-vortexed state. The polarization is also dominated by the right-circularly polarized component **(H,P)** with $S_3 \sim -1$ for the high intensity region.

absence of OAM ($m = 0$), ϕ_G would result in the phase change of the complex electric field, $(E_x, E_y) \rightarrow -(E_x, E_y)$. In our case, $m' = -1$ will give another factor of -1, and therefore, we expect no change of the sign upon focussing for the far field ($z \rightarrow \infty$).

For the vortex beam with the higher order OAM, the Pancharatnam-Berry-Gouy phase factor depends on the parity of m. If $|m|$ is odd, the contribution would vanish together with the contribution from the polarization, as we saw for $m' = -1$. If $|m|$ is even including $m = 0$, the phase change is expected upon crossing over the focal point. Therefore, the parity dependent interference is expected for a vortex, generated from the gear.

2.5. Far-Fields

We have also calculated far-fields and Stokes parameters in a polar coordinate (r, θ, ϕ) and in a cylindrical coordinate (r, ϕ, z), as shown in **Figure 8**. In a polar coordinate, the polar (E_ϕ) and the azimuthal (E_ϕ) components are obtained (**Figures 8A–D**). In particular, the phase of E_ϕ is constant over the hemisphere (**Figure 8D**), showing the electric field is rotating with a fixed phase along the azimuthal direction. As noted before, the unit vector of azimuthal component depends on ϕ, ($\mathbf{n}_\phi = \mathbf{n}_\phi(r, \phi) = (-\sin\phi, \cos\phi, 0)$), such that the fixed phase means the vectorial direction of azimuthal component is also changing the direction along the rotation.

As shown in **Figures 6**, **7**, our near-field mode profile is not collimated at all. Therefore, the vortex and associated OAM are not maintained in far-fields (**Figures 8E,I,K**), and the mode is spreading over the hemisphere. The intensity profiles are spreading over the polar angle of 10 to 40°. Nevertheless, the original nature of rotated phase is sustained, as shown in the rotated phases of ϕ_x (**Figure 8J**) and ϕ_y (**Figure 8L**), reflecting the left-vortexed nature in the near-field. The polarization of the mode is also reflecting the original mode in the near-field, and the right polarized component of $S_3 \sim -1$ (**Figures 8H,P**) is dominated at the region of high intensities.

3. POINCARÉ ROTATOR

In this section, we discuss about our main results for the proposed Poincaré rotator (**Figure 1A**). As shown in the previous section, we could generate the left-vortexed state $|\mathrm{L}\rangle$ by injecting photons from the port 1 of the Si wire waveguide. Due to the mirror symmetry between the port 1 and the port 2 together with the gear, we can generate the right-vortexed state $|\mathrm{R}\rangle$, which is completely opposite chiral rotation to the left-vortex, by injecting photons from the port 2. The idea, here, is to inject from both ports after adjusting the relative amplitudes and phases of the injected beams, to generate an arbitrary vortexed state

$$|\Theta, \Phi\rangle = \mathrm{e}^{-i\frac{\Phi}{2}} \cos\left(\frac{\Theta}{2}\right)|\mathrm{L}\rangle + \mathrm{e}^{i\frac{\Phi}{2}} \sin\left(\frac{\Theta}{2}\right)|\mathrm{R}\rangle \qquad (29)$$

in the hyper-Poincaré sphere. In modern Si photonic technologies, it is easy to control both amplitudes and phases by

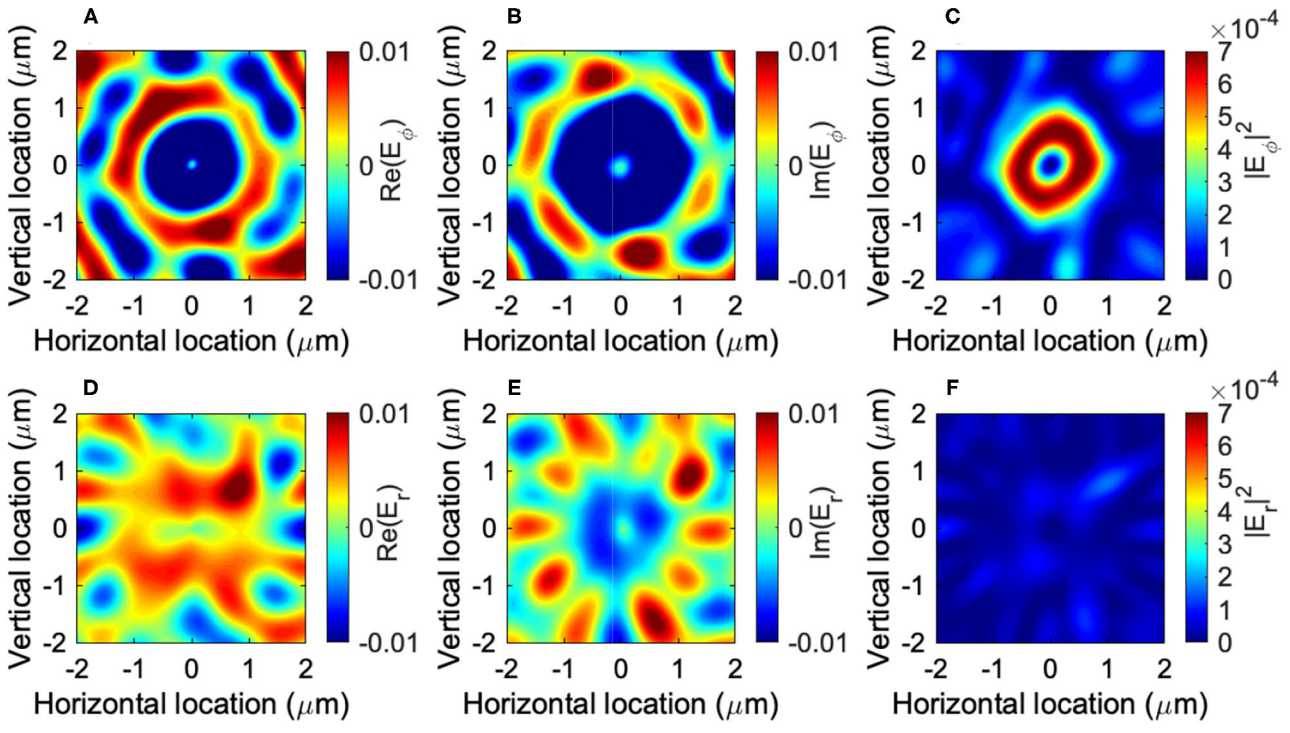

FIGURE 9 | Left vortex generated from the gear of $N = 10$. The input port 1 is used to inject photons to the waveguide, and the mode profile is obtained at $z = 1\mu$m above the gear. **(A)** Real part, **(B)** imaginary part, and **(C)** intensity of the azimuthal complex electric field (E_ϕ). **(D)** Real part, **(E)** imaginary part, and **(F)** intensity of the radial complex electric field (E_r). E_ϕ is almost constant over the ring, such that the mode is dominated by the azimuthal component.

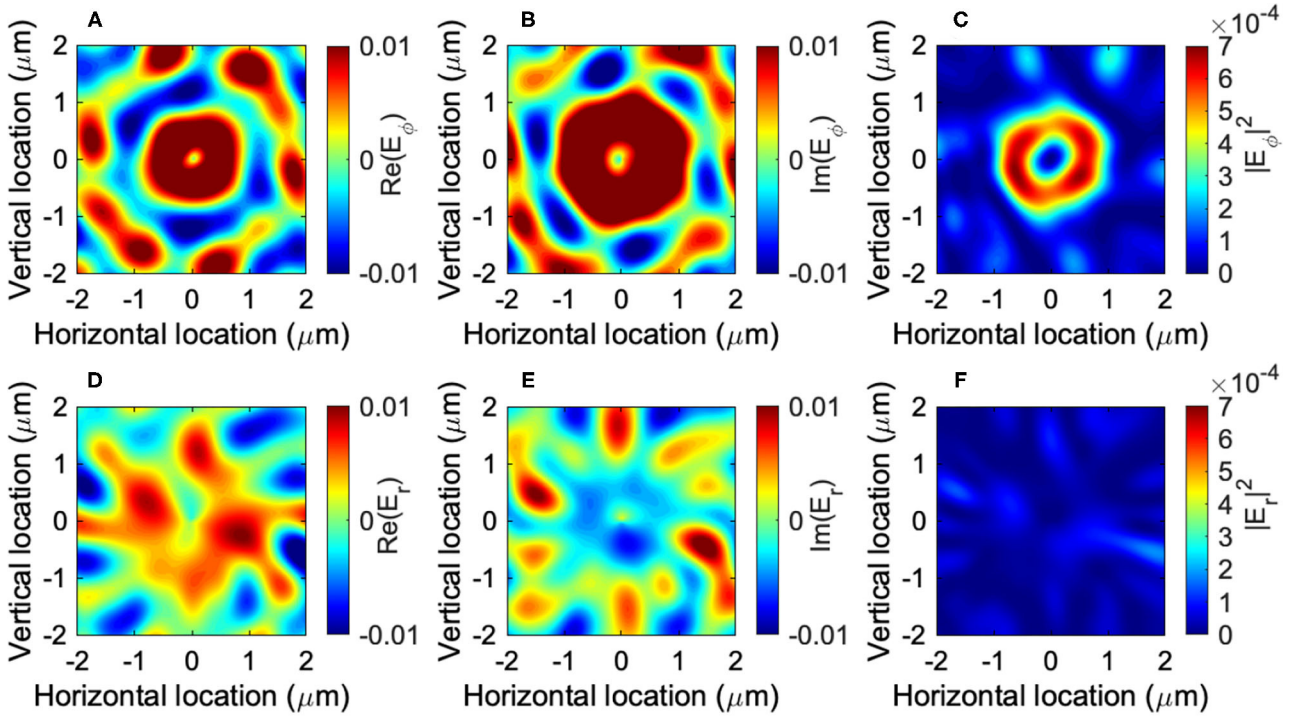

FIGURE 10 | Right vortex generated from the gear of $N = 10$. The input port 2 is used to inject photons to the waveguide, and the mode profile is obtained at $z = 1\mu$m above the gear. **(A)** Real part, **(B)** imaginary part, and **(C)** intensity of the azimuthal complex electric field (E_ϕ). **(D)** Real part, **(E)** imaginary part, and **(F)** intensity of the radial complex electric field (E_r). E_ϕ is pointing toward n_ϕ.

using integrated photonic circuits, such that we can control the superposition state in the hyper-Poincaré sphere.

3.1. Left and Right Vortices

First, we continue to evaluate the left-vortexed state, injected from the port 1. We have calculated azimuthal and radical components for $|\mathrm{L}\rangle$ to obtain

$$E_\phi = \left(\frac{e^{-i\frac{\pi}{4}}}{\sqrt{2}}\right) e^{i\phi}\,(-\sin\phi - i\cos\phi) = -\frac{1}{2}(1+i) \quad (30)$$

$$E_r = \left(\frac{e^{-i\frac{\pi}{4}}}{\sqrt{2}}\right) e^{i\phi}\,(\cos\phi - i\sin\phi) = \frac{1}{2}(1-i). \quad (31)$$

Our numerical results support this picture, as shown in **Figure 9**. Both E_ϕ and E_r are almost constant over the location of the ring, where the intensity is maximized. The overall intensity of E_ϕ is larger than E_r, as explained by the dominant scattering of evanescent component of E_ϕ at the internal grating [29]. The constant E_ϕ does not preclude, however, the existence of the finite OAM of $m' = -1$, as ϕ_x and ϕ_y are clearly rotating to the left over time. The rotated local spin component of $|\text{local spin}\rangle$ also gives rise to a contribute for E_ϕ, since $E_{\text{spin}}\left(\sin^2(\phi) + \cos^2(\phi)\right) = E_{\text{spin}}$, which also gives a constant E_ϕ along the direction of the rotation (ϕ).

Similarly, we have also calculated the mode profiles for the input from the port 2 to generate $|\mathrm{R}\rangle$. We confirmed that the vortex is approximately expressed as

$$|\mathrm{R}\rangle = \frac{e^{-i\frac{\pi}{4}}}{\sqrt{2}}\begin{pmatrix}1\\ i\end{pmatrix} e^{-i\phi}, \quad (32)$$

which means the generation of the right-vortexed state. As we expected the total angular momentum is zero, since it is the direct tensor product state with the left-circularly polarized state,

$$|\mathrm{R}\rangle = |\circlearrowleft\rangle_{\text{spin}} \otimes |\circlearrowright\rangle_{\text{orbit}}. \quad (33)$$

The conservation law of angular momentum upon the diffraction by the grating gear is given by

$$s + m + N = s' + m', \quad (34)$$

where $s = 0$, $m = +10$, $N = -10$, $s' = +1$, and $m' = -1$.

The corresponding azimuthal and radical components for $|\mathrm{R}\rangle$ become

$$E_\phi = \left(\frac{e^{-i\frac{\pi}{4}}}{\sqrt{2}}\right) e^{-i\phi}\,(-\sin\phi + i\cos\phi) = \frac{1}{2}(1+i) \quad (35)$$

$$E_r = \left(\frac{e^{-i\frac{\pi}{4}}}{\sqrt{2}}\right) e^{-i\phi}\,(\cos\phi + i\sin\phi) = \frac{1}{2}(1-i). \quad (36)$$

Numerical simulation completely supports this expectation, as shown in **Figure 10**. E_ϕ (**Figures 10A,B**) changes its sign from

the corresponding left-vortexed state (**Figures 9A,B**), while the relative phase between real and imaginary parts are maintained, which are determined by the location z of the detector, due to the simple phase evolution of $e^{i(kz-\omega t)}$. On the other hand, E_r for the right vortex (**Figures 10D,E**) shows the same phase with the corresponding E_r for the left vortex (**Figures 9D,E**).

Therefore, we could prepare two orthogonal states of $|\mathrm{L}\rangle$ and $|\mathrm{R}\rangle$ simply by injecting photons from different ports. The orthogonality of the modes is guaranteed in 2-folds: one for the spin state as

$$ {}_{\mathrm{spin}}\langle \circlearrowleft \mid \circlearrowright \rangle_{\mathrm{spin}} = \frac{1}{2}\begin{pmatrix}1 & -i\end{pmatrix}\begin{pmatrix}1\\ -i\end{pmatrix} = 0, \tag{37}$$

and the other for OAM

$$ {}_{\mathrm{orbit}}\langle \circlearrowleft \mid \circlearrowright \rangle_{\mathrm{orbit}} = \int_0^{2\pi} \frac{d\phi}{2\pi}\, \mathrm{e}^{-2\phi i} = 0. \tag{38}$$

We can also confirm the proper normalization as

$$ \langle \mathrm{L}|\mathrm{L}\rangle = \frac{1}{2}\begin{pmatrix}1 & i\end{pmatrix}\begin{pmatrix}1\\ -i\end{pmatrix}\int_0^{2\pi}\frac{d\phi}{2\pi}\,1 = 1 \tag{39}$$

$$ \langle \mathrm{R}|\mathrm{R}\rangle = \frac{1}{2}\begin{pmatrix}1 & -i\end{pmatrix}\begin{pmatrix}1\\ i\end{pmatrix}\int_0^{2\pi}\frac{d\phi}{2\pi}\,1 = 1. \tag{40}$$

3.2. Linearly Vortexed States

Now, we have prepared two states of $|\mathrm{L}\rangle$ and $|\mathrm{R}\rangle$, and we will discuss the superposition state among them. We assume that we can control the amplitudes and phases of two input beams from port 1 and port 2.

First, we will construct horizontally ($|\mathrm{H}\rangle$) and vertically ($|\mathrm{V}\rangle$) vortexed state. Considering the analogy to the polarization [48, 50, 51] and a spin 2-level system [5–7], we expect a unitary transformation

$$ \begin{pmatrix}|\mathrm{L}\rangle\\ |\mathrm{R}\rangle\end{pmatrix} = \frac{1}{\sqrt{2}}\begin{pmatrix}1 & i\\ 1 & -i\end{pmatrix}\begin{pmatrix}|\mathrm{H}\rangle\\ |\mathrm{V}\rangle\end{pmatrix}, \tag{41}$$

whose inverse transformation becomes

$$ \begin{pmatrix}|\mathrm{H}\rangle\\ |\mathrm{V}\rangle\end{pmatrix} = \frac{1}{\sqrt{2}}\begin{pmatrix}1 & 1\\ -i & i\end{pmatrix}\begin{pmatrix}|\mathrm{L}\rangle\\ |\mathrm{R}\rangle\end{pmatrix}. \tag{42}$$

Therefore, the horizontally vortexed state is given by injecting photons in the same amplitude and the same phase into both

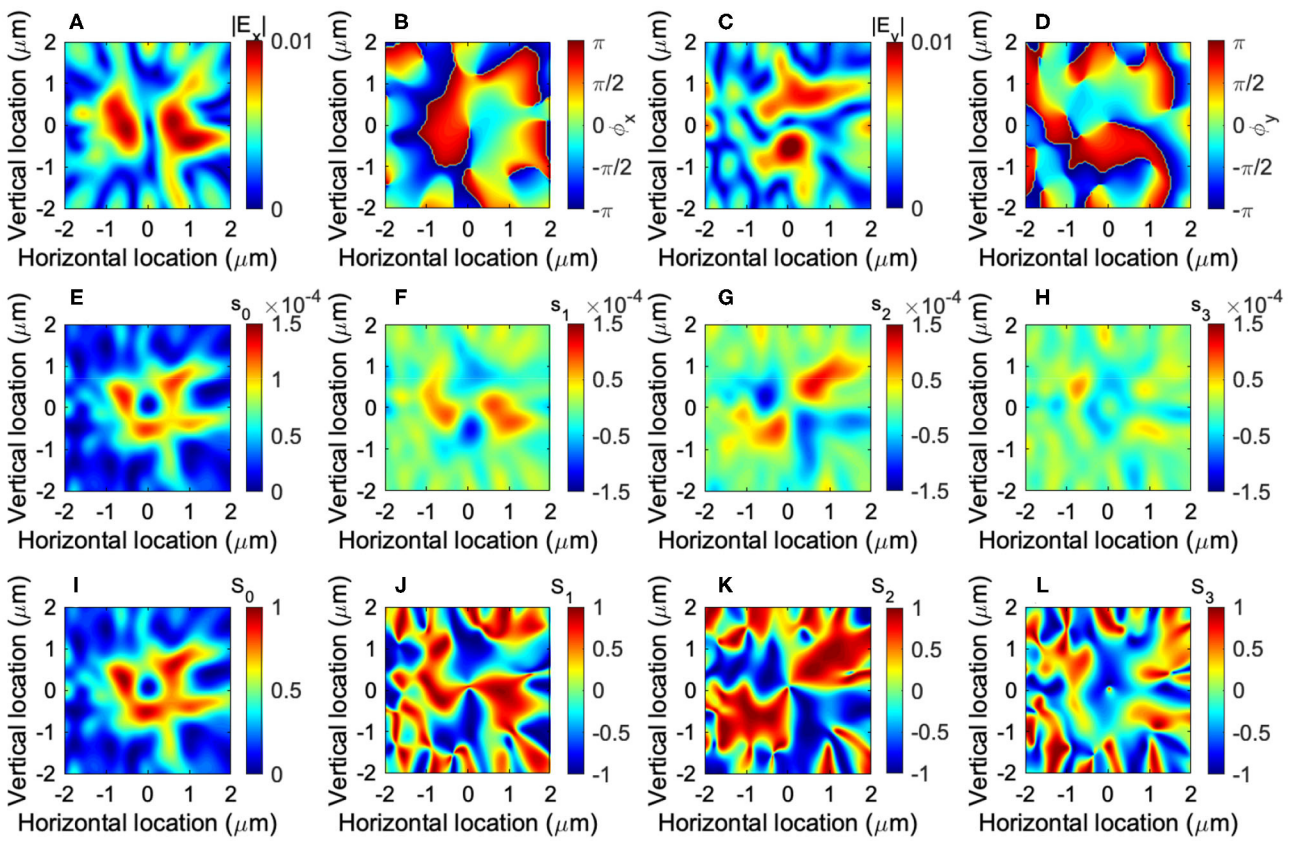

FIGURE 11 | Horizontal vortex generated from the gear of $N = 10$. The input port 1 and 2 are used to inject photons to the waveguide, and two injected modes are in the same phase. The mode profile of a vortex is obtained at $z = 1\mu$m above the gear. **(A)** Real part and **(B)** imaginary part of the horizontal complex electric field (E_x). **(C)** Real part and **(D)** imaginary part of the vertical complex electric field (E_y). A horizontal dipole is recognized for E_x with a node at the center. **(E–H)** The local spin components (s_0, s_1,s_2,s_3), and **(I–L)** normalised Stokes parameters (S_0, S_1,S_2,S_3) are also shown. The circularly polarized component of s_3 **(H)** was substantially reduced.

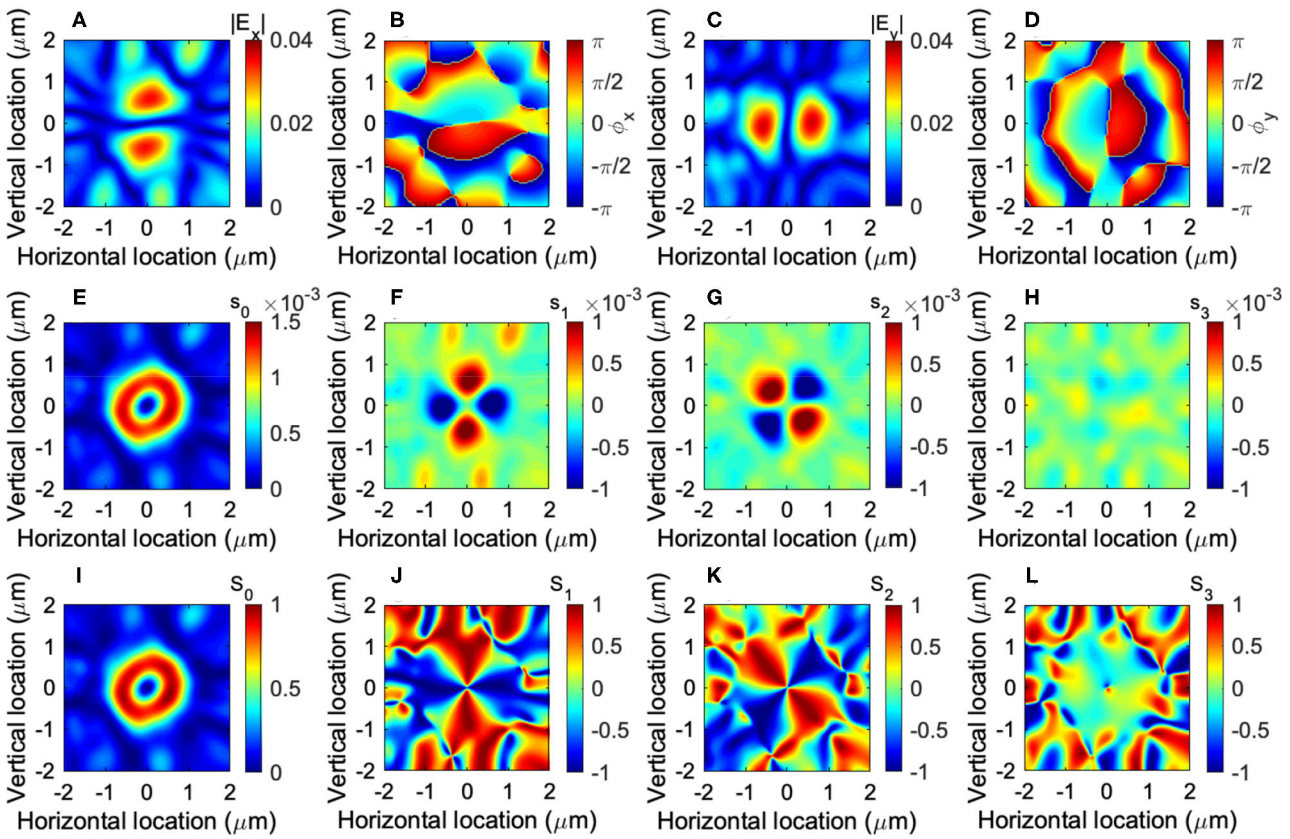

FIGURE 12 | Vertical vortex generated from the gear of $N = 10$. The input port 1 and 2 are used to inject photons to the waveguide, and two injected modes are out of the phase. The mode profile of a vortex is obtained at $z = 1\mu$m above the gear. **(A)** Real part and **(B)** imaginary part of the horizontal complex electric field (E_x). **(C)** Real part and **(D)** imaginary part of the vertical complex electric field (E_y). A vertical dipole is recognized for E_x with a node at the center. **(E–H)** The local spin components (s_0, s_1,s_2,s_3), and **(I–L)** normalised Stokes parameters (S_0, S_1,S_2,S_3) are also shown.

ports, to get

$$|\mathrm{H}\rangle = \frac{1}{\sqrt{2}}\left(|\mathrm{L}\rangle + |\mathrm{R}\rangle\right). \tag{43}$$

Numerically results for the generated vortex of $|\mathrm{H}\rangle$ are shown in **Figure 11**. It is important to be aware that the node is maintained at the center of the vortex. The mode profile of E_x is a dipole-like shape, aligned horizontally. E_x exhibits horizontal distribution, while E_y has a profile along the vertical direction. The difference is coming from the phase difference between real parts and imaginary parts, due to the difference in polarization. Therefore, the E_y component shows a conjugate vertically vortexed structure. If we would like to observe a purely horizontal vortexed state, we can use a polarizer to extract only the x component. Here, we shall call this mode as horizontally vortexed state, referring to the x component, while the y component is always its conjugate state. We have also calculated the local spin components (**Figures 11E,F**) and Stokes parameters (**Figures 11I–L**). The circularly polarized component was substantially compensated by the destructive superposition between left- and right-vortexed states.

On the contrary, the vertically vortexed state (**Figure 12**) is given by

$$|\mathrm{V}\rangle = \frac{-i}{\sqrt{2}}\left(|\mathrm{L}\rangle - |\mathrm{R}\rangle\right), \tag{44}$$

whose mode profile of E_x is a dipole-like shape, aligned vertically. The dipole-like shape of E_y is rotated 90°, which is in fact a conjugate horizontally vortexed state. It also has a node at the center.

If we include the spin state, these states correspond to a singlet state

$$|\mathrm{V}\rangle = \frac{-i}{\sqrt{2}}\left(|\downarrow\rangle_{\mathrm{spin}}|\uparrow\rangle_{\mathrm{orbit}} - |\uparrow\rangle_{\mathrm{spin}}|\downarrow\rangle_{\mathrm{orbit}}\right), \tag{45}$$

and a triplet state

$$|\mathrm{H}\rangle = \frac{1}{\sqrt{2}}\left(|\downarrow\rangle_{\mathrm{spin}}|\uparrow\rangle_{\mathrm{orbit}} + |\uparrow\rangle_{\mathrm{spin}}|\downarrow\rangle_{\mathrm{orbit}}\right), \tag{46}$$

where we have used $\uparrow$ and $\downarrow$ instead of $\circlearrowleft$ and $\circlearrowright$, respectively, and we have omitted to show $\otimes$ for simplicity. It is interesting

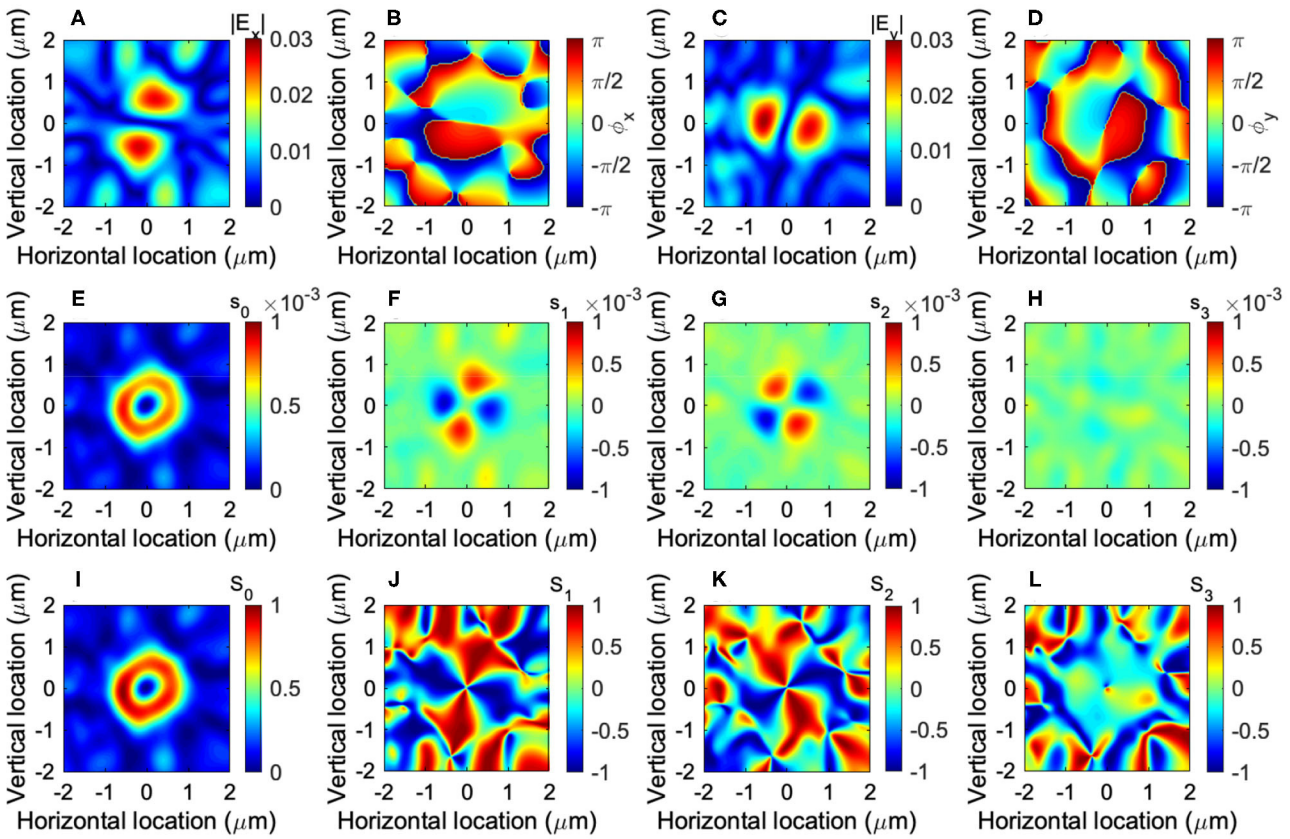

FIGURE 13 | Diagonal vortex generated from the gear of $N = 10$. The input port 1 and 2 are used to inject photons to the waveguide, and the phase of the input 2 is $\pi/2$ ahead of the phase of the input 1. The mode profile of a vortex is obtained at $z = 1\mu$m above the gear. **(A)** The amplitude ($|E_x|$) and **(B)** the phase (ϕ_x) of the horizontal electric field E_x. **(C)** The amplitude ($|E_x|$) and **(D)** the phase (ϕ_y)of the horizontal electric field E_y. The phase is not obviously rotating any more. A diagonal dipole is recognized for E_x with a node at the center. **(E–H)** The local spin components (s_0, s_1,s_2,s_3), and **(I–L)** normalised Stokes parameters (S_0, S_1,S_2,S_3) are also shown.

to make a superposition state by using both internal spin degree of freedom and OAM. Alternatively, if we describe these states by the horizontally ($\leftrightarrow$) and the vertically ($\updownarrow$) polarized and vortexed states, we obtain a singlet state

$$|\mathrm{V}\rangle = \frac{1}{\sqrt{2}}\left(|\leftrightarrow\rangle_{\mathrm{spin}}|\updownarrow\rangle_{\mathrm{orbit}} - |\updownarrow\rangle_{\mathrm{spin}}|\leftrightarrow\rangle_{\mathrm{orbit}}\right), \quad (47)$$

and a triplet state

$$|\mathrm{H}\rangle = \frac{1}{\sqrt{2}}\left(|\leftrightarrow\rangle_{\mathrm{spin}}|\leftrightarrow\rangle_{\mathrm{orbit}} + |\updownarrow\rangle_{\mathrm{spin}}|\updownarrow\rangle_{\mathrm{orbit}}\right). \quad (48)$$

If we use the gear of $N = 8$, we could also generate another two states for the triplet states

$$|\circlearrowleft\rangle_{\mathrm{spin}}|\circlearrowleft\rangle_{\mathrm{orbit}} = |\uparrow\rangle_{\mathrm{spin}}|\uparrow\rangle_{\mathrm{orbit}} \quad (49)$$

$$|\circlearrowright\rangle_{\mathrm{spin}}|\circlearrowright\rangle_{\mathrm{orbit}} = |\downarrow\rangle_{\mathrm{spin}}|\downarrow\rangle_{\mathrm{orbit}}. \quad (50)$$

For these states, the total sum of angular momentum between spin and OAM remain finite.

We are aware that the intensity of the intensity of $|\mathrm{H}\rangle$ (**Figure 11**) is smaller than that of $|\mathrm{V}\rangle$ (**Figure 12**). The reason is presumably because of our Si photonic waveguide design. All the modes in the waveguide is in the TE mode, which is vertically polarized along y direction, and there exists a tiny amount of the longitudinal component, due to the transverse nature of electromagnetic waves. Regardless of the cylindrical symmetry of the gear, most of the photons are diffracted upwards by the grating without circulating the ring resonator. Therefore, the amount of the horizontally oscillating mode is reduced.

3.3. Diagonally Vortexed States

Next, we have considered the diagonal $|\mathrm{D}\rangle$ (**Figure 13**) and the anti-diagonal $|\mathrm{A}\rangle$ (**Figure 14**) vortices. In analogy to the polarization, we obtain

$$|\mathrm{D}\rangle = \frac{1}{\sqrt{2}}(|\mathrm{H}\rangle + |\mathrm{V}\rangle) \quad (51)$$

$$= \frac{\mathrm{e}^{-\frac{\pi}{4}i}}{\sqrt{2}}(|\mathrm{L}\rangle + i|\mathrm{R}\rangle) \quad (52)$$

$$|\mathrm{A}\rangle = \frac{1}{\sqrt{2}}(|\mathrm{H}\rangle - |\mathrm{V}\rangle) \quad (53)$$

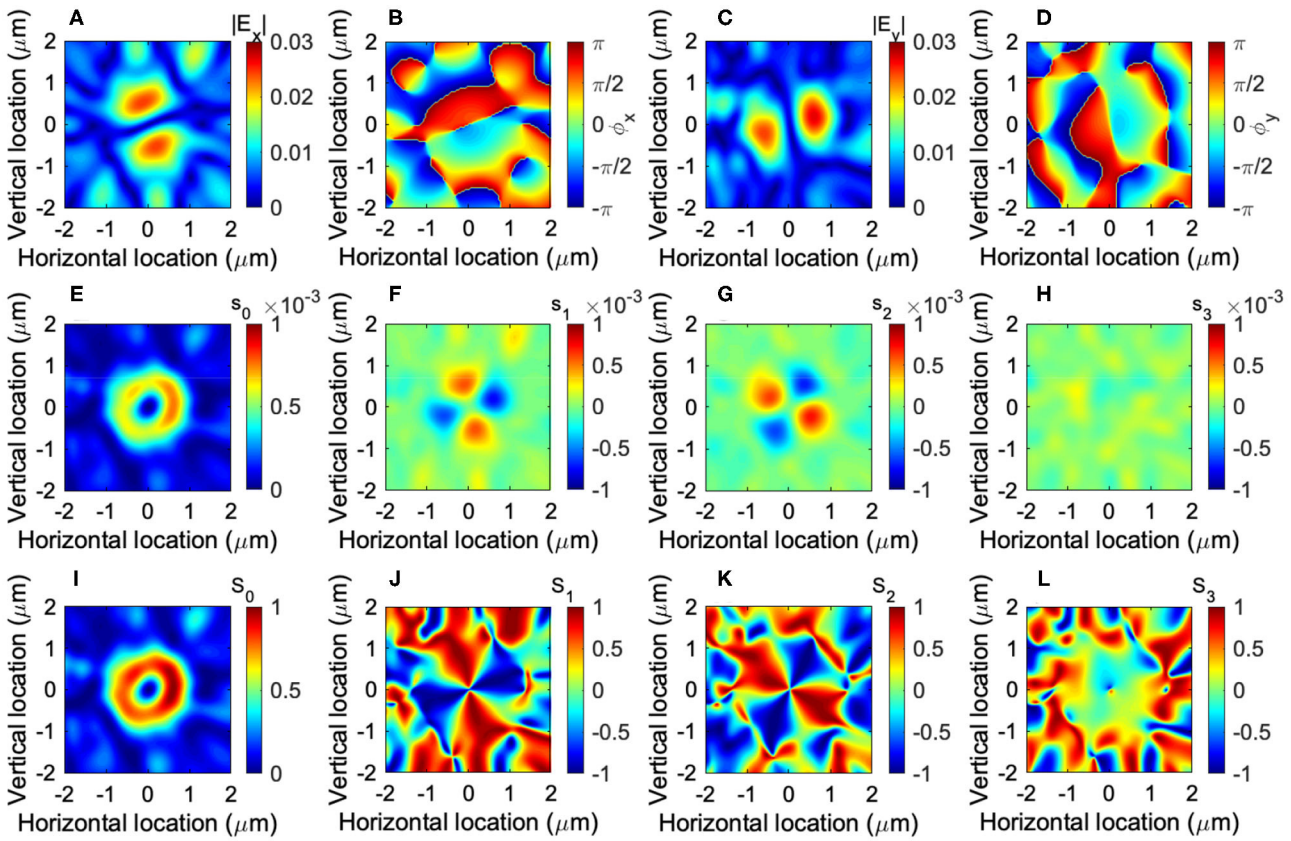

FIGURE 14 | Anti-diagonal vortex generated from the gear of $N = 10$. The input port 1 and 2 are used to inject photons to the waveguide, and the phase of the input 1 is $\pi/2$ ahead of the phase of the input 2. The mode profile of a vortex is obtained at $z = 1\mu$m above the gear. **(A)** The amplitude ($|E_x|$) and **(B)** the phase (ϕ_x) of the horizontal electric field E_x. **(C)** The amplitude ($|E_x|$) and **(D)** the phase (ϕ_y)of the horizontal electric field E_y. An anti-diagonal dipole is recognized for E_x with a node at the center. **(E–H)** The local spin components (s_0, s_1,s_2,s_3), and **(I–L)** normalised Stokes parameters (S_0, S_1,S_2,S_3) are also shown.

$$= \frac{e^{\frac{\pi}{4}i}}{\sqrt{2}} (|\mathrm{L}\rangle - i|\mathrm{R}\rangle) . \quad (54)$$

Numerical results for these states are shown in **Figures 13**, **14**, respectively. A dipole is aligned diagonally in E_x for the diagonal vortex (**Figure 13A**), and anti-diagonally in E_x for the anti-diagonal vortex (**Figure 14A**). Phases of these states are not rotating clearly, such that the average OAM components along z vanish.

If we include spin states, these states become

$$|\mathrm{D}\rangle = \frac{1}{\sqrt{2}} \left(|\leftrightarrow\rangle_{\mathrm{spin}} |\nearrow\rangle_{\mathrm{orbit}} - |\updownarrow\rangle_{\mathrm{spin}} |\searrow\rangle_{\mathrm{orbit}} \right) \quad (55)$$

$$|\mathrm{A}\rangle = \frac{1}{\sqrt{2}} \left(|\leftrightarrow\rangle_{\mathrm{spin}} |\searrow\rangle_{\mathrm{orbit}} + |\updownarrow\rangle_{\mathrm{spin}} |\nearrow\rangle_{\mathrm{orbit}} \right) . \quad (56)$$

We also confirmed the conjugate nature of these states between E_x and E_y, as shown in **Figures 13**, **14**.

3.4. Hyper-Poincaré Sphere

By extending above ideas, we can generate a superposition state of left- and right- vortexed state $|\Theta, \Phi\rangle$, defined by the polar angle of Θ and the azimuthal angle of Φ in a hyper-Poincaré sphere. Here, we consider a superposition state between left- and right-vortexed states, generated from the gear. In our design, the polarization degree of freedom is locked to a state, which is opposite to the direction of the rotation for a vortex. This is a significant limitation, compared to the hyper-Poincaré sphere, discussed by Milione et al. [28], and we cannot arbitrary change the polarization state for each vortex. Our hyper-Poincaré sphere is similar to the original proposal of Padgett and Courtial [21], and we would like to control by the gear coupled to the Si photonic wire waveguides (**Figure 1**).

In order to achieve it, the amplitude of the input 1 must be $\cos(\Theta/2)$ and the amplitude of the input 2 must be $\sin(\Theta/2)$, while the phase factor of the input 1 must be $e^{-i\Phi/2}$ and the phase factor of the input 2 must be $e^{i\Phi/2}$. This is easily achievable in a Si photonic platform [70, 71]. Therefore, the vortexed state can be controlled in our hyper-Poincaré sphere (**Figure 15**).

In order to see how the vortexed state is changed, it is convenient to define the OAM operator defined by

$$\hat{\mathcal{S}}_1 = \hbar m \, \hat{\sigma}_1 = \hbar m \begin{pmatrix} 0 & 1 \\ 1 & 0 \end{pmatrix} \quad (57)$$

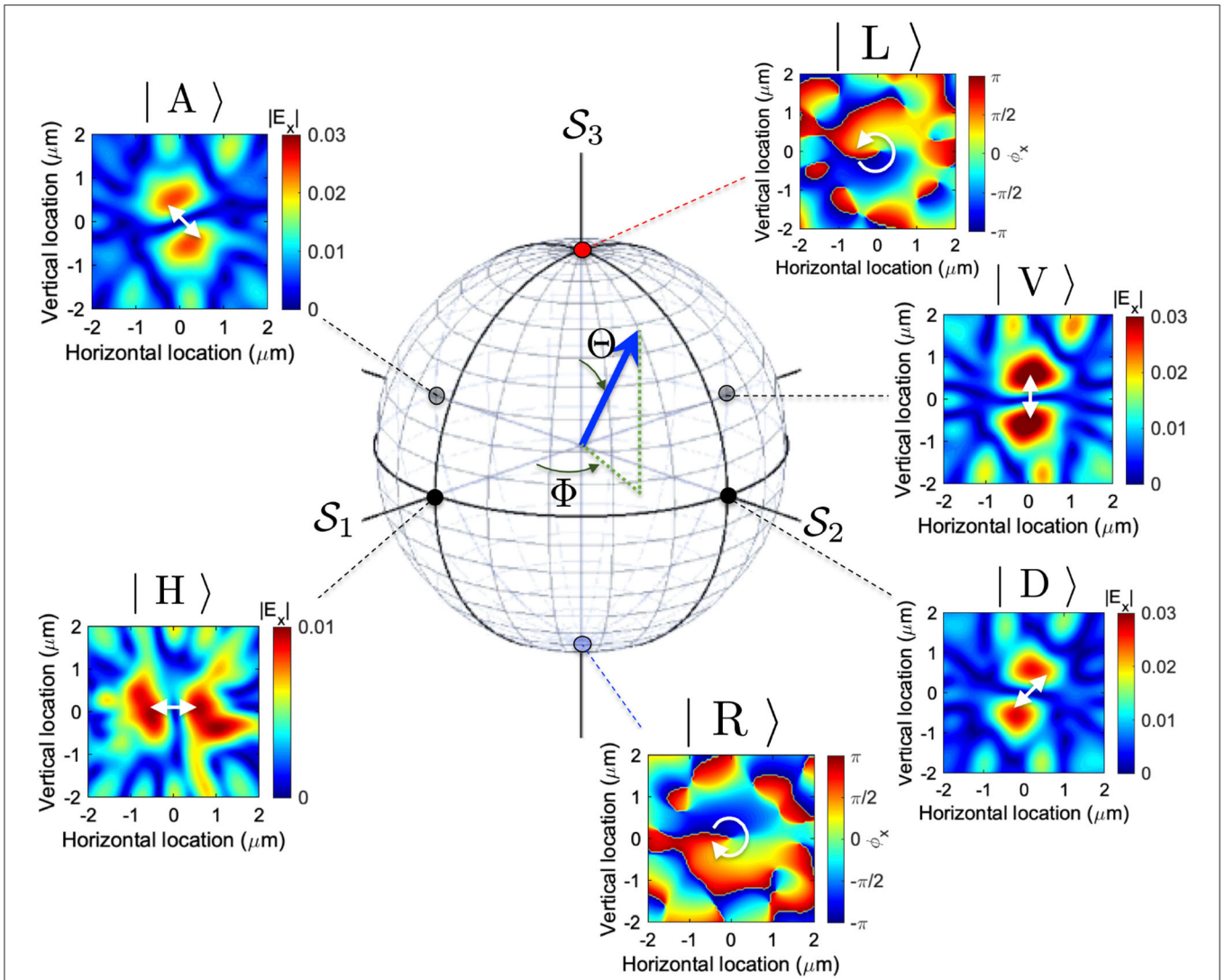

FIGURE 15 | Hyper-Poincaré sphere for describing a quantum state of a vortex. The polar angle of Θ will control the amplitudes of the left and the right vortexed states, while the azimuthal angle of Φ will control the phase between these basis states. Insets show examples of various vortexed states simulated in this work.

$$\hat{\mathcal{S}}_2 = \hbar m\,\hat{\sigma}_2 = \hbar m \begin{pmatrix} 0 & -i \\ i & 0 \end{pmatrix} \tag{58}$$

$$\hat{\mathcal{S}}_3 = \hbar m\,\hat{\sigma}_3 = \hbar m \begin{pmatrix} 1 & 0 \\ 0 & -1 \end{pmatrix}, \tag{59}$$

where σ_i (i = 1,2, and 3) are the Pauli matrices, and these operators will act to the Hilbert space spanned by $|\mathrm{L}\rangle$ and $|\mathrm{R}\rangle$ as basis states. We consider the OAM average per particle, or we can multiply the density of photons in a coherent vortexed state, $|\Theta, \Phi\rangle$. These definitions are in a close analogy to the Stokes parameters for polarization [5–7, 10, 11, 48, 48, 50–52, 55–57, 60] toward the application to OAM [19, 21, 28, 36, 37, 52–54]. If we take the quantum mechanical average of these operators by $|\Theta, \Phi\rangle$, we obtain Stokes parameters for hyper-Poincaré sphere

$$\mathcal{S}_1 = \langle \hat{\mathcal{S}}_1 \rangle = \hbar m \sin(\Theta)\cos(\Phi) \tag{60}$$

$$\mathcal{S}_2 = \langle \hat{\mathcal{S}}_2 \rangle = \hbar m \sin(\Theta)\sin(\Phi) \tag{61}$$

$$\mathcal{S}_3 = \langle \hat{\mathcal{S}}_3 \rangle = \hbar m \cos(\Theta), \tag{62}$$

and it is quite convenient to show these parameters in a 3-dimensional Poincaré sphere, as shown in **Figure 15**. The polar angle of Θ is related to the relative amplitude among two orthogonal modes, and the azimuthal angle of Φ corresponds to the phase difference between the two modes. Therefore, the proposed photonic gear with coupled two Si photonic wire waveguides is one of the practical systems to control these parameters in a compact on-chip module. Obviously, there are many other ways to control both amplitudes and phases to control the superposition state of left and right vortexed states.

4. CONCLUSION

We have proposed a silicon micro-gear coupled to two silicon photonic wire waveguide to control the vortexed state, generated out of the gear. We have shown the importance of the conservation law of the total angular momentum of spin and orbital angular momentum. The generated vortexed state is described by a tensor product of spin and orbit, and we proposed to achieve the superposition state between two orthogonal vortexed states. The amplitudes and the phases can be controlled by standard optical modulators, such that the control of the vortexed state is highly feasible. We believe Stokes parameters in the Poincareé sphere are one to the most important description to represent the quantum nature of spin state of photons. By extending Stokes parameters naturally to the orbital angular momentum in a hyper-Poincaré sphere is an important step to utilize OAM for various practical applications including quantum technologies.

DATA AVAILABILITY STATEMENT

The raw data supporting the conclusions of this article will be made available by the authors, without undue reservation.

AUTHOR CONTRIBUTIONS

The author confirms being the sole contributor of this work and has approved it for publication.

FUNDING

This work was supported by JSPS KAKENHI Grant Number JP 18K19958.

ACKNOWLEDGMENTS

The author would like to express sincere thanks to Prof I. Tomita for continuous discussions and encouragements.

REFERENCES

1. Plank M. On the theory of the energy distribution law of the normal spectrum. *Verhandl Dtsch Phys Ges*. (1900) **2**:237.
2. Dirac PAM. *The Principle of Quantum Mechanics*. Oxford: Oxford University Press (1930).
3. Tomonaga S. *Quantum Mechanics: Volume I: Old Quantum Theory*. Amsterdam: North-Holland Co. (1962).
4. Tomonaga S. *Quantum Mechanics Volume II: New Quantum Theory*. New York, NY: John Wiley & Sons (1966).
5. Sakurai JJ, Napolitano JJ. *Modern Quantum Mechanics*. Edinburgh: Pearson (2014).
6. Sakurai JJ. *Advanced Quantum Mechanics*. New York, NY: Addison-Wesley Publishing Company (1967).
7. Baym G. *Lectures on Quantum Mechanics*. New York, NY: Westview Press (1969).
8. Bohr N. The spectra of helium and hydrogen. *Nature*. (1913) **92**:231–2. doi: 10.1038/092231d0
9. Nauenberg M. Max Planck and the birth of the quantum hypothesis. *Am J Phys*. (2016) **84**:709. doi: 10.1119/1.4955146
10. Georgi H. *Lie Algebras in Particle Physics: from Isospin to Unified Theories*. Cambridge, MA: Westview Press (1999).
11. Pfeifer W. *The Lie Algebras su(N): An Introduction*. Berlin: Springer Basel AG (2003). doi: 10.1007/978-3-0348-8097-8
12. Weinberg S. *The Quantum Theory of Fields: Foundations, Volume 1*. Cambridge: Cambridge University Press (2005).
13. Lehner M. *The Cambridge Companion to Einstein (Cambridge Companions to Philosophy)*. Cambridge: Cambridge University Press (2014).
14. Abrikosov AA, Gorkov LP, Dzyaloshinski IE. *Methods of Quantum Field Thoery in Statistical Physics*. New York, NY: Dover (1975).
15. Fetter AL, Walecka JD. *Quantum Theory of Many-Particle Systems*. New York, NY: Dover (2003).
16. Nagaosa N. *Quantum Field Theory in Condensed Matter Physics*. Berlin: Springer (1999). doi: 10.1007/978-3-662-03774-4
17. Wen XG. *Quantum Field Theory of Many-Body Systems*. Oxford: Oxford University Press (2004).
18. Altland A, Simons B. *Condensed Matter Field Theory*. Cambridge: Cambridge University Press (2010). doi: 10.1017/CBO9780511789984
19. Allen L, Beijersbergen MW, Spreeuw RJC, Woerdman JP. Orbital angular momentum of light and the transformation of Laguerre-Gaussian laser modes. *Phys Rev A*. (1992) **45**:8185–9. doi: 10.1103/PhysRevA.45.8185
20. van Enk SJ, Nienhuis G. Commutation rules and eigenvalues of spin and orbital angular momentum of radiation fields. *J Mod Opt*. (1994) **41**:963–77. doi: 10.1080/09500349414550911
21. Padgett MJ, Courtial J. Poincaré-sphere equivalent for light beams containing orbital angular momentum. *Opt Lett*. (1999) **24**:430–2. doi: 10.1364/OL.24.000430
22. Allen L, Padgett MJ. The Poynting vector in Laguerre-Gaussian beams and the interpretation of their angular momentum density. *Opt Commun*. (2000) **184**:67–71. doi: 10.1016/S0030-4018(00)00960-3
23. Marrucci L, Manzo C, Paparo D. Optical spin-to-orbital angular momentum conversion in inhomogeneous anisotropic media. *Phys Rev Lett*. (2006) **96**:163905. doi: 10.1103/PhysRevLett.96.163905
24. Chen XS, Lü XF, Sun WM, Wang F, Goldman T. Spin and orbital angular momentum in gauge theories: nucleon spin structure and multipole radiation revisited. *Phys Rev Lett*. (2008) **100**:232002. doi: 10.1103/PhysRevLett.100.232002
25. Lai WJ, Lim BC, Phua PB, Tiaw KS, Teo HH, Hong MH. Generation of radially polarized beam with a segmented spiral varying retarder. *Opt Express*. (2008) **16**:15694–9. doi: 10.1364/OE.16.015694
26. Bliokh KY. Geometrodynamics of polarized light: Berry phase and spin Hall effecct in a gradient-index medium. *J Opt A Pure Appl Opt*. (2009) **11**:094009. doi: 10.1088/1464-4258/11/9/094009
27. Ji X. Comment on "Spin and Orbital Angular Momentum in Gauge Theories: Nucleon Spin Structure and Multipole Radiation Revisited." *Phys Rev Lett*. (2010) **104**:039101. doi: 10.1103/PhysRevLett.104.039101
28. Milione G, Sztul HI, Nolan DA, Alfano RR. Higher-order Poincaré sphere, stokes parameters, and the angular momentum of light. *Phys Rev Lett*. (2011) **107**:053601. doi: 10.1103/PhysRevLett.107.053601
29. Cai X, Wang J, Strain MJ, Johnson-Morris B, Zhu J, Sorel M, et al. Integrated compact optical vortex beam emitters. *Science*. (2012) **338**:363–6. doi: 10.1126/science.1226528
30. Barnett SM, Cameron RP, Yao AM. Duplex symmetry and its relation to the conservation of optical helicity. *Phys Rev A*. (2012) **86**:013845. doi: 10.1103/PhysRevA.86.013845
31. Sun J, Moresco M, Leake G, Coolbaugh D, Watts MR. Generating and identifying optical orbital angular momentum with silicon photonic circuits. *Opt Lett*. (2014) **39**:5977–80. doi: 10.1364/OL.39.005977
32. Barnett SM, Allen L, Cameron RP, Gilson CR, Padgett MJ, Speirits FC, et al. On the natures of the spin and orbital parts of optical angualr momentum. *J Opt*. (2016) **18**:064004. doi: 10.1088/2040-8978/18/6/064004

33. Barnett SM, Babiker M, Padgett MJ. Optical orbital angular momentum. *Philos Trans R Soc A*. (2016) **375**:20150444. doi: 10.1098/rsta.2015.0444
34. Leader E, Lorcé C. The angular momentum controversy: what's it all about and does it matter? *Phys Rep*. (2014) **541**:163–248. doi: 10.1016/j.physrep.2014.02.010
35. Bliokh KY, Rodríguez-Fortuño FJ, Nori F, Zayats AV. Spin-orbit interactions of light. *Nat Photon*. (2015) **9**:796–808. doi: 10.1038/nphoton.2015.201
36. Naidoo D, Roux FS, Dudley A, Litvin I, Piccirillo B, Marrucci L, et al. Controlled generation of higher-order Poincaré sphere beams from a laser. *Nat Photon*. (2016) **10**:327–32. doi: 10.1038/nphoton.2016.37
37. Liu Z, Liu Y, Ke Y, Liu Y, Shu W, Luo H, et al. Generation of arbitrary vector vortex beams on hybrid-order Poincaré sphere. *Photon Res*. (2017) **5**:15–21. doi: 10.1364/PRJ.5.000015
38. Bliokh KY, Bekshaev AY, Nori F. Optical momentum, spin, and angular momentum in dispersive media. *Phys Rev Lett*. (2017) **119**:073901. doi: 10.1103/PhysRevLett.119.073901
39. Bliokh KY, Bekshaev AY, Nori F. Optical momentum and angular momentum in complex media: from the Abraham-Minkowski debate to unusual properties of surface plasmon-polaritons. *New J Phys*. (2017) **19**:123014. doi: 10.1088/1367-2630/aa8913
40. Erhard M, Fickler R, Krenn M, Zeilinger A. Twisted photons: new quantum perspectives in high dimensions. *Light Sci Appl*. (2018) **7**:17146. doi: 10.1038/lsa.2017.146
41. Sotto M, Tomita I, Debnath K, Saito S. Polarization rotation and mode splitting in photonic crystal line-defect waveguides. *Front Phys*. (2018) **6**:85. doi: 10.3389/fphy.2018.00085
42. Sotto M, Debnath K, Khokhar AZ, Tomita I, Thomson D, Saito S. Anomalous zero-group-velocity photonic bonding states with local chirality. *J Opt Soc Am B*. (2018) **35**:2356–63. doi: 10.1364/JOSAB.35.002356
43. Sotto M, Debnath K, Tomita I, Saito S. Spin-orbit coupling of light in photonic crystal waveguides. *Phys Rev A*. (2019) **99**:053845. doi: 10.1103/PhysRevA.99.053845
44. Dorney KM, Rego L, Brooks NJ, Romá JS, Liao CT, Ellis JL, et al. Controlling the polarization and vortex charge of attosecond high-harmonic beams via simultaneous spin-orbit momentum conservation. *Nat Photon*. (2019) **13**:123–9. doi: 10.1038/s41566-018-0304-3
45. Moreau PA, Toninelli E, Gregory T, Aspden RS, Morris PA, Padgett MJ. Imaging Bell-type nonlocal behavior. *Sci Adv*. (2019) **5**:eaaw2563. doi: 10.1126/sciadv.aaw2563
46. Ndagano B, Nape I, Cox MA, Rosales-Guzman C, Forbes A. Creation and detection of voctor vortex modes for classical and quantum communication. *J Light Technol*. (2018) **36**:292–301. doi: 10.1109/JLT.2017.2766760
47. Jackson JD. *Classical Electrodynamics*. New York, NY: John Wiley & Sons (1999).
48. Yariv Y, Yeh P. *Photonics: Optical Electronics in Modern Communications*. Oxford: Oxford University Press (1997).
49. Fox M. *Quantum Optics: An Introduction*. Oxford: Oxford University Press (2006).
50. Goldstein DH. *Polarized Light*. London: CRC Press (2011).
51. Gil JJ, Ossikovski R. *Polarized Light and the Mueller Matrix Approach*. London: CRC Press (2016).
52. Stokes GG. On the composition and resolution of streams of polarized light from different sources. *Trans Camb Philos Soc*. (1851) **9**:399–416.
53. Poincaré JH. *Théorie Mathématique de la Lumière*. G. Carré (1892).
54. d Castillo GFT, García IR. The Jones vector as a spinor and its representation on the Poincaré sphere. *Rev Mex Fis*. (2011) **57**:406–13.
55. Jones RC. A new calculus for the treatment of optical systems I. Description and discussion of the calculus. *J Opt Soc Am*. (1941) **31**:488–93. doi: 10.1364/JOSA.31.000488
56. Payne WT. Elementary spinor theory. *Am J Phys*. (1952) **20**:253–62. doi: 10.1119/1.1933190
57. Fano U. A stokes-parameter technique for the treatment of polarization in quantum mechnics. *Phys Rev*. (1954) **93**:121–3. doi: 10.1103/PhysRev.93.121
58. Collett E. Stokes parameters for quantum systems. *Am J Phys*. (1970) **38**:563. doi: 10.1119/1.1976407
59. Luis A. Polarization distributions and degree of polarization for quantum Gaussian light fields. *Opt Commun*. (2007) **273**:173–81. doi: 10.1016/j.optcom.2007.01.016
60. Born M, Wolf E. *Principles of Optics*. Cambridge: Cambridge University Press (1999).
61. Luis A. Degree of polarization in quantum optics. *Phys Rev A*. (2002) **66**:013806. doi: 10.1103/PhysRevA.66.013806
62. Pedrotti FL, Pedrotti LM, Pedrotti LS. *Introduction to Optics*. New York, NY: Pearson Education (2007).
63. Björk G, Söderholm J, Sánchez-Soto LL, Klimov AB, Ghiu I, Marian P, et al. Quantum degrees of polarization. *Opt Commun*. (2010) **283**:4440–7. doi: 10.1016/j.optcom.2010.04.088
64. Hecht E. *Optics*. Essex: Pearson Education (2017).
65. Courtial J, Dholakia K, Robertson DA, Allen L, Padgett MJ. Measurement of rotational frequency shift imparted to a rotating light beam possessing orbital angular momentum. *Phys Rev Lett*. (1998) **80**:3217–9. doi: 10.1103/PhysRevLett.80.3217
66. Devlin RC, Ambrosio A, Rubin NA, Mueller JPB, Capasso F. Arbitrary spin-to-orbital angular momentum conversion of light. *Science*. (2018) **358**:896–901. doi: 10.1126/science.aao5392
67. Al-Attili AZ, Kako S, Husain MK, Gardes FY, Higashitarumizu N, Iwamoto S, et al. Whispering gallery mode resonances from Ge micro-disks on suspended beams. *Front Mat*. (2015) **2**:43. doi: 10.3389/fmats.2015.00043
68. Shao Z, Zhu J, Chen Y, Zhang Y, Yu S. Spin-orbit interaction of light induced by transverse spin angular momentum engineering. *Nat Commun*. (2018) **9**:926. doi: 10.1038/s41467-018-03237-5
69. Zhang Z, Qiao X, Midya B, Liu K, Sun J, Wu T, et al. Tunable topological charge vortex microlaser. *Science*. (2020) **368**:760–3. doi: 10.1126/science.aba8996
70. Reed GT, Knights AP. *Silicon Photonics*. Chichester: Wiley (2004). doi: 10.1002/0470014180
71. Saito S, Tomita I, Sotto M, Debnath K, Byers J, Al-Attili AZ, et al. Si photonic waveguides with broken symmetries: applications from modulators to quantum simulations. *Jpn J Appl Phys*. (2020) **59**:SO0801. doi: 10.35848/1347-4065/ab85ad
72. Guan B, Scott RP, Qin C, Fontaine NK, Su T, Ferrari C, et al. Free-space coherent optical communication with orbital angular, momentum multiplexing/demultiplexing using a hybrid 3D photonic integrated circuit. *Opt Express*. (2013) **22**:145–56. doi: 10.1364/OE.22.000145
73. Pancharatnam S. Generalized theory of interference, and its applications. *Proc Indian Acad Sci Sect A*. (1956) **XLIV**:398–417. doi: 10.1007/BF03046095
74. Berry MV. Quantual phase factors accompanying adiabatic changes. *Proc R Sco Lond A*. (1984) **392**:45–57. doi: 10.1098/rspa.1984.0023
75. Tomita A, Cao RY. Observation of Berry's topological phase by use of an optical fiber. *Phys Rev Lett*. (1986) **57**:937–40. doi: 10.1103/PhysRevLett.57.937
76. Simon R, Mukunda N. Bargmann invariant and the geometry of Güoy effect. *Phys Rev Lett*. (1993) **70**:880–3. doi: 10.1103/PhysRevLett.70.880
77. Debnath K, Thomson DJ, Zhang W, Khokhar AZ, Littlejohns C, Byers F, et al. All-silicon carrier accumulation modulator babsed on a lateral metal-oxide-semiconductor capacitor. *Photon Res*. (2018) **6**:373–9. doi: 10.1364/PRJ.6.000373
78. Lee BG, Small BA, Bergman K, Xu Q, Lipson M. Transmission of high-data-rate optical signals through a micrometer-scale silicon ring resonator. *Opt Lett*. (2006) **31**:2701–6. doi: 10.1364/OL.31.002701
79. Bogaerts W, Heyn PD, Vaerenbergh TV, Vos KD, Selvaraja SK, Claes T, et al. Silicon microring resonators. *Laser Photon Rev*. (2012) **6**:47–73. doi: 10.1002/lpor.201100017
80. Serrano-Núñez MA, Shoji Y, Mizumoto T. Giant Faraday rotation of cobalt ferrite thin films deposited on silicon substrates for silicon photonic nonreciprocal device applications. *Appl Phys Express*. (2020) **13**:062002. doi: 10.35848/1882-0786/ab8b52
81. Cao QT, Wang H, Dong CH, Jing H, Liu RS, Chen X, et al. Experimental demonstration of spontaneous chirality in a nonlinear microresonator. *Phys Rev Lett*. (2017) **118**:033901. doi: 10.1103/PhysRevLett.118.033901
82. Almeida VR, Barrios CA, Panepucci RR, Lipson M. All-optical control of light on a silicon chip. *Nature*. (2004) **431**:1081–4. doi: 10.1038/nature02921
83. Kittel C. *Introduction to Solid State Physics*. 8th ed. New York, NY: John Wiley & Sons (2004).

84. Chuang SL. *Physics of Photonic Devices*. New York, NY: John Wiley & Sons (2009).
85. Joannopoulos JD, Johnson SG, Winn JN, Meade RD. *Photonic Crystals: Molding the Flow of Light*. New York, NY: Princeton University Press (2008). doi: 10.1515/9781400828241
86. Hamazaki J, Mineta Y, Oka K, Morita R. Direct observation of Pouy phase shift in a propagating optical vortex. *Opt Express*. (2006) **14**:8382–92. doi: 10.1364/OE.14.008382

Conflict of Interest: SS is employed by Hitachi, Ltd., Tokyo, Japan.

Frontiers in Physics

Investigates complex questions in physics to understand the nature of the physical world

Addresses the biggest questions in physics, from macro to micro, and from theoretical to experimental and applied physics.

Discover the latest Research Topics

See more →

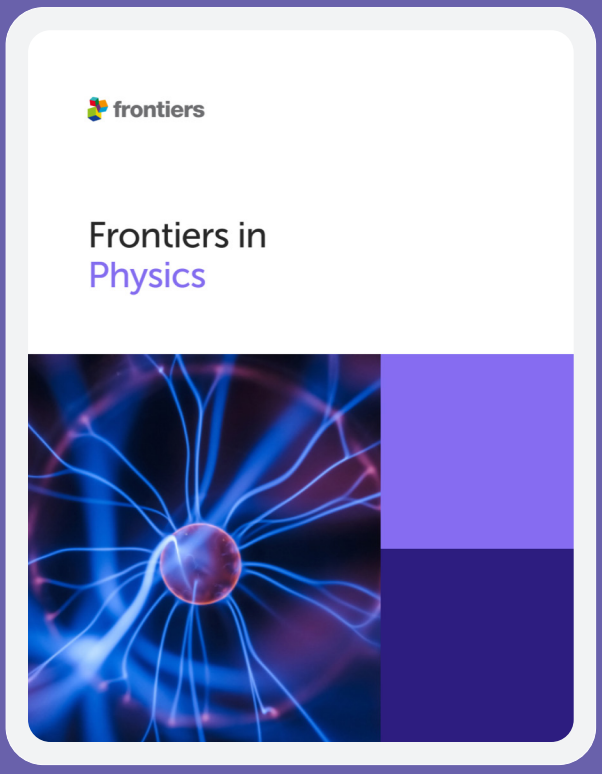

Frontiers

Avenue du Tribunal-Fédéral 34
1005 Lausanne, Switzerland
frontiersin.org

Contact us

+41 (0)21 510 17 00
frontiersin.org/about/contact